PLANETARY MISSION DESIGN AND ANALYSIS USING AEROASSIST MANEUVERS

A Dissertation

Submitted to the Faculty

of

Purdue University

by

Ye Lu

In Partial Fulfillment of the

Requirements for the Degree

of

Doctor of Philosophy

August 2019

Purdue University

West Lafayette, Indiana

THE PURDUE UNIVERSITY GRADUATE SCHOOL
STATEMENT OF DISSERTATION APPROVAL

Dr. Sarag J. Saikia, Co-Chair

School of Aeronautics and Astronautics

Prof. James M. Longuski, Co-Chair

School of Aeronautics and Astronautics

Prof. David A. Spencer

School of Aeronautics and Astronautics

Prof. Michael J. Grant

School of Aeronautics and Astronautics

Approved by:

Prof. Weinong Wayne Chen

Head of the School Graduate Program

ACKNOWLEDGMENTS

I would like to express my gratitude to my advisor Dr. Sarag J. Saikia and Prof. James M. Longuski for their invaluable insight throughout my doctoral study and for exposing me to interesting projects that helped shape my work. I am tremendously grateful for many opportunities that you have brought me. I would also like to thank my committee members, Prof. David Spencer and Prof. Michael Grant for their support and feedback.

In addition, I also would like to thank Ms. Vicki Leavitt for her support and guidance in my personal development. While working with her, I have learn invaluable lessons that are extremely helpful for my professional career. In addition, I want to acknowledge the Department of Mathematics, College of Engineering, and School of Aeronautics and Astronautics for providing financial support during my study.

Finally, I would like to extend my gratitude to my family for their endless support through this journey and all the time I spent away from home in the last ten years. Knowing you will always be there to support me has and will keep me moving forward everyday. I would also like to thank my fiancée for supporting me throughout. My home is where you are.

TABLE OF CONTENTS

Page

Page

LIST OF TABLES

LIST OF FIGURES

Figure Page

ABSTRACT

Lu, Ye Ph.D., Purdue University, August 2019. Planetary Mission Design and Analysis using Aeroassist Maneuvers. Major Professors: Sarag J. Saikia, James M. Longuski.

Mission designs have been focused on using proven orbital maneuvers (i.e., propulsive maneuvers and gravity-assist) to deliver spacecraft to planetary destinations. Aeroassist maneuvers, despite their potential benefits, have not been given serious considerations due to the perceived risk and complexity. As entry technologies mature, aeroassist maneuvers need to be considered more extensively. Currently, there is no tool available that can perform rapid preliminary mission designs using aeroassist maneuvers. In this dissertation, integrated design methodologies for aerocapture and aerogravity-assist are developed, which can be readily converted to design tools that enable rapid mission concept formulations.

The aerocapture design methodology is used to develop extensive design rules and relations for aerocapture missions to Titan, Venus, and Uranus, considering a wide range of vehicle parameters and interplanetary trajectories. These design rules and relations are intended as a convenient resource for mission designers and system engineers to evaluate the feasibility of aerocapture (e.g., effects of V_∞ on aerocapture missions) and the relevant design requirements, such as choices for vehicle characteristics and TPS materials. In addition, potentials for inclination change for Titan aerocapture are also quantified, presenting additional benefits of using aerocapture. Given the unusual orientation of Uranus, the changes in inclination and shift of line of apsides are also quantified for Uranus aerocapture.

A novel design methodology is developed for Saturn system missions using non-traditional aerogravity-assist maneuvers at Titan. Compared with the existing literature, the novel methodology explores a comprehensive design space by integrating

design considerations for interplanetary trajectories, atmospheric trajectories, arrival geometries at Titan, and vehicle designs. The methodology enables preliminary design trades and allows the mission designer to assess the feasibility of Titan aerogravity-assist and quickly develop requirements for trajectory designs and vehicle designs. The methodology also identifies potential Saturn and Titan arrival conditions. Results for an example Enceladus mission and Saturn system mission are presented, showing that a Saturn arrival V_∞ of 7 km/s renders Titan aerogravity-assist feasible for an Enceladus mission, while using the current entry technology.

Bank modulation and drag modulation have been considered separately for aeroassist vehicles in the literature. The investigation combines bank modulation and drag modulation to improve the control authorities for aeroassist vehicles and such improvements are quantified using numerical simulations for a wide range of vehicle design configurations. The results show the potential of using a low-L/D vehicle for aerocapture at Uranus using combined bank and drag modulation.

1. INTRODUCTION

1.1 Aeroassist Maneuvers

Aeroassist is a family of spacecraft maneuvers that use aerodynamic forces within the atmospheres of planetary bodies to actively control and change the trajectories. Aeroassist maneuvers include aerocapture, aerobraking, aerogravity-assist (AGA), and orbit transfer (e.g., plane change maneuvers). Over the years, a variety of terms have been used interchangeably for different aeroassist maneuvers. In the current literature, it is generally accepted that there are three types of aeroassist maneuvers which depend on the type of trajectories entering and exiting the atmosphere. The two types of orbits that are relevant to aeroassist maneuvers are hyperbolic and elliptical orbits. Hyperbolic orbits have positive specific orbit energy, ϵ, whereas elliptical orbits have negative ϵ.

$$\epsilon = \frac{V^2}{2} - \frac{\mu}{r} \tag{1.1}$$

where V is the velocity relative to the central body and μ is the gravitational constant and r is the radial distance from the center of the central body. The two types of orbits form a total of three cases as shown in Table 1.1.

Table 1.1. Three cases with two types of inbound and outbound orbits

Case	Inbound orbit	Outbound orbit	Note
1	Hyperbolic	Hyperbolic	Aerogravity-assist
2	Hyperbolic	Elliptical	Aerocapture
3	Elliptical	Elliptical	Aerobraking and orbit transfers

Case 1 (hyperbolic to hyperbolic) is usually referred to as aerogravity-assist maneuver, which is used as interplanetary orbital maneuvers to either increase or decrease the energy and change other orbital parameters relative to a central body. Aerogravity-assist uses both aerodynamic forces and gravity forces to change the orbit. Gravity-assist (GA) is an orbital maneuver that was most notably used in Voyager I and II, which leveraged the momentum exchange between the spacecraft and a planet to increase their energies relative to the Sun. Aerogravity-assist follows the same principle, but with the added aerodynamic forces [1].

Case 2 (hyperbolic to elliptical) is often referred as aerocapture, which is an orbit insertion maneuver. Aerocapture can be used for any orbiter missions to planets or moons (e.g., Saturn's moon, Titan) with a sensible atmosphere. Aerocapture uses aerodynamic drag force to decelerate upon hyperbolic arrival to enter an elliptical orbit around the target body.

Case 3 (elliptical to elliptical) may have different names and have the most applications in the literature. One name used is aerobraking, which was implemented in several missions, (i.e., Venus Express [2], Magellan [3], Mars Global Surveyor [4], Mars Odyssey [5], and Mars Reconnaissance Orbiter [6]), and aerobraking is being considered for the EnVision mission to Venus from European Space Agency (ESA) [7]. Other elliptical-to-elliptical aeroassist maneuvers include plane changes [8] and formation flying for satellites in Low Earth Orbit using aerodynamic lift and drag [9].

1.2 Literature Survey

1.2.1 Aerocapture Mission Design

Traditionally, primary orbit insertion maneuvers rely on chemical propulsion systems. For all spacecraft that capture around a planet, high thrust chemical propulsion is the proven and only method that has been used. Aerocapture is a promising alternative to propulsive orbit insertion in which aerodynamic forces are used in a planetary atmosphere to autonomously guide a spacecraft from a hyperbolic trajectory into the

target transfer orbit. Figure 1.1 shows a schematic illustration of aerocapture flight: the spacecraft enters the atmosphere of the target body, decelerates by an effective ΔV during the atmospheric phase (denoted as ΔV_{AC}), and exits the atmosphere in an elliptical orbit with periapsis within the atmosphere.

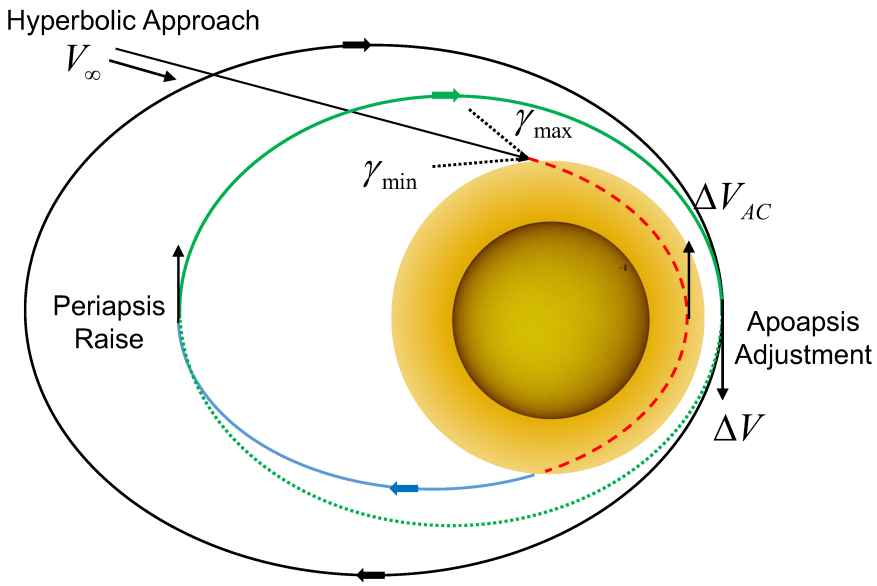

Figure 1.1. Aerocapture schematic shows the atmospheric pass (red dotted line), periapsis raise ΔV to enter transfer orbit (green), and apoapsis adjustment to enter science orbit (black) [10].

The concept of using aerodynamic forces to change orbit first appeared in publication in 1962 by London [11]. In the following two decades, many works have been done in the areas of aerocapture, aerobraking, and orbital transfer vehicles, which are summarized by Walberg [8]. Walberg ascribed the lack of interest in aeroassisted flight during the mid to late 1970s to the high perceived risk and cost associated with developing and implementing aeroassist technologies; and the benefit from increased payload capability was not a primary goal at the time. From 1985 to 1990, Aeroassisted Flight Experiment (AFE) [12–15] was studied as a possible mission to demonstrate aerobraking technology; however, the study was canceled due to cost overrun.

In the early 2000s, NASA centers collaborated and conducted aerocapture studies and provided reference point-designs of aerocapture systems for missions to Venus, Titan, and Neptune [10, 16, 17]. To fulfill the needs of future human Mars exploration, NASA's Space Technology Mission Directorate (STMD) is again investing in aeroassist technologies [18]. In early 2016, NASA Jet Propulsion Laboratory (JPL) conducted an A-Team study on aerocapture to identify how aeroassist/aerocapture technologies and associated risk reduction initiatives would be beneficial for potential robotic missions to Titan, Venus, Mars, Uranus, and Neptune [19]. The study concluded that NASA is technologically ready for aerocapture missions to Titan and Mars, and there is no need for flight demonstrations. In addition, because aerocapture may be an enabling technology for missions to ice giants (i.e., Uranus and Neptune), there is a renewed interest in aerocapture from NASA. In 2016, Purdue University led an aerocapture assessment in support of NASA's ice giants mission studies conducted at JPL [20, 21]. The study showed that for missions to ice giants, aerocapture technology could enable shorter trip times, higher delivered mass, or both. The study concluded that aerocapture at Uranus and Neptune requires a mid-lift-to-drag ratio (L/D) (i.e., from 0.6–0.8) vehicle due to uncertainties in guidance and navigation, atmosphere models, and vehicle aerodynamics properties. Since heritage entry vehicles, i.e., rigid aeroshell with L/D from 0–0.4, cannot be used and a mid-L/D vehicle is not available, significant cost and effort is required to develop a new mid-L/D vehicle to perform aerocapture at the Ice Giants.

A parametric study was performed for manned aerocapture at Mars [22], manned aerocapture mission for Earth return from Mars [23], aerocapture mission to Venus [24], and aerocapture mission to Titan [25]. Spilker et al. [18] conducted a qualitative assessment for aerocapture at all destinations on a programmatic level focusing on the state of technology readiness.

Figure 1.2 shows aerocapture may provide significant mass savings over propulsive options. The usable payload using propulsive captures decreases exponentially with increasing ΔV requirements, whereas usable payload, using aerocapture, decreases

linearly. A maximum ΔV of 3.5 km/s is assumed using a single-stage rocket for orbit insertion, which is constrained by the rocket propellant throughput. Rocket staging for orbit insertion is unlikely to be considered due to the associated risks. Hall et al. [26] quantified the cost and delivered mass of 11 representative aerocapture missions to all bodies in the Solar System with substantial atmospheres and compared with the best non-aerocapture options, including chemical propulsion, aerobraking, and solar electric propulsion. They showed that aerocapture "enables" missions to Jupiter, Saturn, and Neptune; and "enhances" missions and increase delivered mass to Venus by 79%, Mars by 15%, Titan by 280%, and Uranus by 218%. But a different study by NASA Ames [27] concluded that, for Uranus, aerocapture could increase the delivered payload by 42%, which is significant nevertheless. It is important to note that these mass saving numbers are derived using assumptions (i.e., same set of interplanetary trajectories are used to compare aerocapture and propulsive captures) that were revised later; thus, these numbers should be taken with some skepticism.

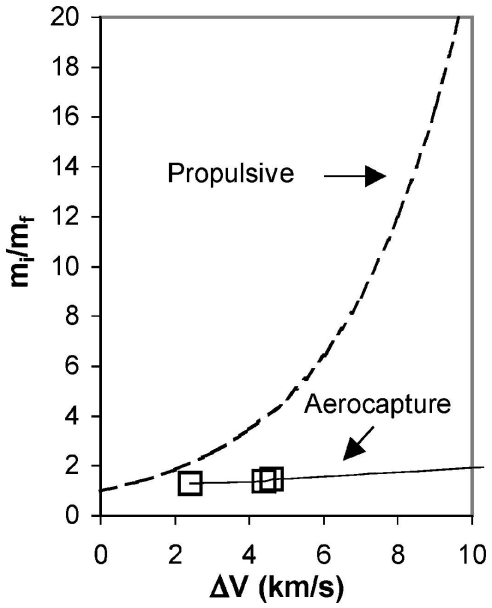

Figure 1.2. Mass ratio comparison between aerocapture and propulsive option shows the advantage of aerocapture at higher ΔV [26]. m_i and m_f are the spacecraft masses before and after the maneuver.

Guidance and control is an important aspect of aerocapture and many literatures have been devoted to the study of optimal trajectories, control, and guidance for aerocapture. This dissertation focuses on the mission design perspective, guidance and control are not investigated in further details in the text. For details on optimal trajectory and guidance, Miele et al. [28] summarizes the works prior to 1995 on guidance for aeroassisted orbit transfer; Lu et al. [29] discussed guidance using bank modulation; and Putnam and Braun [30] discusses guidance using drag modulation.

Aerocapture shares technologies with atmospheric entry, such as vehicle designs and thermal protection systems (TPS). Most of the aerocapture mission concept studies use entry vehicles. There are also studies showing that aerocapture can be achieved using a flexible tether [31–33] and an inflatable ballute [34–39]. In this dissertation, only entry vehicles are considered and investigated given their heritage in manned and robotic missions.

1.2.2 Aerogravity-Assist Mission Design

Aerogravity-assist is a maneuver where a spacecraft enters a planetary atmosphere upon hyperbolic approach and exits the atmosphere to a modified hyperbolic orbit. Figure 1.3 shows the difference between gravity-assist and aerogravity-assist. Traditional aerogravity-assist maneuver achieves a higher turn angle (δ_{AGA}) using aerodynamic forces, thus gaining a higher velocity boost compared to gravity-assist (δ_{GA}) [40, 41].

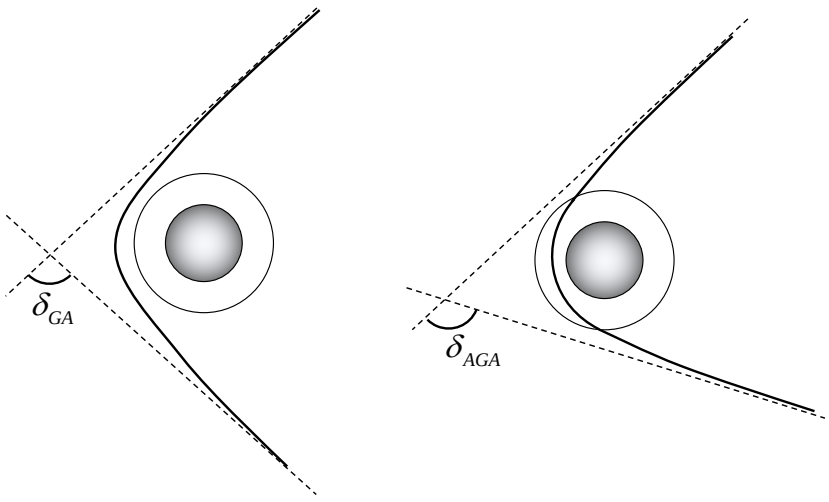

Figure 1.3. The figure on the left illustrates a pure gravity assist; and the figure on the right, an aerogravity-assist in which the spacecraft flies through the atmosphere.

Traditional aerogravity-assist maneuvers as in the literature have the same application as gravity-assist and use an atmosphere-bearing body to achieve a larger turn angle than gravity-assist and may require a vehicle with L/D of 3.0 or higher [42]. Such vehicle minimizes the aerodynamic drag forces [43] while maximizing the AGA turn angles. There are prototype hypersonic vehicles, i.e., Hypersonic Technology Vehicle [44] but most are for military purposes and none are operational. In the literature, the aerogravity-assist turn angle is solved using an analytical equation based on the assumption of vehicles with a high L/D, i.e., hypersonic waverider (L/D > 1.0) [45].

Figure 1.4 illustrates the concept of an Enceladus mission using Titan aerogravity-assist. Upon hyperbolic approach at Titan, the spacecraft slows down significantly and gets into orbit around Saturn. Such maneuver is different from the traditional AGA which minimizes the drag to reduce velocity loss. In order to distinguish between the traditional aerogravity-assist maneuver and Titan aerogravity-assist maneuver investigated in this dissertation, *traditional aerogravity-assist* refers to the one used

the most in the literature for interplanetary transfers, while *aerogravity-assist* refers to the case shown in Figure 1.4, and is used throughout the rest of the dissertation.

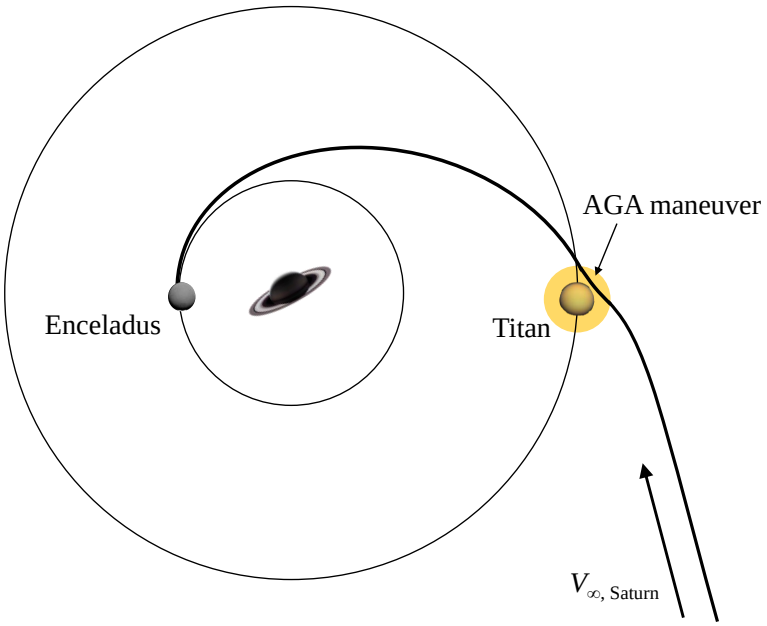

Figure 1.4. Illustration of spacecraft using Titan aerogravity-assist maneuver to get in transfer orbit to Enceladus (shown for minimum arrival velocity at Enceladus).

Titan has a small gravity (surface gravity is 1/7 of that for Earth) and a very thick atmosphere (density at surface altitude is 4.5 times that of Earth), the combination of which provides a very benign environment to perform aerocapture/aerogravity-assist for Saturn system missions. Ramsey and Lyne [46, 47] conducted a preliminary analysis of missions to Saturn and Enceladus using aerogravity-assist. They evaluated the corridor width and the target orbit and showed that it is feasible using vehicles with L/D of 1.0 and 0.48 (depending on the entry speed). Low-L/D vehicles (i.e., 0–0.4) can be used for Aerocapture at Titan [25].

1.3 Dissertation Contributions

This dissertation is focused on enabling rapid preliminary mission design and analysis using aerocapture and aerogravity-assist. The mission design process for early mission concept formulation starts with a science definition team that consists of primarily scientists and some engineers and technologists. The mission designers would go through rapid iterations for trajectory designs using trajectory search and optimization tools, i.e., STAR [48], Mystic and Mission Analysis Low-Thrust Optimizer (MALTO) [49] and Evolutionary Mission Trajectory Generator (EMTG) [50]. However, all tools available are not capable of designing missions using aeroassist maneuvers, with the exception of Satellite Tour Design Program (STOUR) [42] which can conduct automated designs of fast interplanetary missions using traditional aerogravity-assist maneuver. Other tools that can perform aeroassist-related analysis are for very specific purposes (i.e., POST2, for trajectory simulation [51] and LAURA, for aerothermal analysis [52]), and they are not suitable for early-stage mission concept formulations that require rapid iterations.

This dissertation advances the state-of-the-art in preliminary mission designs using aerocapture and aerogravity-assist that are of interest to the space exploration community, especially the mission designers. The specific contributions of this dissertation are listed as follows.

1. Developed an integrated methodology for aerocapture mission design

The first contribution of this work is the development of an integrated methodology to design aerocapture missions. The methodology can be readily converted into a design tool that fills the gap in the state-of-the-art mission design tools. Currently, there is no tool available that can perform rapid mission designs using aerocapture and the Ice-Giants pre-decadal study has concluded the need for such tool [20]. The integrated methodology allows mission designers to quickly assess the constraints for vehicle design and requirements for trajectory characteristics and help conduct rapid mission concept formulations using aerocapture. The methodology is also the first to

combine both the interplanetary trajectory design and the vehicle design for aerocapture missions and the methodology is applicable for any atmospheric-bearing body. The methodology considers design parameters including interplanetary arrival conditions (i.e., V_∞) and vehicle design constraints, such as peak g-load (for instrument and payload), peak stagnation-point heat rate, and total stagnation-point heat load (both for thermal protection system). The details of the integrated design methodology are discussed in Chapter 2.

2. Developed design rules and relations for aerocapture missions to Titan, Venus, and Uranus

Another contribution of this work is the design rules and relations developed using the integrated methodology for aerocapture missions. Prior to this work, only limited design rules for aerocapture were available for preliminary mission design and trade analysis, and some assumptions used in earlier work for aerocapture missions [26, 27] were revised based on the results of this work. Using the integrated design methodology, extensive design rules and relations are found for missions to Titan, Venus, and Uranus, which are intended as a convenient resource for mission designers to evaluate the feasibility of aerocapture (e.g., effects of V_∞ on aerocapture missions) and the relevant design requirements, such as choices for vehicle characteristics and TPS materials. The design rules and relations would enable NASA and other agencies to identify areas for technology investment for various missions. The analysis considers a wide range of interplanetary trajectories, i.e., arrival V_∞ and a wide range of vehicle designs, characterized by L/D and ballistic coefficients. The changes in inclination and apoapsis line through aerocapture maneuvers at Titan and Uranus are also quantified, which provide additional benefits using aerocapture. The methodology can be easily extended to the remaining atmospheric-bearing bodies of the Solar System to derive the specific design rules and relations. The results are presented and design rules and relations are discussed in details in Chapter 3.

3. Developed a novel design methodology using nontraditional aerogravity-assist maneuvers at Titan for Saturn system missions

A novel design methodology is developed for Saturn missions using aerogravity-assist at Titan. Potential Saturn arrival conditions are identified which are intended to help mission designers to quickly assess the feasibility of using Titan aerogravity-assist for future Saturn system missions. Compared with the existing literature [46, 47], the novel methodology explores an extensive design space by integrating interplanetary trajectory design, atmospheric trajectories, arrival geometry at Titan, and vehicle designs. The methodology combines a graphical method using vector diagrams and physical constraints. Considering key design parameters (i.e., V_∞) and vehicle design parameters (i.e., ballistic coefficient and L/D), the methodology is used to demonstrate the feasibility of using Titan AGA for Saturn and Enceladus missions. The design methodology is presented and detailed results are discussed in Chapter 4.

4. Established improvements in vehicle control using combined bank and drag modulation

Existing literatures have considered using bank modulation for aeroassist maneuvers and planetary entry, and only recently drag modulation has been studied for aerocapture and entry. However, none of the studies have considered the benefit of combining bank modulation and drag modulation to improve the control authority of aeroassist vehicles. This investigation offers a new control approach for aeroassist vehicles combining bank and drag modulation. The results may help the mission design community to quickly assess the vehicle requirements for aeroassisted missions and provide guidance for future technology investments. The improvements in control authority are quantified and presented by evaluating the theoretical corridor width for a wide range of vehicle configurations (i.e., L/D and ballistic coefficients). Such analysis has never been done in the literature, and it enhances early mission concept studies using aeroassist maneuvers. Control authorities (i.e., theoretical corridor width) using bank modulation, drag modulation, and combined bank and drag

modulation are compared. The results are also applicable to other vehicle control methods, e.g., active force control. Detailed discussion and results are presented in Chapter 5.

2. AEROCAPTURE DESIGN METHODOLOGY

In this chapter, the details of an integrated aerocapture design methodology are presented. To evaluate the trajectory of the spacecraft in the atmosphere, equations of motion for atmospheric flights are used and integrated numerically. Gravity models and atmosphere models are used to improve the accuracy of the simulation. Peak deceleration (g-load) is an important parameter for instrument and vehicle structural design and is evaluated during the atmospheric phase. Aerothermodynamic heating is also essential for aerocapture design as it affects the material selection for thermal protection system (TPS) and the mass fraction required to shield the spacecraft from the heat. When empirical relations are available, convective and radiative heating is evaluated throughout the atmospheric portion of the trajectory. The consideration of interplanetary trajectory and post-capture orbits are also discussed in detail.

2.1 Equations of Motion

The equations of motion for atmospheric flight is used for the atmospheric phase of an aerocapture maneuver. Kinematics equations relative to a non-rotating body in the body-centered and body-fixed reference frame are as follows [53]:

$$\dot{\theta} = \frac{V \cos\gamma \cos\chi}{r \cos\phi} \tag{2.1a}$$

$$\dot{\phi} = -\frac{V \cos\gamma \sin\chi}{r} \tag{2.1b}$$

$$\dot{r} = V \sin\gamma \tag{2.1c}$$

where θ and ϕ are the longitude and latitude in a spherical surface model, r the radial distance from the center, χ the heading angle measured clockwise from the direction of local parallel (eastward), V the velocity of the vehicle, γ the flight-path

angle (positive above local horizon). The dynamic equations including gravity force and aerodynamic forces are [53]:

$$\dot{V} = -\frac{q}{\beta} - g\sin\gamma + f\cos\gamma\sin\chi \tag{2.2a}$$

$$\dot{\gamma} = -\frac{q(L/D)}{V\beta}\cos\sigma + \left(\frac{V}{r} - \frac{g}{V}\right)\cos\gamma - \frac{f}{V}\sin\gamma\sin\chi \tag{2.2b}$$

$$\dot{\chi} = \frac{q(L/D)}{V\beta}\frac{\cos\sigma}{\cos\gamma} + \frac{V}{r}\cos\gamma\sin\chi\tan\phi + \frac{g}{V}\frac{\cos\chi}{\cos\gamma} \tag{2.2c}$$

where σ is the bank angle, which is the rotation angle about the relative velocity vector, $\beta = m/(C_D A)$ is the ballistic coefficient where m is vehicle mass and C_D is the aerodynamic drag coefficient, $q = (1/2)\rho V^2$ is the dynamic pressure, where ρ is the density of the atmosphere, and L and D are the lift and drag forces respectively defined as:

$$L = \frac{1}{2}\rho V^2 A C_L, \qquad D = \frac{1}{2}\rho V^2 A C_D \tag{2.3}$$

where C_L is the aerodynamic lift coefficient, and A is the aerodynamic reference area of the vehicle. The angle of attack, α, affects the C_L and C_D, and is assumed constant as the trim angle of attack. g and f are the radial and latitudinal components of the gravitational acceleration respectively which are defined as the following:

$$g = -\frac{\partial U}{\partial r}, \qquad f = \frac{1}{r}\frac{\partial U}{\partial \phi} \tag{2.4}$$

where U is the gravitational potential which a function of both r and ϕ. Expressed in 4th order expansion, the gravitational potential is:

$$\begin{aligned} U = \frac{\mu_p}{r} + J_2\frac{\mu_p}{r}\left(\frac{r_p}{r}\right)^2\left(\frac{1}{2} - \frac{3}{2}\sin^2\phi\right) + J_3\frac{\mu_p}{r}\left(\frac{r_p}{r}\right)^3\left(\frac{3}{2}\sin\phi - \frac{5}{2}\sin^3\phi\right) \\ + J_4\frac{\mu_p}{r}\left(\frac{r_p}{r}\right)^4\left(-\frac{3}{8} + \frac{30}{8}\sin^2\phi - \frac{35}{8}\sin^4\phi\right) \end{aligned} \tag{2.5}$$

where μ_p is the gravitational constant of the planetary body, r_p the equatorial radius, and J_2, J_3, and J_4 the characteristic constants of the gravitational field, whose values are from gravity models constructed using spacecraft radiometric tracking data. Table 2.1 summarizes the moment and geometric properties for planets and moon.

Table 2.1. Moments and geometric properties of selected bodies

Body	μ_p, $\times 10^{12}$ m^3/s^2	Equatorial radius, km	J_2 ($\times 10^{-6}$)	J_3 ($\times 10^{-6}$)	J_4 ($\times 10^{-6}$)	Scale Height, km
Titan [54]	8.978	2,575	31.808	−1.88	0	17
Venus	324.86	6,052	4.40	−1.93	−2.15	15.9
Earth	398.6	6,378	1,082.6	−2.54	−1.62	8.5
Mars	42.8	3,396	1,955.5	31.45	−15.38	11.1
Jupiter [55]	126,687	71,492*	14,695	0	−591	27
Saturn [55]	37,931	60,268*	16,290.7	0	−935.83	59.5
Uranus [56]	5,794	25,559*	3,341.29	0	−30.44	27.7
Neptune [56]	6,836	24,764*	3,408.43	0	−33.40	20

*The equatorial radius is defined at 1 bar.

Peak deceleration is an important parameter to consider and is constrained by spacecraft structure, engineering systems, and science payloads. The deceleration, n, is calculated as the following:

$$n = \frac{\sqrt{L^2 + D^2}}{m} = \frac{q}{\beta}\sqrt{1 + (L/D)^2} \tag{2.6}$$

2.2 Atmosphere Models

Atmosphere models of celestial bodies are constructed using data collected by two means: remote sensing and in-situ measurements. In-situ measurements often involve direct entry probe or spacecraft close fly-through in the upper atmosphere. Remote sensing includes both Earth-based observations and in-orbit spacecraft onboard measurements (e.g., radio occultation). In-situ measurement provides a high accuracy but lacks in the spatial and temporal coverage capabilities that remote sensing offers. Atmosphere models are usually constructed using all available data.

Titan Atmosphere

In 1981, Hunten [57] constructed the first model of Titan atmosphere by analytically fitting the Voyager's radio occultation data for altitude below 200 km and interpolating using the hydrostatic equation for altitudes between 200 km and 1270 km with only one measurement of temperature and number density at 1270 km. Hunten's model has a density uncertainty of 30%. In 1987, Lellouch and Hunten [57] updated and combined the earlier models into Lellouch-Hunten models: in the 0–200 km range, a model was constructed by Lellouch after taking into account uncertainties from occultation measurement data and variation in chemical composition; models for altitude above 200 km followed an updated model by Hunten, in which temperature profiles above 680 km were used from a physical modeling of the stratosphere, mesosphere, and thermosphere, while satisfying constraints from Voyager infrared spectrometer (IRIS) and ultraviolet spectrometer (UVS) data.

Design of Huygens probe was based on Lellouch-Hunten models, until 1994, when it was superseded by Yelle et al. models [58] which incorporated updated model for the thermal structure of the upper atmosphere and chemical composition of the atmosphere. Waite et al. [59] developed new models in 2013 using Cassini data from 2004 to 2010. Since different science instruments measure different altitude ranges, they used different sets of data from several instruments onboard Cassini and developed the vertical profile of Titan atmosphere. The model from the surface to 200 km uses both in-situ and remote sensing data—Huygens Atmosphere Structure Instrument (HASI) and Gas Chromatograph and Mass Spectrometer (GCMS), as well as Cassini's Composite Infrared Spectrometer (CIRS) and Radio Science Subsystem (RSS). Models from 150 to 400 km use CIRS data to characterize the atmosphere at these altitudes. From 600 to 1100 km, models used data from Cassini Ultraviolet Imaging Spectrograph (UVIS). From 950 to 1500 km, data from Ion and Neutral Mass Spectrometer (INMS) during close flybys was used. Then combining models at different altitudes through a cubic-spline interpolation, Waite et al. achieved vertical profiles of Titan atmosphere models [59].

All atmosphere models are empirical and use some form of interpolation to connect the models at different altitude regions. An engineering atmosphere model provides atmospheric properties (i.e., density, temperature, and pressure) from zero-mean altitude up to an altitude with a sensible atmosphere. An aerocapture vehicle never travels below certain altitudes (200–300 km depending on arrival V_∞, vehicle L/D and ballistic coefficient); therefore, numerical simulation of the trajectory only requires knowledge of atmosphere above those altitudes. A high-fidelity aerocapture simulation may use improved atmosphere models with a more accurate density profile for altitude ranges where aerodynamic forces dominate gravity (e.g., 200–850 km). Figures 2.1 and 2.2 compare the temperature and density profiles of Yelle et al. and Waite et al. models—the latter is more sophisticated and provides more accurate estimates of atmospheric properties. Trajectory simulation in this study uses density profiles from Waite et al. models.

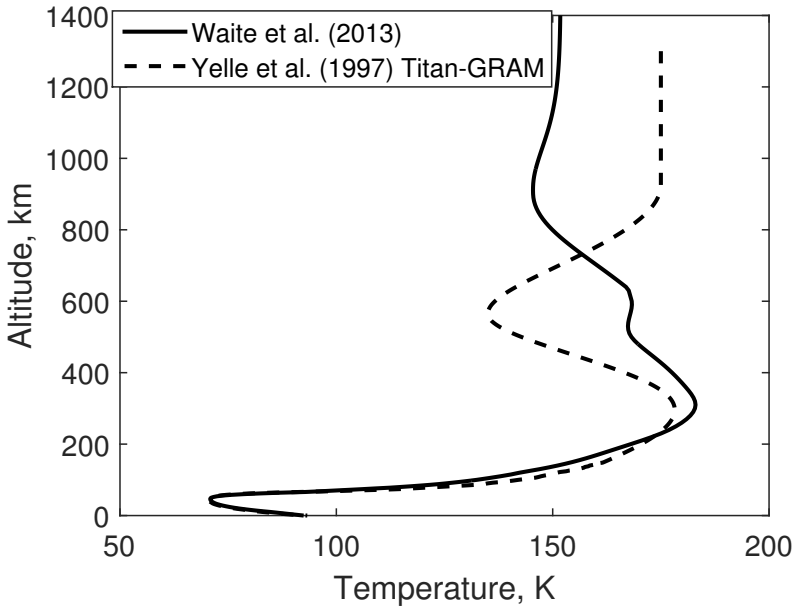

Figure 2.1. Comparison of temperature profiles shows that Waite et al. [59] improved the model accuracy by using a more detailed temperature profile (above 300 km altitude) than Yelle et al. models [58].

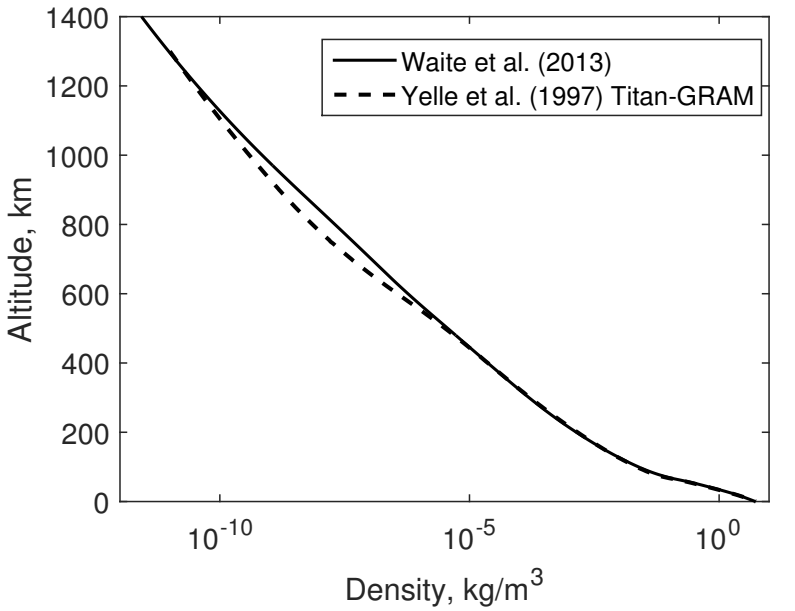

Figure 2.2. The comparison of density profiles shows that Waite et al. [59] predict a denser atmosphere at altitude range from 500 to 1100 km.

Venus Atmosphere

Abundant data is available for Venus atmosphere, and there are different engineering models developed independently, such as the Venus International Reference Atmosphere (VIRA) [60] and Venus Global Reference Atmospheric Model (GRAM) which is partially derived from VIRA. In this dissertation, VIRA data is used for numerical simulation, and the density profile is shown in Fig. 2.3.

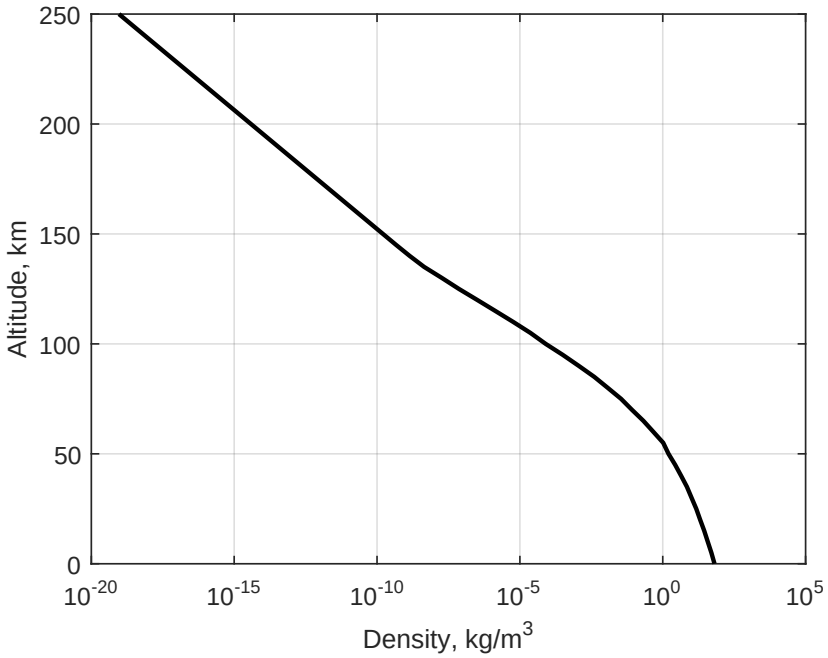

Figure 2.3. Density profile vs. altitude for Venus [60].

Uranus Atmosphere

Uranus atmosphere contains primarily hydrogen and helium and unlike for Venus and Titan, no GRAM model is available for Uranus. Data for Uranus atmosphere is rather limited and the only available is from the Voyager-2 flyby in 1986. Used in the simulation is the engineering atmosphere model developed based on the radio

occultation data from Voyage-2 flyby [61]. Figure 2.4 shows the density profile vs altitude used for the numerical simulation.

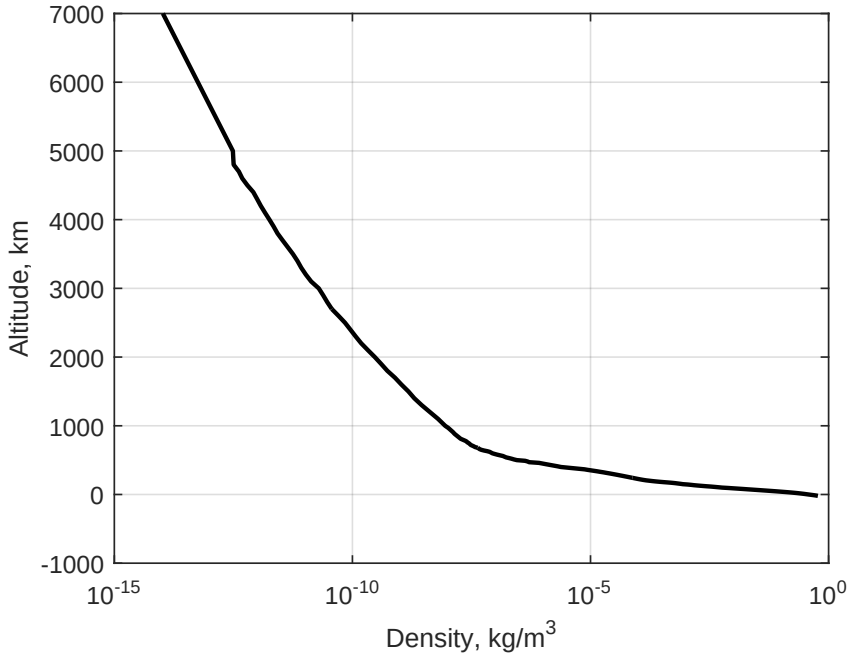

Figure 2.4. Density profile vs. altitude for Uranus [61].

2.3 Thermal Protection System

2.3.1 Rigid and Deployable Entry System

Aeroassist maneuver requires thermal protection system to shield the spacecraft from the aerodynamic heat generated during the atmospheric pass. Heritage entry vehicles have been proven for both robotic and manned missions. Most robotic missions used ballistic entry vehicles which have no active guidance or control (e.g., Mars Pathfinder, Mars Exploration Rovers, and Phoenix); whereas entry vehicles for manned missions and some Mars missions (e.g., Mars Science Laboratory) used lifting vehicles to control the entry trajectories in order to meet strict requirements such as landing accuracy and g-load limit (e.g., 10 g that the human body can sus-

tain). Traditional entry vehicles use rigid front aeroshell with a spherical section or sphere-cone shape. By offsetting the center of mass, the traditional rigid aeroshell can provide L/D of more than 0.3. Several other entry vehicle designs have been proposed and studied and they are Hypersonic Inflatable Aerodynamic Decelerator (HIAD) [62], Adaptable Deployable Entry and Placement Technology (ADEPT) [63], mid-L/D vehicle design [17], and star-body waverider [64]. Table 2.2 summarizes the design parameters of the past, current, and future entry vehicles. Most traditional spherical section or sphere-cone shaped entry vehicles have L/D in the range of 0–0.4 whereas space shuttle had an L/D of 1.0 at hypersonic speeds and up to 5.0 at approach speeds.

Peak g-load occurs at the maximum dynamic pressure during the atmospheric phase. Ballistic coefficient varies along the trajectory as the vehicle may lose mass from TPS material ablation and as the aerodynamic characteristics change. This study, however, assumes a constant ballistic coefficient throughout the entire trajectory.

2.3.2 Aerothermodynamic Heating

When a spacecraft enters the atmosphere at hypersonic speed, the aerodynamic drag force decelerates the spacecraft and generates heat, some of which is transferred onto the surface of the vehicle. There are two types of dominating heat transfers that occur: convective and radiative. Sutton & Graves [65] developed an empirical relation for convective heat rate with an arbitrary gas mixture:

$$\dot{q}_{s,c} = k \left(\frac{\rho}{R_n} \right)^{0.5} V^3 \tag{2.7}$$

where R_n is the nose radius in m. $\dot{q}_{s,c}$ has the unit of W/cm^2 and k is defined as follows [65]:

$$k = \frac{1}{\sqrt{\sum \frac{c_i}{K_i^2}}} \tag{2.8}$$

Table 2.2. Design parameter of heritage and proposed vehicles

Vehicle Design	Planet	Mission (Year)	Entry Mass, kg	$(L/D)_{trim}$
Spherical Section	Earth	Apollo (1960s)	5,560	>0.30
Sphere-cone	Mars	Viking I and II (1976)	576	0.18
Sphere-cone	Mars	MSL (2012)	3,380	0.24
ADEPT/HIAD	-	-	Variable	∼0.2
HIAD	-	-	Variable	∼0.2
Ellipsled	Neptune	-	∼6,000	0.6–0.8
-	Earth	Space Shuttle	∼100,000	1 (Hypersonic)
Starbody Waverider	-	Aeroassist	∼100,00	∼2 [64]

where c_i and K_i are respectively the mass fractions and constant coefficients of ith gas component.

Titan Heating Environment

Table 2.3 shows values of constant K and mass fractions of the two primary species in the Titan atmosphere: N_2 and CH_4. The approximate value of k in Eq. (2.7) is 1.7407×10^{-8}. The mass fraction of methane may have minimal effect on convective heat rate; however, at hypersonic speeds, methane can be decomposed behind the shock and release hydrogen atoms with high mobility, which will quickly diffuse to the surface. Callault et al. [66] investigated the effect of methane on radiative heat rate for Huygen's probe at a nominal -65 deg entry flight-path angle, and they showed that radiative heat rate is very sensitive to methane mass fraction. An increase from 0.5 % to 1.7 % in the mass fraction of methane results in an increase in peak radiative heat rate of more than 80%. (Note that mole fraction used by Callault et al. is converted into mass fractions for consistency.) An accurate methane mass fraction is imperative for estimating the radiative heating rate. While there exist some empirical relations for radiative heat rate similar to Eq. (2.7), yet none is available for Titan environment. Therefore, heating results for Titan only include convective heat rate.

Table 2.3. Mass fraction of N_2 and CH_4 in Titan atmosphere

		Mass fraction, c_i [59]	
Species	Value of K	Min	Max
N_2	0.11	97.8%	98.8%
CH_4 (methane)	0.08	2.2%	1.2%

Venus Heating Environment

Convective heating for Venus entry follows Eq. (2.7), and the constant k for Venus is 1.896×10^{-8} [67]. Given the available data, there exists an empirical relation for radiative heating at Venus entry. The relation was first derived by Page and Woodward [68] and the equation was taken from Lyne et al. [22] as follows:

$$\dot{q}_r = 3.07 \times 10^{-48} V^{13.4} \rho^{1.2} R_n^{0.49} \qquad \text{if } 10,000 \leq V \leq 12,000 \text{ m/s} \tag{2.9a}$$

$$\dot{q}_r = 1.22 \times 10^{-16} V^{5.5} \rho^{1.2} R_n^{0.49} \qquad \text{if } 8,000 \leq V < 1,000 \text{ m/s} \tag{2.9b}$$

$$\dot{q}_r = 3.33 \times 10^{-34} V^{10.0} \rho^{1.2} R_n^{0.49} \qquad \text{if } V < 8,000 \text{ m/s} \tag{2.9c}$$

where $\dot{q}_r$ is the radiative heating rate in W/cm^2. It is important to note Eq. (2.9a) is also used for estimating radiative heating for velocities higher than 12,000 m/s, which may result in inaccurate heating estimates; but should be sufficient for preliminary design purposes.

Uranus Heating Environment

Since Uranus and Neptune have very similar atmospheric composition—H_2 and He dominated atmosphere, the heating relation for Uranus follows the same for Neptune heating environment which was developed at NASA Ames Research Center for 2005 Neptune probe study [69]:

$$\dot{q}_c = 2.2401 \times 10^{-7} \sqrt{(0.291/R_n)} \rho^{0.4521} V^{2.6918} \tag{2.10a}$$

$$\dot{q}_r = 2.8699 \times 10^{-63} (0.291/R_n) \rho^{0.4981} V^{15.11} \tag{2.10b}$$

2.3.3 TPS Materials

TPS materials protect the vehicle from aerodynamic heating by absorbing the heat and/or carrying the heat away from ablation. There are two types of TPS materials:

reusable and ablative. The former is usually used on reusable manned vehicles, such as the Space Shuttle, and can only sustain a low heat rate (<100 W/cm^2). The Space Shuttle employed a unique high-L/D vehicle design which allowed the use of non-ablative TPS material, i.e., reinforced Carbon-Carbon Composite (RCC). Ablative TPS materials have much higher heat rate limit (up to 100,000 W/cm^2); however, vehicles lose TPS material from ablation and therefore cannot be reused without significant, typically impractical, repairs. Most human and robotics missions use ablative TPS materials. The most challenging requirements during TPS development was the Galileo probe for Jupiter entry where the expected peak heat rate is well over 10,000 W/cm^2. In support of the Galileo mission, fully dense Carbon Phenolic (CP) was used, which is the only material that can sustain such heat rate. Summarized in Table 2.4, other TPS materials that are available or are currently under development include, but not limited to: Advanced Carbon-Carbon (ACC), Phenolic Impregnated Carbon Ablator (PICA), Silicone Impregnated Reusable Ceramic Ablator (SIRCA), Toughened Uni-piece Fibrous Reinforced Oxidation-resistant Composite (TUFROC), and Heatshield for Extreme Entry Environment Technology (HEEET).

Peak stagnation-point heat rate (measured in W/cm^2) and total stagnation-point heat load (measured in J/cm^2) are two key parameters when designing an entry vehicle. Stagnation-point heating environment can be used as a guideline for worst-case heating on an entry vehicle; however, worst-case heat rate during flight may exceed the predicted stagnation-point heat rate due to turbulent flow (example of MSL switching from SLA-561V to PICA [72]); nevertheless, the following dissertation assumes stagnation-point values for peak heat rate and refers the two parameters in short as peak heat rate and total heat load throughout.

Peak heat rate represents the highest heat rate exposed to the entry vehicle and limits the types of TPS material that can be used. For example, if the required or expected maximum heat rate is 1000 W/cm^2, one must select the TPS material that is capable of sustaining a higher heat rate. Table 2.4 summarizes densities of some TPS materials and their maximum allowable heat rate ($\dot{q}_s$) and pressure. Total heat

Table 2.4. Summary of TPS material properties [10, 17, 70]

		Performance Limit	
Material	Density, g/cm^3	Maximum $\dot{q}_s$, W/cm^2	Pressure, atm
Shuttle Tiles	0.192–0.352	44	
SRAM Family (ARA)[a]	0.224–0.32	∼100	∼1
SRAM 14 (ARA)	0.224	∼100	
SRAM 17 (ARA)	0.272	∼100	
SRAM 20 (ARA)	0.32	∼100	
SIRCA	0.192–0.352	∼150	>1
Acusil I	0.48	∼100	
TUFROC	Varies	∼300	
SLA-561V	0.256	100–200	<0.3
AVCOAT		∼900	∼1
PICA	0.256	>1400	∼0.3
PhenCarb-20 (ARA)	0.32	1000–4000	>1
HEEET	0.3–1.4	∼7,000 (tested [71])	
Carbon phenolic (CP)	1.45	100,000 (flown 30,000)	≫1 (flown 7)

[a]ARA: Applied Research Associate.

load (aka. integrated heat load) is the heat accumulated on the surface of the vehicle through the atmospheric pass. Total heat load drives the required mass of the ablative TPS material. The higher the total heat load, the more TPS mass is required. A power regression model was fitted to the data from past missions (as shown in Fig. 2.5) and the equation relating the TPS mass fraction, $\mathrm{MF}_{\mathrm{TPS}}$, and total heat load, J_s, is as follows [70, p. 124]:

$$\mathrm{MF}_{\mathrm{TPS}} = 0.091 J_s^{0.51575} \tag{2.11}$$

It is worth noting that Eq. (2.11) is empirical and is applicable only for low-L/D rigid aeroshell with ablative TPS materials; therefore should be used with caution. Nevertheless, Eq. (2.11) captures the trend that total heat load drives the TPS mass fraction.

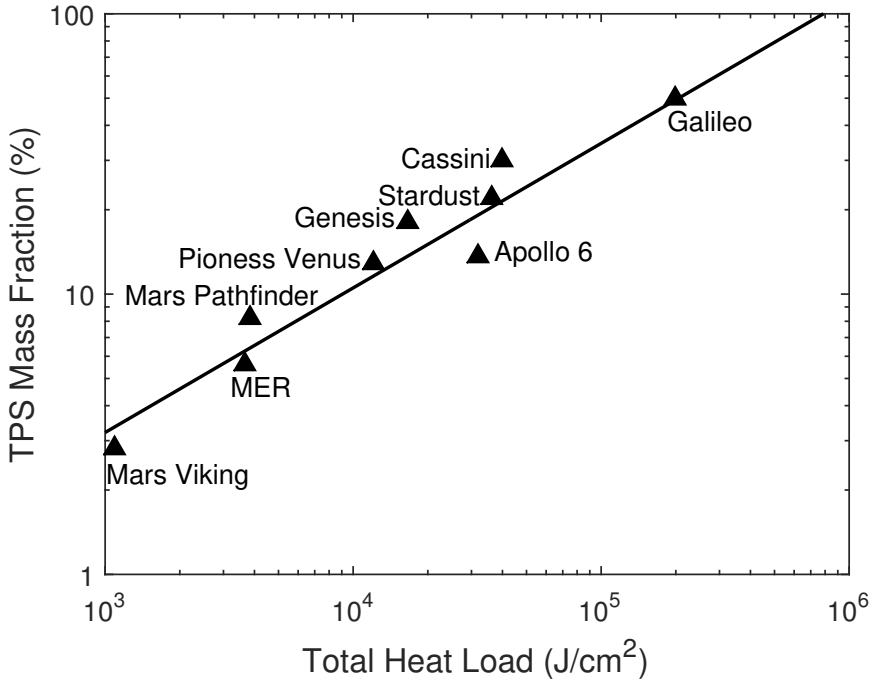

Figure 2.5. TPS mass fraction is a linear function of total heat load in log-log scale [70]. The higher the total heat load, the higher the TPS mass fraction. Lower TPS mass fraction is preferred to increase the useful payload mass fraction.

2.4 Arrival Condition and Post-Capture Orbit

Interplanetary trajectory design for missions to the outer Solar System is primarily driven by gravity-assist options which vary by launch date. There exist many possible interplanetary trajectories and mission designers can perform trades on metrics such as time of flight and delivered mass. One can use more propellant to accelerate the spacecraft more and achieve a shorter time of flight at the expense of less delivered mass. Generally, a shorter time of flight results in a higher arrival V_∞. For arrival at planets, the arrival V_∞ depends solely on the interplanetary trajectory. However, for moon encounter, particular Titan, the arrival time can be adjusted so that Titan is at different positions in orbit which allows the spacecraft to arrive at a range of V_∞ with a single interplanetary trajectory.

The analysis of interplanetary trajectories uses a single parameter, arrival V_∞, to represent the arrival conditions. Arrival V_∞ is related to entry velocity V_e as follows:

$$V_e^2 = V_\infty^2 + \frac{2\mu_p}{r_e} \tag{2.12}$$

where r_e is the entry altitude. One can use proper transformation matrices to convert inertial entry velocities into velocities in other reference frames, such as atmosphere-relative entry speed. However, the effects of wind and body rotation are not considered.

Mission designers, along with the science team would select the post-capture orbit based on the science goals and objectives as well as engineering constraints. Titan atmosphere stretches to over 1300 km. To sustain the orbiting altitude without expending any propellant, the spacecraft must be in orbit with a periapsis altitude of at least 1300 km. Titan Saturn System mission concept study used a circular orbit of 1500 km as the target science orbit [73] whereas Titan Explorer flagship mission study selected a circular orbit of 1700 km [74]. A 1700 km circular orbit is considered as the target science orbit for Titan.

For Venus, a low circular orbit of 400 km is used as the target orbit which provides the opportunity for accurate measurement for onboard instruments. For Uranus, a

5-day elliptical orbit of 20,000 km by 577,000 km is used which allows the opportunity for observing the natural satellites of Uranus.

By banking towards one side during aerocapture, the vehicle can actively change orbit inclination which otherwise requires additional propellant using propulsive capture. With one interplanetary trajectory, (namely one V_∞ vector), a small deflection maneuver can adjust the arrival trajectory to target different points on the B-plane. Figure 2.6 shows that there exists a circle of entry targets on the B-plane for a constant entry flight-path angle. B-plane is a coordinate system centered on the target body with unit vectors $\hat{R}$, $\hat{S}$, and $\hat{T}$, where $\hat{S}$ is in the direction of arrival V_∞, $\hat{T}$ parallel to the ecliptic plane and normal to $\hat{S}$, and $\hat{R}$ in the direction defined by $\hat{S} \times \hat{T}$. The center point in Fig. 2.6 represents an entry flight-path angle of -90 deg and for illustration purpose, an arrival V_∞ of 5 km/s is used to plot the contour lines of constant flight-path angles. The magnitude of B-plane targeting vector is:

$$B = \sqrt{R^2 + T^2} = \mu / V_\infty^2 \sqrt{(1 + V_\infty^2 r_p / \mu) - 1} \tag{2.13}$$

where R and T are the component of the B-plane targeting vector along $\hat{R}$ and $\hat{T}$ respectively.

Figure 2.7 shows a visualization of the circle of entry points from Fig. 2.6. Titan's obliquity relative to the ecliptic plane is 26.73 deg as shown in Table 2.5. Orbit inclination, i is a function of both entry latitude, ϕ_e, and entry heading, χ_e, as $\cos i = \cos \phi_e \cos \chi_e$. Arriving at a high latitude guarantees a high inclination, yet prohibits the spacecraft from achieving a low inclination. As shown in Fig. 2.7, there is a locus of entry points to choose using one single interplanetary trajectory and one entry flight-path angle. Each entry point has a different combination of entry latitude and entry heading; thus the locus of entry points provides a wide range of initial orbit inclination, with the minimum inclination constrained by the arrival declination.

Arrival declination is the angle between the normal vector to the B-plane (i.e., V_∞ vector) and the equatorial plane of the target body. Depending on the required entry flight-path angle and arrival V_∞, a different pre-capture orbit inclination can be achieved. Note that the arrival declination is the minimum inclination achievable.

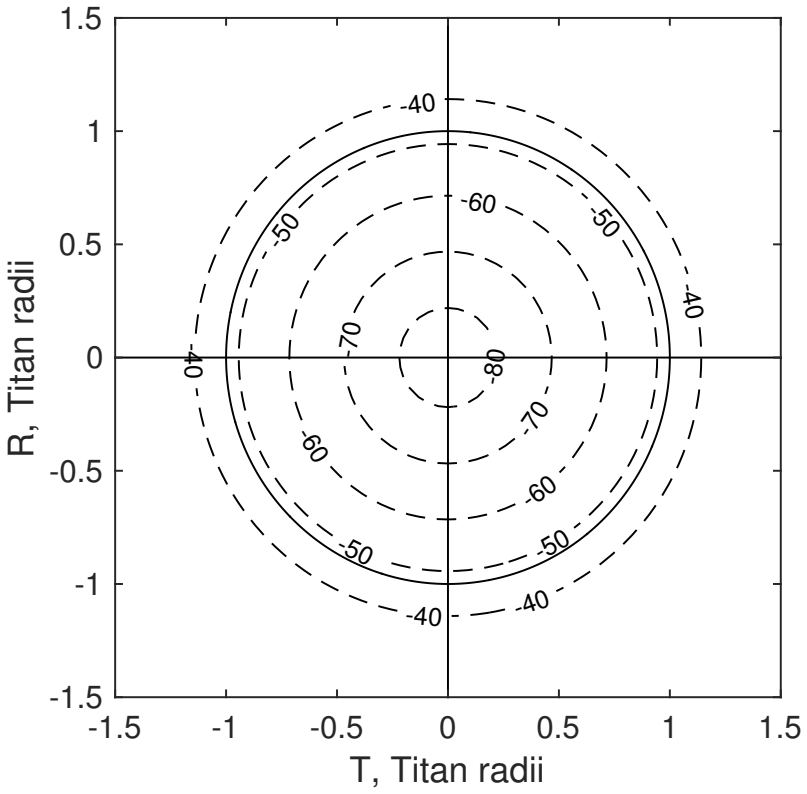

Figure 2.6. B-plane entry targeting shows points with the same entry flight-path angle form a circle (concentric dashed circles). Solid line indicates the radius of Titan [75].

Table 2.5. Orbital parameters for Titan and Saturn

Planet	Titan	Saturn
Semi-major axis	1.222 $\times 10^6$ km	1.433 $\times 10^9$ km
Inclination	0.365 deg[a]	2.49 deg[b]
Obliquity[b]	26.73 deg	26.73 deg

[b]Relative to the ecliptic plane.

[a]Relative to Saturn's equator.

From the science perspective, a high inclination orbit may be preferred in order to achieve global coverage of the body; Strange et al. [73] considered a circular orbit with 85 deg inclination for Titan. The performance analysis in Chapter 3 also assesses the capability of performing inclination changes with aerocapture by simulating the trajectories with banking angle from 0–180 deg and examine the corresponding inclination changes.

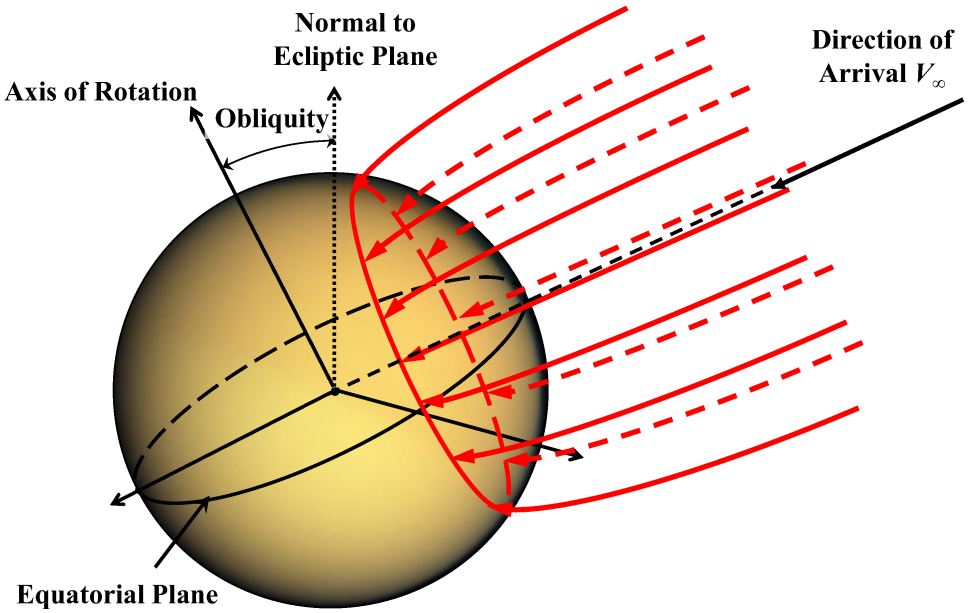

Figure 2.7. The red solid and dashed lines form a locus of constant entry flight-path angles relative to the target body using a single arrival V_∞. The locus shows a range of arrival conditions (i.e., longitude and latitude).

3. AEROCAPTURE PERFORMANCE ANALYSIS FOR TITAN, VENUS, AND URANUS

This chapter demonstrates the application of the integrated aerocapture design methodology described in Chapter 4.2. Three particular bodies are selected—Titan, Venus, and Uranus; each representing a moon, an inner planet, and an outer planet. More importantly, there are significant scientific interests to explore all three bodies. The results are presented in the form of performance analysis of mission using aerocapture to Titan, Venus, and Uranus, and extensive design rules and relations are discussed in detail.

3.1 Aerocapture Performance Analysis for Titan

3.1.1 Science Case for Titan

The moon of Saturn—Titan, is the only celestial body other than Earth known to harbor stable surface liquids. It is also the only world in the Solar System beyond Earth that is shielded from deadly radiation, and harbors a benign, but extremely cold, environment with a nitrogen-dominated atmosphere. Titan's atmosphere experiences a wide range of dynamical and chemical processes, and varies seasonally in temperature and composition. Surface liquids act as a natural collection system for the global organic inventory, and noble gases which upon investigation could provide new insights into organic chemical evolution on a global scale and detect ongoing biological processes [76]. Impact craters, tectonics, cryovolcanism, fluvial and lacustrine erosive processes have played a role in shaping Titan's icy surface. And evidence of the surface shaped by rain, rivers, and wind points to an active meteorological cycle involving liquid methane that mimics water cycle on Earth [76]. Titan's surface fea-

tures bear a surreal resemblance to Earth's, and Fig. 3.1 shows Cassini RADAR map of Titan's surface where features of rivers and lakes can be clearly identified. Huygens' probe from Cassini-Huygens' mission, landed 10°S on Titans surface on January 14, 2005. The probe Descent Imager and Spectral Radiometer (DISR) has recorded an astonishing view of Titan surface beneath the haze that presents very similar geology to Earth's ridges, mountains, lakes, shorelines, and even liquid channel. Figure 3.2 is a colorized photo showing round icy cobblestones on the surface of Titan that provide evidence of liquid flows in the past around the landing site.

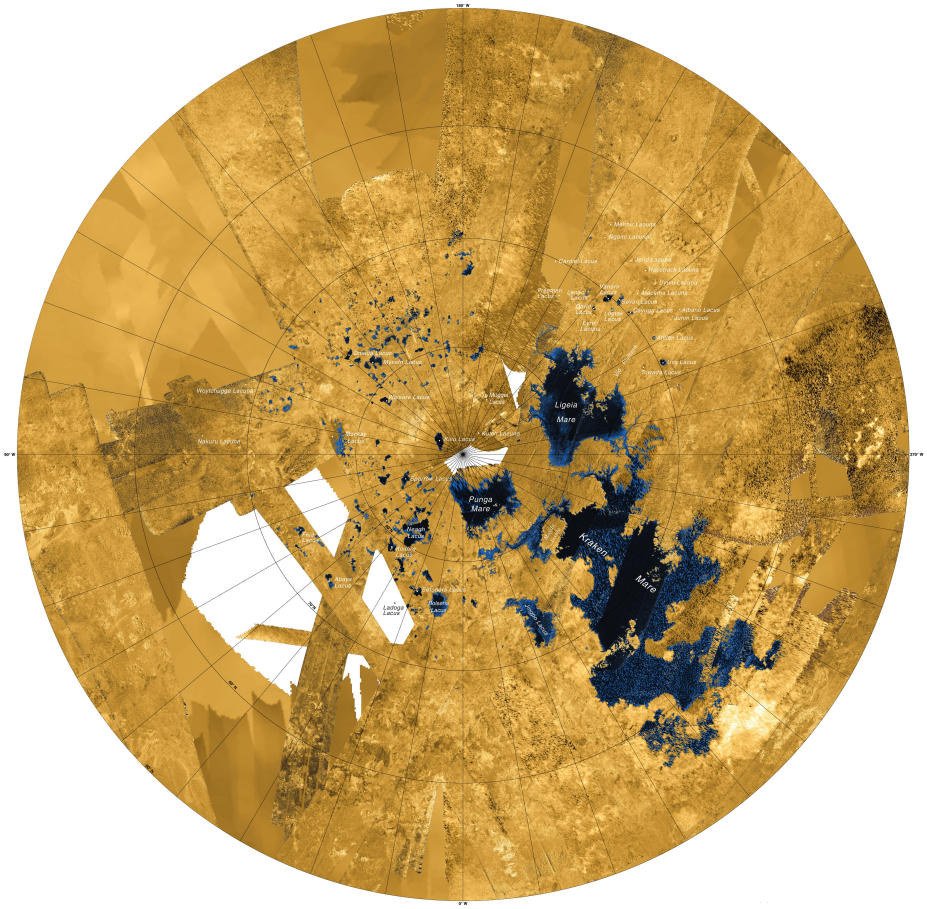

Figure 3.1. Cassini RADAR image of Titan surface in the northern hemisphere (Credit: NASA) shows methane lakes, rivers, and shoreline features.

In the 2017 Announcement of Opportunity (AO) for New Frontiers program, studies of Ocean worlds (i.e., Titan, Enceladus, or Europa) have been given priority; in comparison, the 2013–2022 Decadal survey did not consider missions to Titan as a high priority objective. In the New Frontiers AO, the science goals for Titan are: (1) to understand the organic and methanogenic cycle on Titan, especially as it relates to prebiotic chemistry, (2) to investigate the subsurface ocean and/or liquid reservoirs, particularly their evolution and possible interaction with the surface.

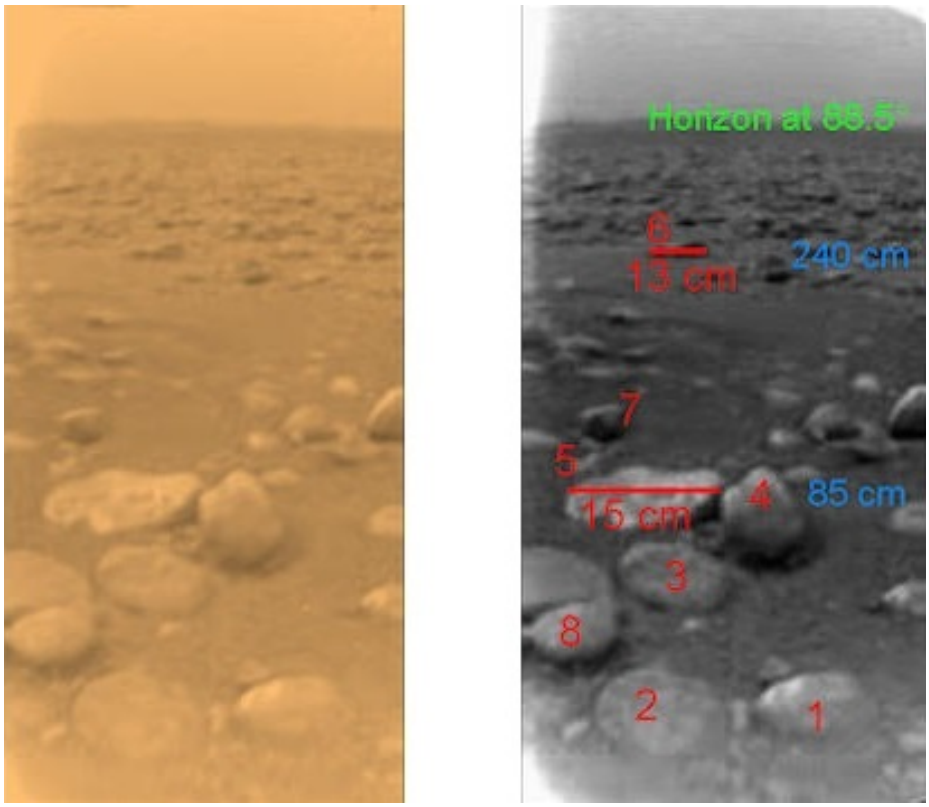

Figure 3.2. Image of Titans surface from Huygens (Credit: NASA/ESA).

Upon the return of the Cassini data, interest in sending follow-on missions to Titan have increased. Numerous studies have been proposed to investigate Titan in further detail, in which different platforms can be used either alone or in combination thereof: orbiter, surface lander, lake lander, aerial platforms, and mobility systems [1518]. The Applied Physics Laboratory at Johns Hopkins University conducted a Titan Explorer

Flagship Mission Study in 2007 that includes separate Orbiter, Lander, and Balloon in order to meet comprehensive science goals [74]. A mission concept study of Titan Lake Probe in 2010 proposed four mission concepts ranging from New-Frontiers class to Flagship-class missions [77]. The Flagship-class mission includes a relay orbiter, a lake lander, and a submersible. The other three are New Frontiers-class missions: (1) a floating lake lander with direct-to-Earth communication, where a similar concept was also proposed in another study—Titan Mare Explorer (TiME) [78], (2) a relay orbiter with a submersible, and (3) a relay orbiter with a floating lake lander, which is also proposed in the Titan Saturn System Mission (TSSM) concept study [79].

3.1.2 Entry Corridor Width

Theoretical corridor width (TCW) is a measure of the control authority of an entry vehicle and is defined as the range between the maximum and minimum allowable entry flight-path angles (γ_{max} and γ_{min} in Fig. 1.1):

$$\text{TCW} = |\gamma_{max} - \gamma_{min}| \tag{3.1}$$

Vehicles can actively control its trajectory during entry via two means: bank angle control of lifting vehicle [8] and drag modulation [30]. Results in this chapter only consider the former. γ_{max} is the steepest angle at which the vehicle can enter a desired transfer orbit while pointing the lift vector fully upwards; whereas γ_{min} is the shallowest angle while pointing the lift vector fully downward. The transfer orbit can then be modified to the target science orbit with two propulsive ΔV maneuvers: one to raise the periapsis altitude of post-aerocapture orbit, and another to adjust the final apoapsis altitude; however, the latter is needed only if the aerocapture maneuver produces some error in periapsis altitude.

Theoretical corridor width depends on both arrival condition (i.e., V_∞) and vehicle designs (i.e., ballistic coefficient, β and L/D). While theoretical corridor width measures the vehicle's control authority, required corridor width determines the desired control authority and is driven by the delivery error incurred during interplanetary

navigation and guidance, uncertainties in vehicle aerodynamics, and uncertainties in atmosphere models. Figure 3.3 shows the breakdown of the required corridor width for Titan aerocapture to each of the error/uncertainty source [10]. Required corridor widths for case noted as 6.5 km/sec and 10 km/sec are derived with only pre-Cassini knowledge. Note that 6.5 km/s and 10 km/s are inertial entry velocities at 1000 km altitude, which correspond to arrival V_∞ of 6.10 km/s and 9.75 km/s respectively. Cases denoted EOC ephemeris refer to the required corridor widths with updated ephemeris data from Cassini, whereas cases denoted EOC ephemeris, atmos refer to the required corridor widths with updated ephemeris and atmospheric data from Cassini. For spacecraft to successfully perform aerocapture, the designed theoretical corridor width must exceed the required corridor width, otherwise, the vehicle risks skipping out of Titan gravity.

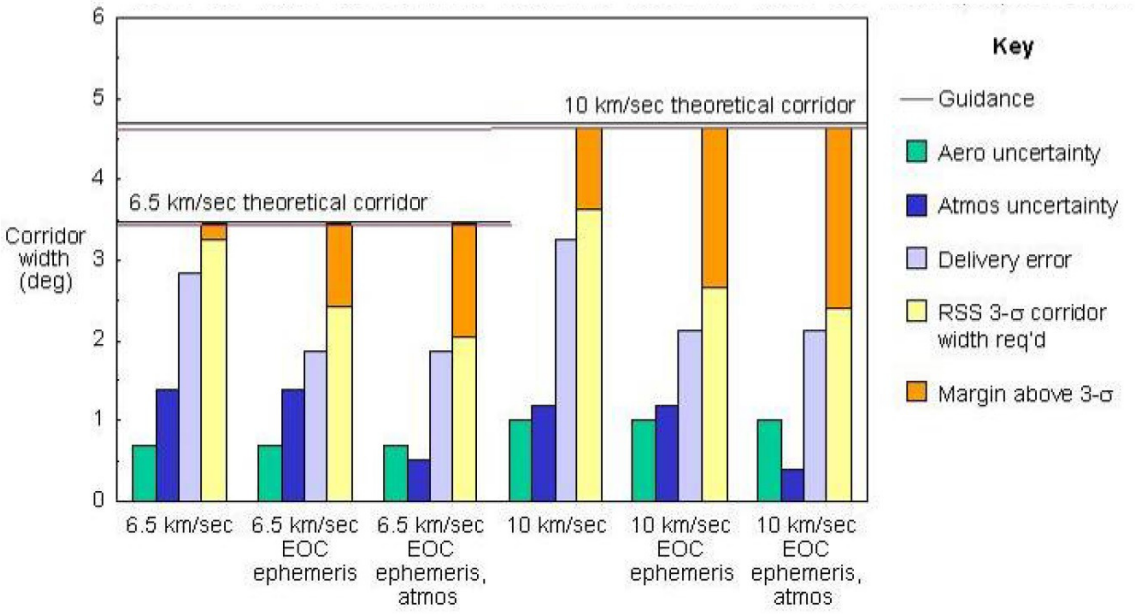

Figure 3.3. Robustness for Titan aerocapture [10]. Contribution breakdown for six scenarios shows the required corridor width of 3.5 deg and 4.5 deg for entry velocities of 6.5 km/s and 10 km/s respectively.

Figures 3.4 and 3.5 show the contour plots of theoretical corridor width for $\beta =$ 90 and 800 kg/m^2 respectively with L/D from 0 to 1 and arrival V_∞ from 0 to 16 km/s. The contours show that if a vehicle with L/D of 0.1 arrives at Titan with V_∞ of 3 km/s, the vehicle will not have enough control authority to guarantee the success of orbit insertion using aerocapture. Note that the choice of two ballistic coefficients represents the upper and lower limits. $\beta = 90$ kg/m^2 is a realistic value [10] and $\beta =$ 800 kg/m^2 is a theoretical maximum. The worst-case required corridor width of 3.5 deg for $V_\infty = 6.10$ km/s and 4.5 deg for $V_\infty = 9.75$ km/s from Fig. 3.3 are chosen as two reference points and they are marked as circles in Figs. 3.4 and 3.5. The required corridor width constrains either the lowest arrival V_∞ for a specific vehicle L/D or the lowest vehicle L/D for a specific arrival V_∞. Increasing either V_∞ or vehicle L/D increases the theoretical corridor width. Given a required corridor width, there exists a combination of arrival V_∞ and vehicle L/D. From Figs. 3.4 and 3.5, the minimum required L/D is between 0.2 and 0.3, which corresponds to vehicle designs, such as spherical aeroshell, sphere-cone shape, ADEPT, or HIAD.

3.1.3 Peak G-load

Peak deceleration (g-load) is one of the driving factors in aerocapture system design and is constrained by vehicle structure and on-board instruments. Figure 3.6 shows the effect on peak g-load from vehicle aerodynamics, arrival V_∞, and bank angle selection. For lift-up case ($\sigma = 0$ deg), peak g-load varies slightly with respect to the targeted post-capture orbital period. The longer the orbit period, the smaller the peak g-load. With the same target post-capture orbit, flying the vehicle lift-up results in a higher g-load than flying lift-down. The range of peak g-load between lift-up and lift-down cases for L/D = 0.2 is smaller than that for L/D = 0.4. Note that vehicle with higher L/D has a higher control authority and can fly at a wider range of trajectories, thus resulting in a theoretically higher g-load. While no vehicle will

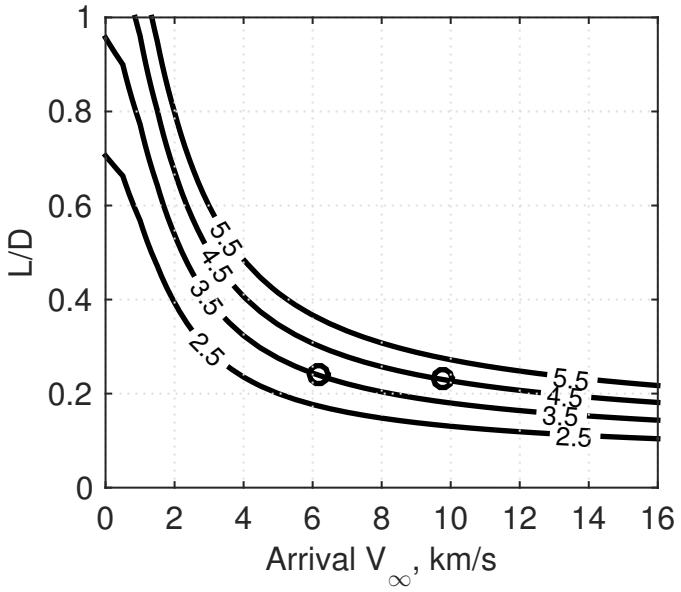

Figure 3.4. Theoretical corridor width for $\beta = 90$ kg/m^2. Two circles denote the required corridor width of 3.5 deg and 4.5 deg. The required vehicle L/D is 0.24.

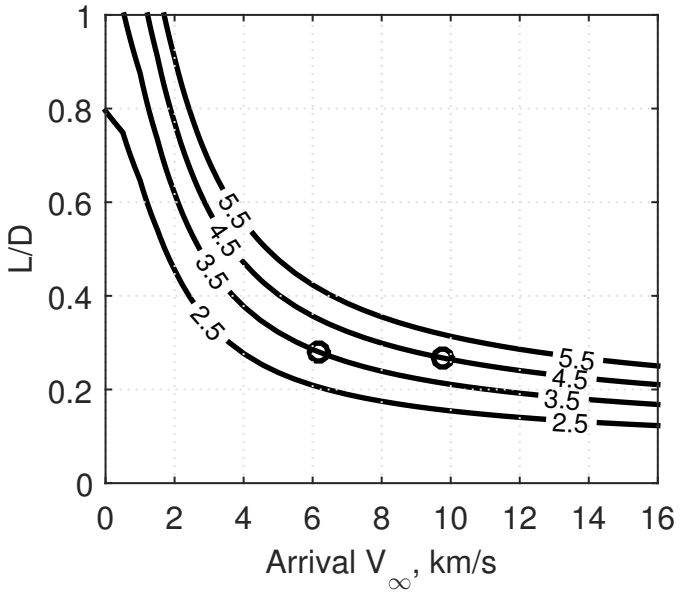

Figure 3.5. Theoretical corridor width for $\beta = 800$ kg/m^2. Two circles denote the required corridor width of 3.5 deg and 4.5 deg. The required vehicle L/D is 0.28.

never fly at the trajectory with the worst g-load, with proper trajectory optimization and guidance algorithm, a vehicle with higher L/D usually achieves a lower g-load.

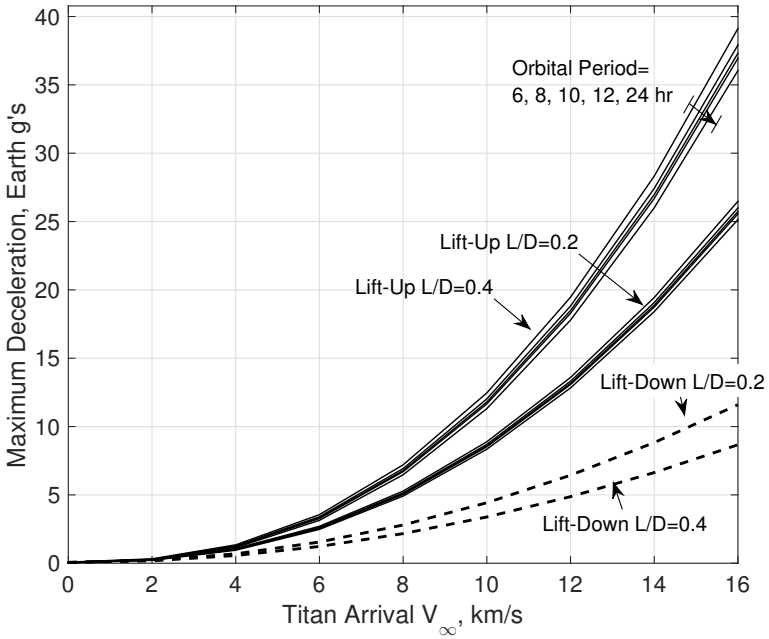

Figure 3.6. Peak g-load as a function of arrival V_∞ shows that peak g-loads are different for lift-up and lift-down cases and different vehicle configurations (L/D of 0.2 and 0.4).

Figure 3.7 shows contours of constant g-load values where the values are the worst-case deceleration when the vehicle points its lift vector fully upward. From the shape of contour lines in Fig. 3.7, vehicles with higher L/D allow a lower arrival V_∞. The solid and dashed lines differ only by a small amount; therefore, the ballistic coefficient has a small effect on the peak g-load. As the vehicle maneuverability (i.e., L/D) increases, the corresponding maximum V_∞ is reduced; however, it is important to note that since only the worst-case results are presented, higher L/D does not necessarily mean that the g-load is higher in a realistic situation.

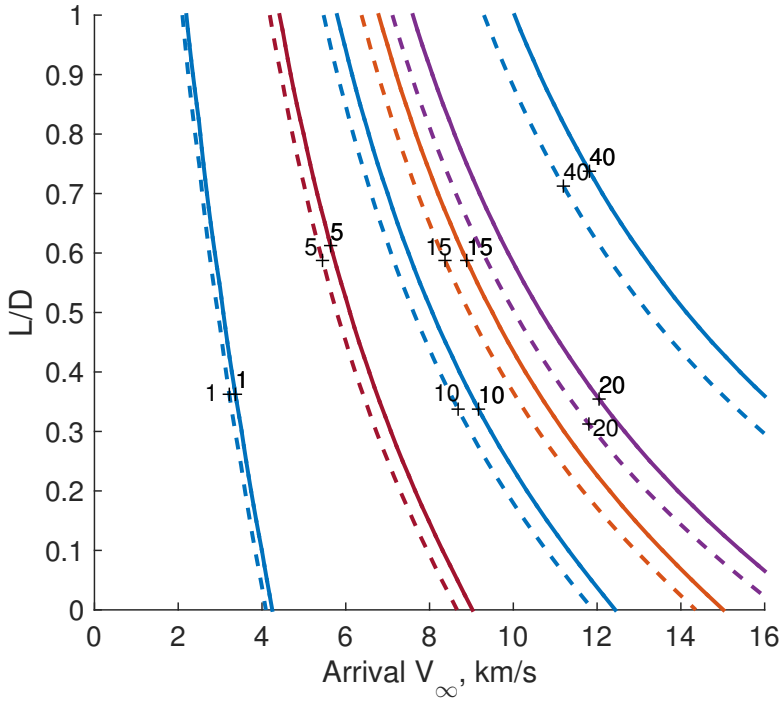

Figure 3.7. Contour lines of peak g-load for $\beta = 90$ kg/m^2 (solid lines) and 800 kg/m^2 (dashed lines) shows the effect of vehicle L/D and arrival V_∞. High ballistic coefficient shifts the contour lines slightly towards the left.

3.1.4 Peak Heat Rate and Total Heat Load

As discussed in Section. 2.3.2, peak heat rate, and total heat load are two important parameters to consider during the conceptual design process: peak heat rate drives the selection of TPS materials, and the total heat load drives the mass fraction of TPS materials. Figure 3.8 shows the heat rate profiles at four constant bank angles with target apoapsis altitude of 1700 km, $V_\infty = 10$ km/s, $\beta = 800$ kg/m^2, and L/D = 0.3. Peak heat rate occurs a few minutes after the vehicle enters the atmosphere. $\sigma = 0$ deg and $\sigma = 180$ deg correspond to the full lift-up and full lift-down cases respectively.

Figure 3.8 shows that the larger the constant bank angle profile, the lower the peak heat rate. The worst-case heat rate results are presented in the following sections, i.e., the lift-up case. Note that for the target apoapsis altitude, the entry flight-path angles are also different with different for constant bank angle profiles.

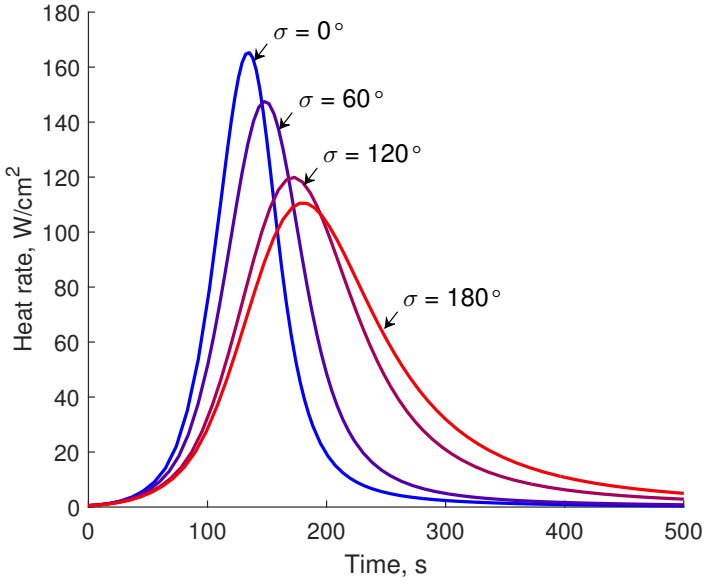

Figure 3.8. Heat rate profiles for arrival $V_\infty = 10$ km/s, $\beta = 90$ kg/m^2, and L/D = 0.3 shows that peak heat rate occurs at $\sigma = 0$ deg.

Figure 3.9 shows the total heat load results for bank angles from 0 to 180 deg at both β of 90 and 800 kg/m^2 with arrival V_∞ = 10 km/s and L/D = 0.3. Total heat load varies differently from peak heat rate with respect to bank angle. Maximum total heat load occurs at the lift-down case when the bank angle is 180 deg for both β of 90 and 800 kg/m^2. Similarly, only the maximum total heat load is presented, that is when $\sigma = 180\,\text{deg}$.

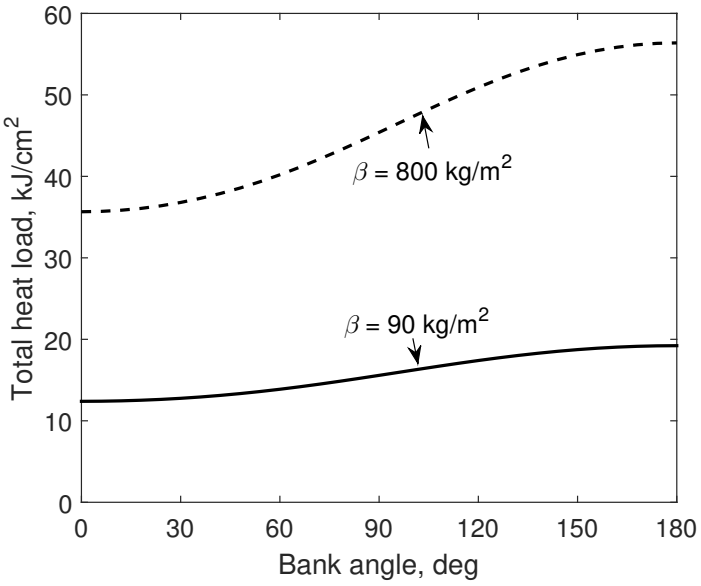

Figure 3.9. Total heat load with vehicle ballistic coefficients of 90 and 800 kg/m^2. Both cases show peak heat load occurs at σ = 180 deg.

For entry studies, the trade-off between total heat load and peak heating rate is a key consideration—entering the atmosphere at a steeper flight-path angle lowers the total heat load (thus the mass fraction of TPS materials), yet increases the peak heat rate; and vice versa. As illustrated in Fig. 1.1, to capture the vehicle in orbit, aerocapture requires a particular range of entry flight-path angles as determined by γ_{max} and γ_{min}; therefore, entry flight-path angle cannot be adjusted for trade studies of peak heat rate and total heat load.

Atmospheric uncertainty has very small effects on the heating conditions as shown in Fig. 3.10. The heat rate profiles for both lift-up and lift-down cases are very close for minimum, nominal, and maximum atmosphere. The minimum and maximum atmospheres are only different in density profiles from the nominal and the atmospheric compositions are the same. The minimum and maximum atmosphere is ±60% in density from the nominal at an altitude of 1500 km and ±5% at 0 km. The entry flight-path angle for either minimum and maximum atmosphere use the same as the nominal case for both lift-up and lift-down cases.

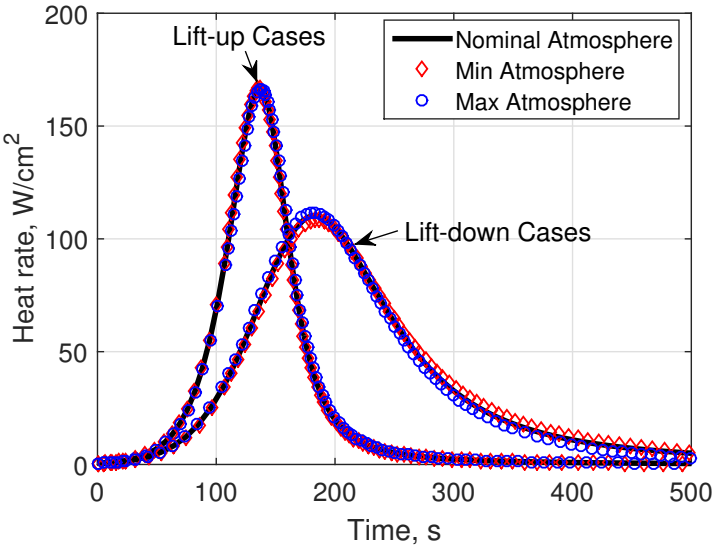

Figure 3.10. Heat rate profiles for both lift-up and lift-down cases at minimum, nominal, and maximum atmosphere shows a very small change in heating conditions from atmospheric variability.

From Figs. 3.11 and 3.12, dashed contour lines for $\beta = 800$ kg/m^2 are on the left-side of the same valued solid contour lines for $\beta = 90$ kg/m^2; meaning that same peak heat rate and total heat load for $\beta = 800$ kg/m^2 occur at a lower arrival V_∞ compared to that for $\beta = 90$ kg/m^2. Both peak heat rate and total heat load increase with a higher ballistic coefficient. Considering the state-of-the-art TPS technologies, the peak heat rate is well within that limit. From Table 2.4, HEEET has a heat rate

limit of over 7000 W/cm^2 which is higher that the expected peak heat rate at V_∞ of 16 km/s for both β of 90 and 800 kg/m^2. Total heat loads of 10, 30, and 50 kJ/cm^2 correspond to TPS mass fractions of 10%, 18%, and 24% using 2.11. Comparing these values to the fuel mass fraction of 70% (assuming $\Delta V = 3.5$ km/s and specific impulse, $I_{sp} = 300$s), the TPS mass fraction for aerocapture is within a reasonable range.

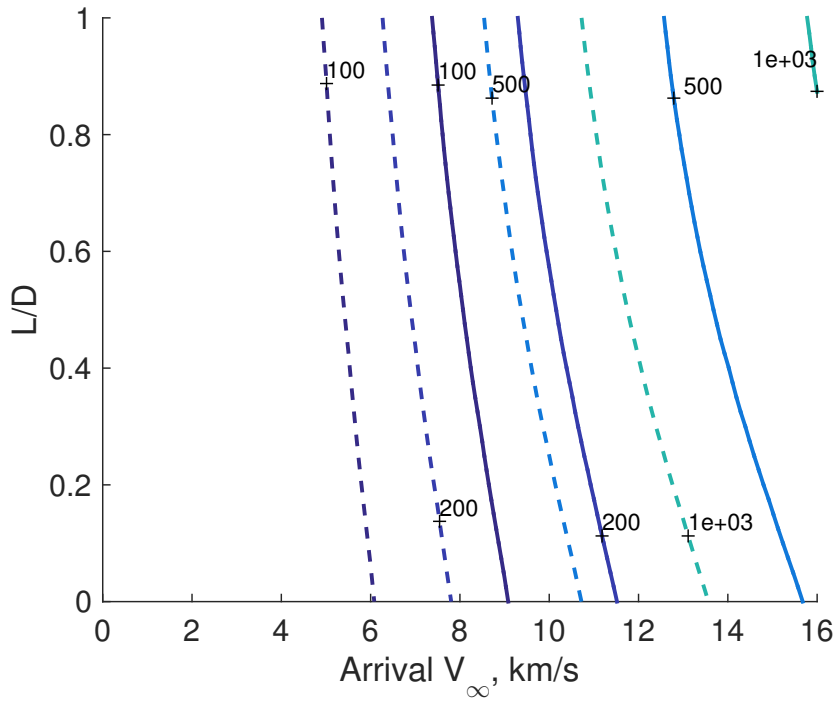

Figure 3.11. Contour lines of peak heat rate (in W/cm^2) for $\beta = 90$ kg/m^2 (solid lines) and 800 kg/m^2 (dashed lines) shows the effect of vehicle L/D and arrival V_∞. Results shown correspond to lift vector pointed fully upwards.

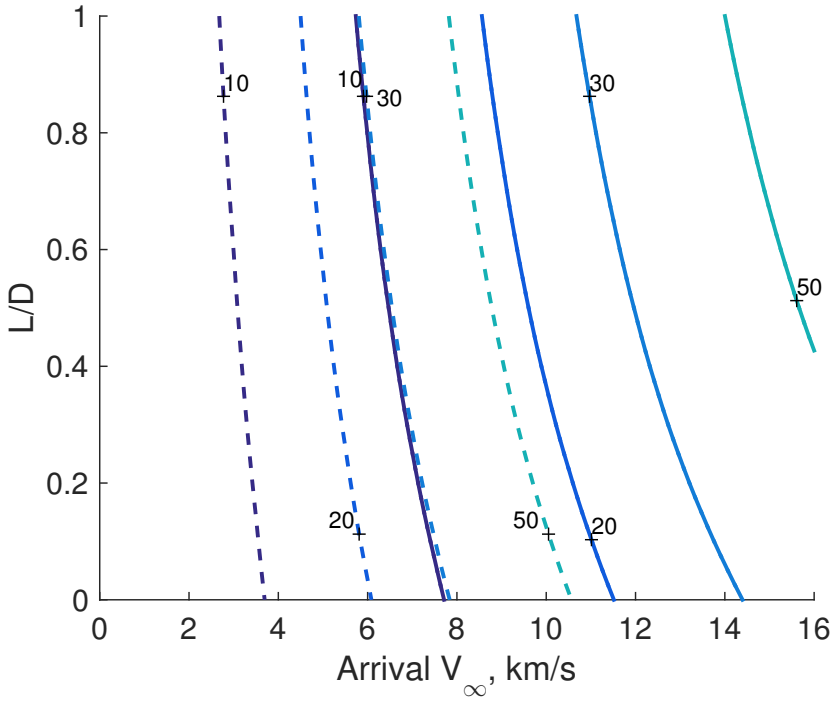

Figure 3.12. Contour lines of total heat load (in kJ/cm^2) for β = 90 kg/m^2 (solid lines) and 800 kg/m^2 (dashed lines) shows the effect of vehicle L/D and arrival V_∞. Results shown correspond to lift vector pointing fully downwards.

The heating results only include convective heating as no radiative heating relations exist for Titan. To give an order-of-magnitude estimates for radiative heating, results from Olejniczak et al. [80] can provide some rough relations for convective and radiative heat rate and heat load as shown in Table. 3.1. Depending on the vehicle configuration, predicted peak radiative heat rate is roughly 1.5 to 3.5 times that for convective, and the total heat load from radiative heating is roughly 1.5 to 2.5 times that from convective. Note that Olejniczak et al. [80] used the atmosphere model from Yelle et al. [58] which was shown to have overestimated the mass fraction of CH_4 and a more accurate model is given by Waite et al. [59]. As discussed in Section 2.3.2, the abundance of CH_4 greatly affects the radiative heat rate and lower mass

fraction of CH_4 results in a lower radiative heat rate. Therefore, the realistic radiative heat rate may be less than the values shown in Table 3.1.

Table 3.1. Comparisons of radiative and convective peak heat rate and total heat load from Olejniczak et al. [80]

Case	Peak heat rate, W/cm^2		Total heat load, J/cm^2	
	Radiative	Convective	Radiative	Convective
1	124	39	10200	5500
2	84	29	12090	7500
3	43	28	18400	7700
4	149	41	10580	5200
5	100	30	12480	7600

3.1.5 Aerocapture Feasibility Plot

Combining all constraints in a single plot, shown in Fig. 3.13, the area shaded green is the applicable region of aerocapture at Titan, assuming a required corridor width of 3.5 deg, a peak g-load constraint of 10 Earth g's, peak heat rate of 100 W/cm^2, and total heat load limit of 30 kJ/cm^2. The required corridor width determines the lower limits on arrival V_∞ and vehicle L/D, whereas peak g-load, peak heat rate, and total heat load determine the upper limits on arrival V_∞ and vehicle L/D. If the limits on g-load and heat rate increase to 20 Earth g's and 200 W/cm^2 respectively, the applicable region is expanded by the area shaded yellow. As the vehicle design constraints is relaxed, a higher arrival V_∞ may be possible; however, the minimum required vehicle L/D decreases by only a very small amount.

Traditional rocket propulsion can provide orbit insertion ΔV up to 3.5 km/s, which corresponds to an arrival V_∞ using the following equation:

$$\Delta V_{\text{burn}} = \sqrt{V_\infty^2 + \frac{2\mu_p}{r_t}} - \sqrt{\frac{\mu_p}{r_t}} \tag{3.2}$$

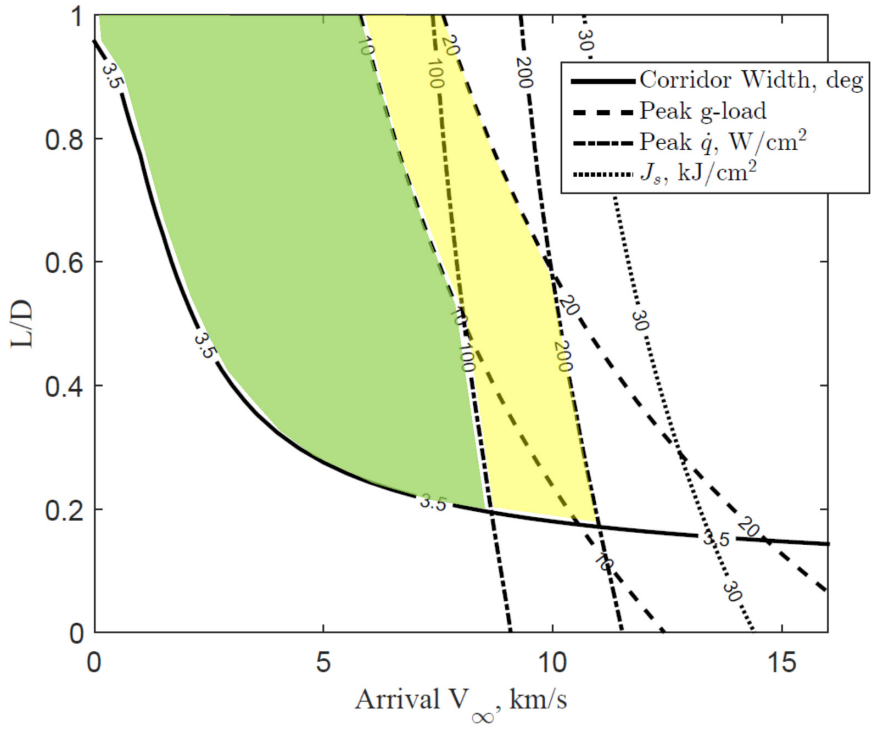

Figure 3.13. Aerocapture applicable region (shaded green) with a required corridor of 3.5 deg, g-load constraint of 10 Earth g's, peak heat rate of 100 W/cm^2, and total heat load of 30 kJ/cm^2. The area shaded yellow denotes the expansion of aerocapture applicable region when increasing the peak heat rate to 200 W/cm^2 and g-load to 20 Earth g's.

where r_t is the target orbit radius. Assuming a 1700 km circular science orbit, propulsive options can achieve orbit capture at a maximum arrival V_∞ of 4.5 km/s at Titan (assuming maximum ΔV of 3.5 km/s). There exist other alternate options for which the spacecraft is first captured around Saturn, then followed by Titan orbit insertion leveraging aerobraking [73] or gravity-assist options [81]. Here only considers ΔV values for direct orbit insertion.

Figures 3.14 and 3.15 show that the region where aerocapture is feasible for different constraints on heating and g-load. Both plots summarize four constraints, required corridor width, peak g-load, peak heat rate, and total heat load. Note selections of values of the peak heat rate, and total heat load are different for $\beta = 90$ kg/m^2 and $\beta = 800$ kg/m^2. With $\beta = 800$ kg/m^2, higher peak heat rate and heat load are expected. The chemical region is boxed in both plots. Aerocapture applicable region overlaps with chemical region only when the vehicle has higher L/D; however, a lower L/D is a preferred vehicle configuration. Thus for low-L/D (<0.3) configuration, there is no overlapping area between chemical capture and aerocapture. In addition, aerocapture allows an arrival V_∞ of 16 km/s or higher.

For a particular vehicle L/D, theoretical corridor width sets the lowest arrival V_∞ where aerocapture can be applied; whereas peak g-load, peak heat rate, and total heat load limit the highest achievable arrival V_∞. A vehicle with L/D = 0.2 using traditional spherical section aeroshell has been proven and flown at Earth and Mars. A higher vehicle L/D may present an increased challenge in system complexity. Reducing the required corridor width is so-far the only way to lower the required vehicle L/D. With the updated ephemeris and atmosphere models from Cassini data, as shown in Fig. 3.3, required corridor widths for arrival V_∞ of 6.10 km/s and 9.75 km/s are 2 and 2.5 deg respectively; therefore, a vehicle with L/D of 0.2 can be a viable option for aerocapture at Titan.

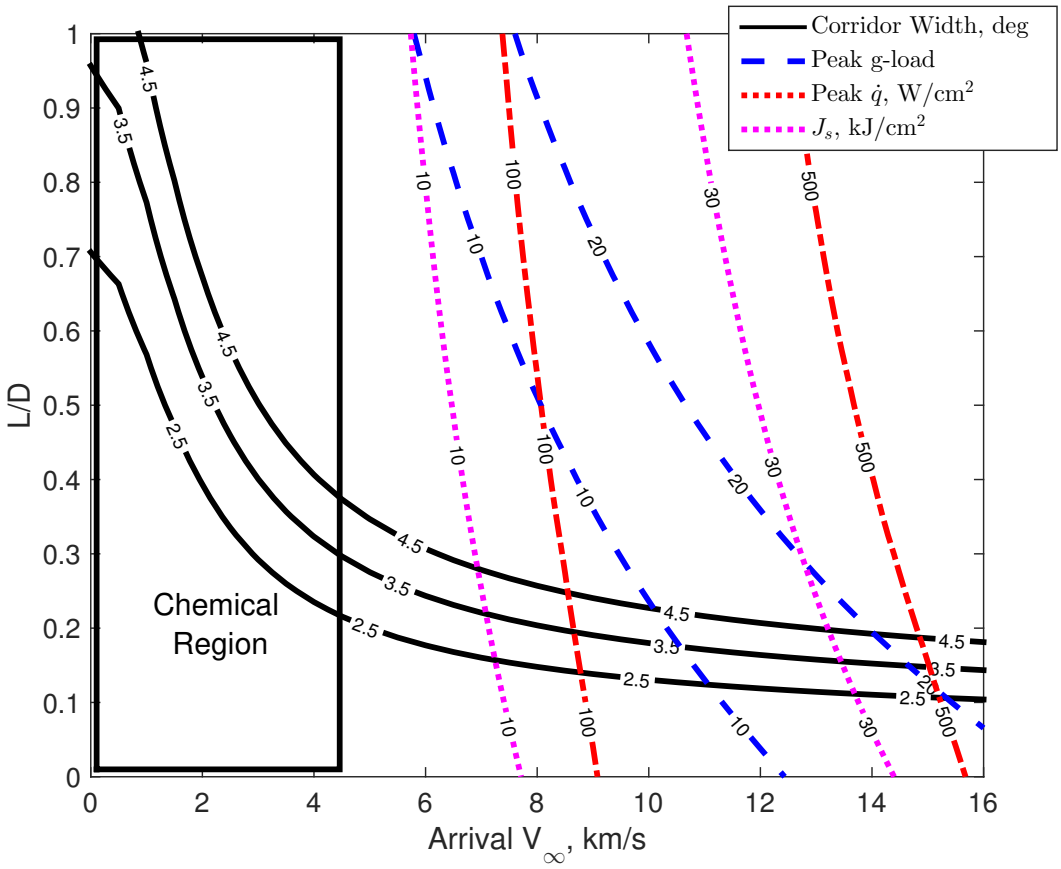

Figure 3.14. Constraints summarized in a single plot for $\beta = 90$ kg/m^2.

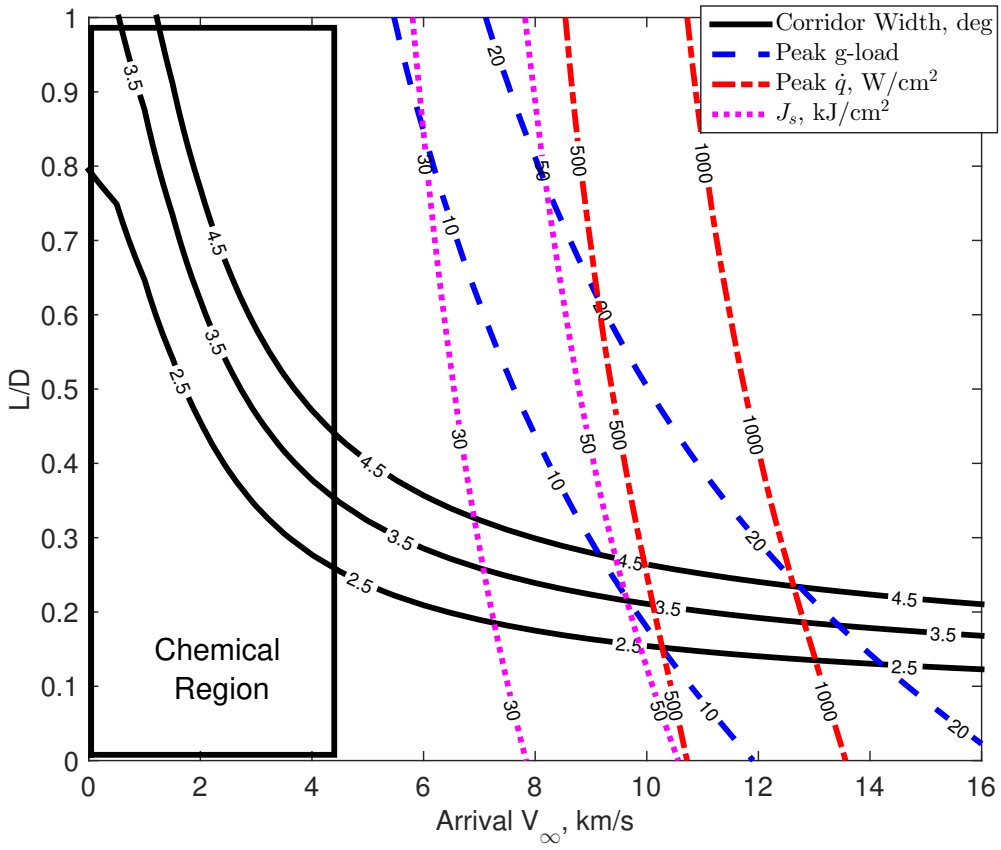

Figure 3.15. Constraints summarized in a single plot for $\beta = 800$ kg/m^2.

3.1.6 Post-aerocapture Trajectory Correction Maneuver

Post-capture orbit has periapsis inside the atmosphere; the spacecraft needs to perform trajectory correction maneuvers (TCM) after aerocapture to achieve the desired science orbit. Two scenarios of TCM are described here: (1) first one at the exit of atmospheric phase to correct the apoapsis altitude; and second at the apoapsis to raise the periapsis altitude; (2) one at the post-aerocapture apoapsis to raise the periapsis altitude; and second at the apoapsis to correct the periapsis altitude. The first approach ensures the successful capture of the spacecraft and is a preferred method if the theoretical corridor width is smaller than the required corridor

width (e.g., in cases where the vehicle has less than the required L/D). Although it is unlikely to be the case for Titan aerocapture, the first approach remains as an alternative. The second approach follows the traditional orbit transfer maneuvers where TCM are performed at apsides. Post-capture TCM may have a significant ΔV requirement. To characterize the ΔV required to correct the post-capture orbit, Figs. 3.16 and 3.17 show the contour lines of upper and lower limit on the required ΔV to achieve 1700 km circular orbit with $\beta = 90$ kg/m^2. Figure 3.16 shows that ΔV of at least 140 m/s is required using a vehicle with L/D of 0.3. In Fig. 3.17, for arrival V_∞ less than 15 km/s, the required ΔV using vehicle L/D of 0.3 is at most 300 m/s. Similar to how peak heat rate varies with vehicle L/D, the upper limit on the required ΔV increases with increasing vehicle L/D. Recall that increase of vehicle maneuverability (i.e., L/D) results in a wider range of trajectories. Realistic values of required ΔV can be better estimated using guidance algorithm along with Monte Carlo simulations.

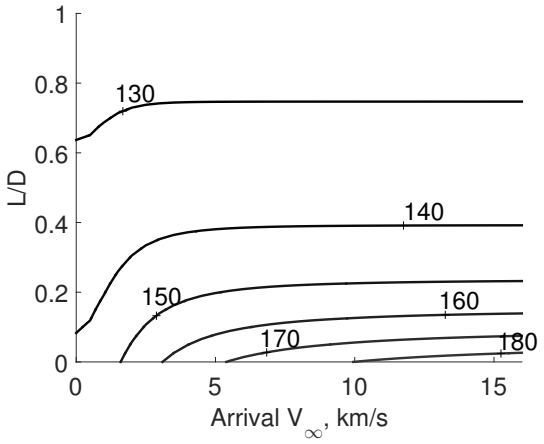

Figure 3.16. Lower limit on the required ΔV (in m/s) to achieve 1700 km circular orbit shows that a minimum of 100 m/s is required.

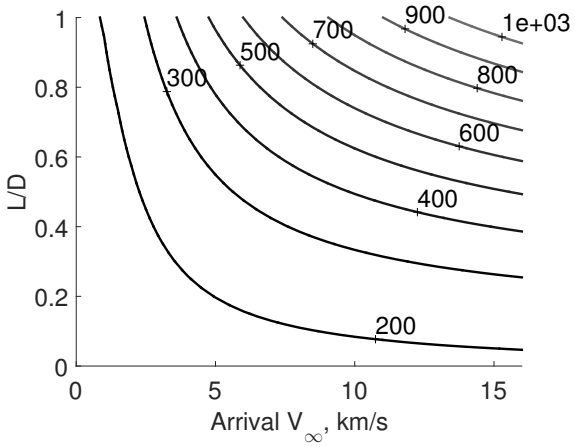

Figure 3.17. Upper limit on the required ΔV (in m/s) to achieve 1700 km circular orbit shows that required ΔV at low-L/D is less than 400 m/s.

3.1.7 Inclination Change

Aerocapture maneuver allows inclination changes via banking maneuvers (pointing the lift vector away from the vertical and consistently towards one side). Figure 3.18 shows the maximum inclination changes at arrival V_∞ from 5 to 15 km/s with target orbit periods from 6 hours to 2 days. Each curve consists of simulation results with banking angles from 0 to 180 deg. The maximum inclination change occurs at a banking angle of 90 deg. The simulation assumed that the vehicle enters at 0 deg latitude with a heading of 0 deg. An arrival V_∞ of 10 km/s is highlighted at target orbit of 6 hr period. The maximum inclination change is 18 deg which, however, corresponds to a constant banking angle of 90 deg, which means that any disturbances would prevent the vehicle from achieving such inclination change. The green line in Fig. 3.18 denotes a 2-deg difference in entry flight-path angle which represents the required corridor width. An inclination change of 15 deg can be achieved. With an arrival V_∞ of 15 km/s and a target orbit period of 6 hrs, the vehicle can achieve an inclination change of 20 deg. As discussed in Section 2.4, it is preferred that the science orbit has a high inclination, and also that the inclination of the pre-capture

orbit cannot be lower than the arrival declination, yet there is no upper limit for pre-capture orbit inclination. If the vehicle arrives at a low declination (<15 deg), the spacecraft can achieve any inclination by simply targeting particular points on the arrival locus as shown in Fig. 2.7.

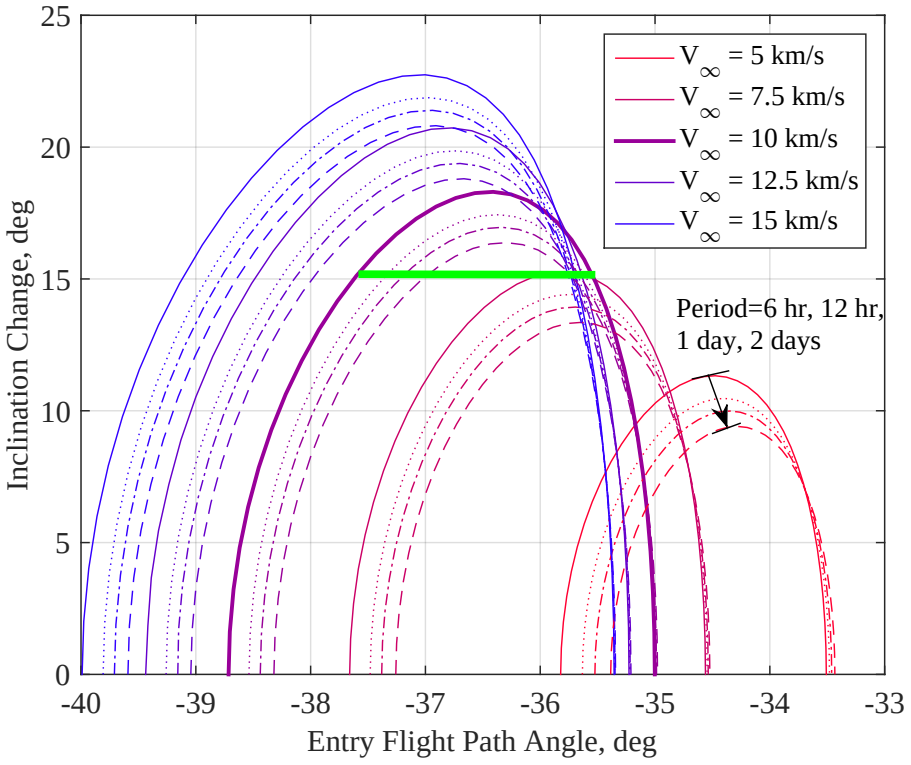

Figure 3.18. Inclination change at different arrival V_∞ and final orbital period. Green line shows the 2-deg corridor width on the plot. An inclination change of more than 10 deg can be achieved.

3.2 Aerocapture Performance Analysis for Venus

3.2.1 Science Case for Venus

Venus, as the most popular target for gravity-assist, presents unique exploration opportunities. The Venus Bridge Study [82] considered low-cost candidate concepts including CubeSats, SmallSats, in-situ element such as lander and balloon, all of which have delivered payload less than 200 kg. For a low-cost mission, ride-along options with spacecraft that are using Venus for gravity-assist either for exploring the heliosphere or the outer planets, are particularly attractive. However, the ΔV requirements for orbit insertion and particularly a tight orbit using chemical propulsion can be prohibitive. Aerocapture could be an alternative for mass-efficient orbital missions.

Previous work by Craig and Lyne [24] performed parametric studies for Venus aerocapture, in which they considered an Apollo-style entry vehicle with L/D of 0.2 and 0.35, and an arrival V_∞ of 4–10 km/s. A NASA study on Venus aerocapture [16] considered a single interplanetary trajectory with V_∞ of 2.88 km/s and proposed a reference point-design for Venus aerocapture vehicle. While they have shown aerocapture at Venus is feasible, the results in this section present a more thorough aerocapture performance analysis over a broader range of arrival V_∞ and vehicle designs—arrival V_∞ from 0–30 km/s, L/D from 0–0.4, and ballistic coefficients of 50 and 500 kg/m^2. The two values of ballistic coefficients, 50 and 500 kg/m^2 represent the reasonable upper and lower limits of ballistic coefficients for Venus aerocapture.

3.2.2 Theoretical Corridor Width

Figure 3.19 shows the contours of theoretical corridor width for aerocapture at Venus for two values of ballistic coefficients: 50 and 500 kg/m^2. Since the two contour curves are very close to each other in Fig. 3.19, the theoretical corridor width only varies slightly with the ballistic coefficients; thus the effects can be considered

negligible as compared to arrival V_∞ and vehicle L/D. Assuming 1 deg of required corridor width that includes the uncertainties from guidance and control, atmosphere model, and aerodynamic model, the applicable region is above the 1-deg contour of theoretical corridor width in Fig. 3.19.

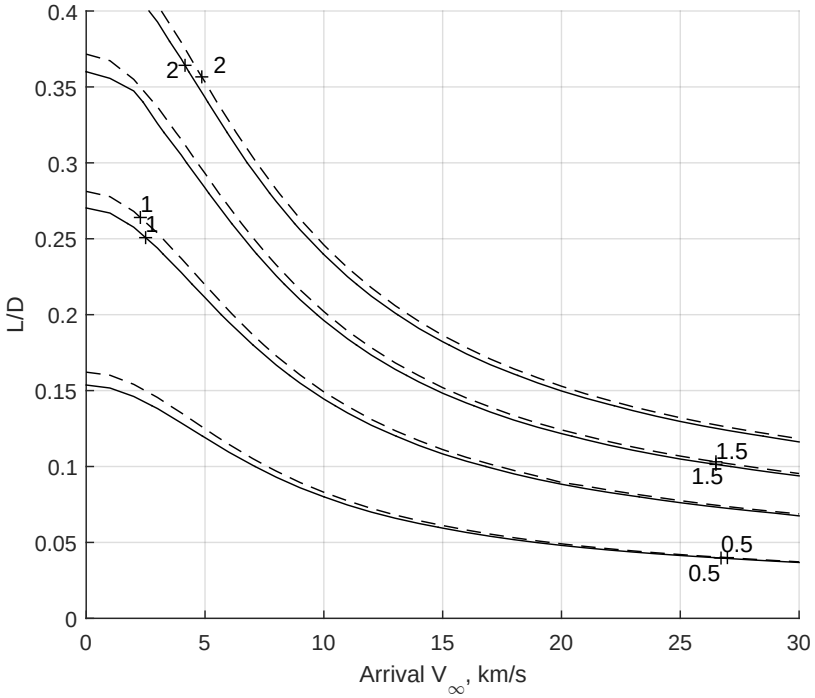

Figure 3.19. Theoretical corridor width for $\beta = 50$ kg/m^2 (solid) and $\beta = 500$ kg/m^2 (dashed).

3.2.3 Peak G-load, Peak Heat Rate, and Total Heat Load

Figure 3.20 shows the contours of peak g-load for ballistic coefficients of 50 and 500 kg/m^2. The peak g-load only varies slightly with respect to vehicle ballistic coefficient; while it changes the most significantly with respect to arrival V_∞. If given a deceleration limit of 20 g, the maximum arrival V_∞ is around 12 km/s (note that such limit does not reflect any other constraints).

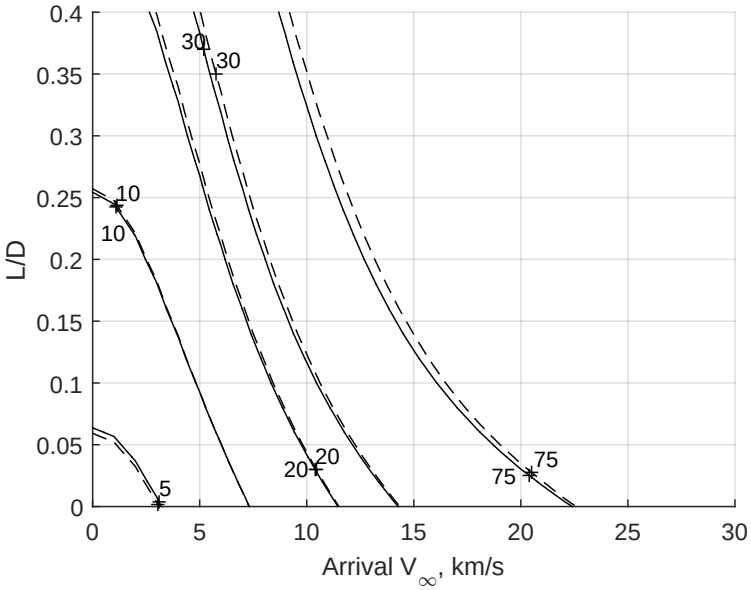

Figure 3.20. Contour of peak g-load for for $\beta = 50$ kg/m^2 (solid) and $\beta = 500$ kg/m^2 (dashed).

Figures 3.21 and 3.22 show the contours of peak heat rate and total heat load for ballistic coefficients of both 50 and 500 kg/m^2. The contours of the same level for $\beta = 500$ kg/m^2 are shifted towards right of that for $\beta = 50$ kg/m^2 in both figures. It is obvious that peak heat rate and total load vary drastically with ballistic coefficient. For total heat load as shown in Fig. 3.22, at high arrival V_∞ the contours are almost vertical and the total heat load does not depend on the vehicle L/D because the total heat load results are for full lift-down cases which are very sensitive to entry flight-path angle. A high L/D results only in a slight change in the nominal entry flight-path angle, therefore, resulting in the almost the same total heat load values for L/D from 0 to 0.4.

Similarly, the contours of peak heat rate as shown in Fig. 3.21 are relatively vertical for V_∞ of more than 5 km/s, therefore, the peak heat rate varies slightly with respect to vehicle L/D. The contours in Figures 3.21 and 3.22 do not extend over V_∞ of more than 15 km/s because the number on the contours shown represent the

realistic values—peak heat rate is limited at 5000 W/cm^2 and total heat load at 250 kJ/cm^2. Thus, any arrival V_∞ of more than 15 km/s may be infeasible due to the heat constraints. Contours in Figs 3.20, 3.21 and 3.22 show the limits at each arrival V_∞ and vehicle L/D; however, the actual peak g-load, peak heat rate, and total heat load will be smaller than the values shown.

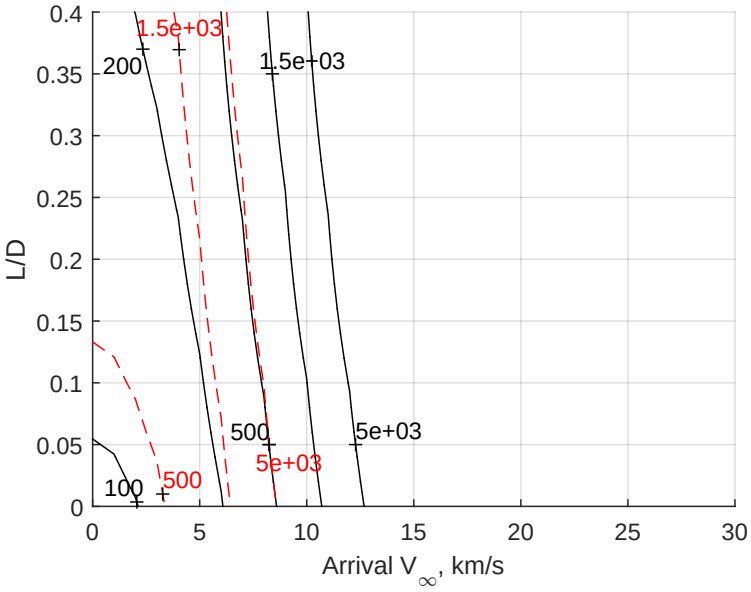

Figure 3.21. Contours of peak heat rate (W/cm^2) for $\beta = 50$ kg/m^2 (solid) and $\beta = 500$ kg/m^2 (dashed).

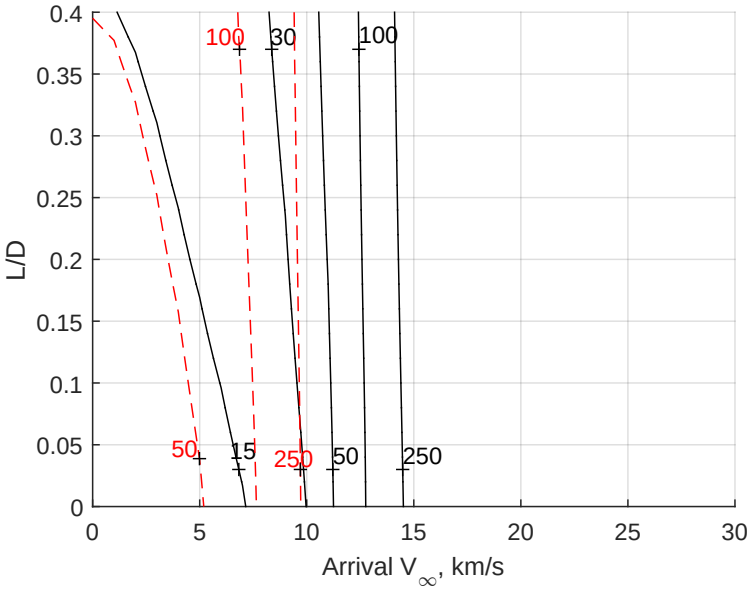

Figure 3.22. Contours of total heat load (kJ/cm^2) for $\beta = 50$ kg/m^2 (solid) and $\beta = 500$ kg/m^2 (dashed).

3.2.4 Aerocapture Feasibility Plot for Venus

Figures 3.23 and 3.24 show the feasible region of Venus aerocapture for ballistic coefficients of 50 and 500 kg/m^2 respectively. Figure 3.23 uses 1 deg of required corridor width, PICA heat rate limit, 25 % TPS mass fraction (from Section 2.3.3), and 50 g as the constraints and the corresponding highest arrival V_∞ is 10 km/s. In Fig. 3.24, 50 g-load limit and 50 % TPS mass are shown and TPS material considered is reduced density carbon phenolic (reduce CP) which can sustain a heat rate up to 25 kW/cm^2 [10]. Galileo, MESSENGER, and Cassini used Venus gravity-assist and arrived at arrival V_∞ of 9.35 km/s, 9.07 km/s, and 31.35 km/s respectively. A ride-along small-sat with L/D of 0.15 and ballistic coefficient of 50 kg/m^2 can be inserted into orbit using aerocapture.

The results are useful for mission designers to search for a wider range of trajectories which could enable more opportunities for future orbiter missions to Venus. The

environment is very benign for aerocapture at low arrival V_∞ (i.e., 3–5 km/s which is above the chemical limit); non-ablative TPS materials may be able to handle the peak heat rate and the estimated TPS mass fraction could be as low as 10%.

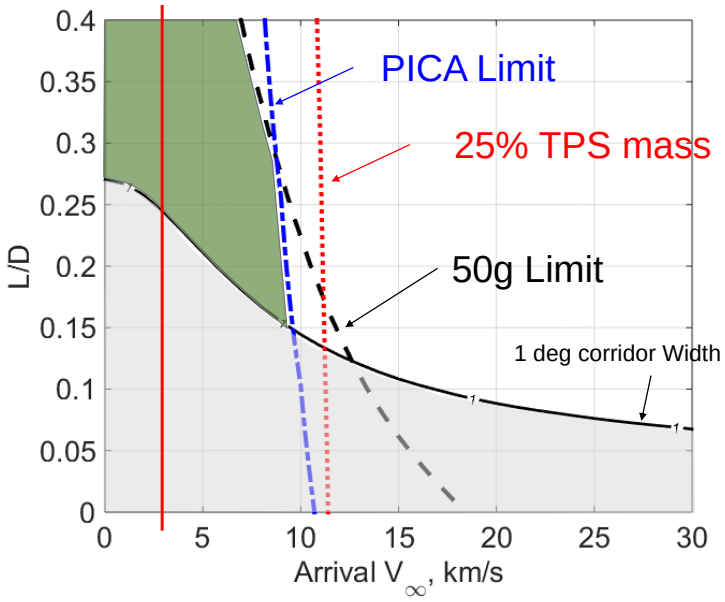

Figure 3.23. Aerocapture feasibility for Venus for $\beta = 50$ kg/m^2. Red lines mark the limit of propulsive options and green areas are the feasible region for Venus aerocapture.

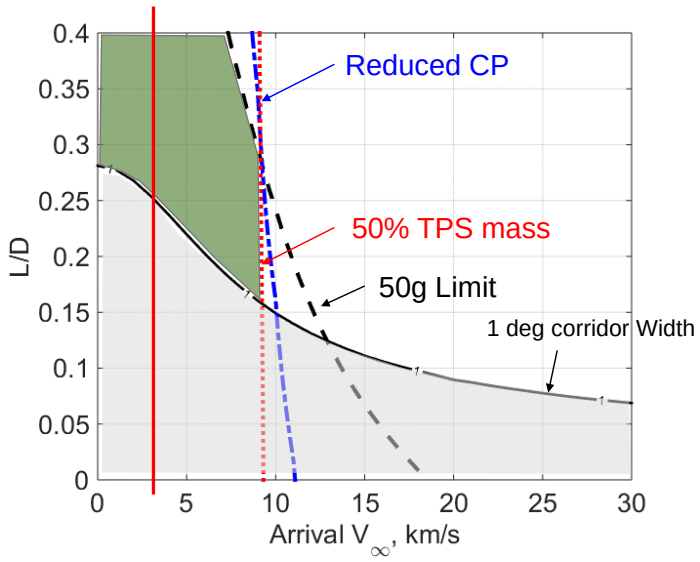

Figure 3.24. Aerocapture feasibility for Venus for $\beta = 500$ kg/m^2. Red lines mark the limit of propulsive options and green areas are the feasible region for Venus aerocapture.

3.3 Aerocapture Performance Analysis for Uranus

3.3.1 Science Case for Uranus

Ice Giants—Neptune and Uranus—as the two most distant planets in the Solar System, present challenges for robotics explorations. There are several studies for ice giant missions, including Hughes [83], the Ice giants pre-decadal study [20], and by Mansell et al. [84]. To reduce the flight times of the interplanetary travel, spacecraft arrives at a very high velocity at Uranus. A very large mass fraction of propellant required to perform orbit insertion may result in impractical delivered mass. Thus the need for aerocapture technology may be inevitable and there are numerous studies that have evaluated aerocapture system design for Neptune [17].

Compared with other planets, Uranus has very unique obliquity of 97.8 deg (as illustrated in Fig. 3.25) and due to the existence of the ring, the arrival problem becomes very complicated. It may be desirable to change inclination and line of apsides upon arrival. Aerocapture maneuver is an opportunity to perform such changes without expending any propellant. Results for Uranus aerocapture focus on the potential orbital change during aerocapture as well as capabilities of shifting of lines of apsides. The analysis considers arrival V_∞ from 5 to 30 km/s, L/D from 0 to 1, ballistic coefficients of 200 and 800 kg/m^2, and a target elliptical orbit with a period of 5 days.

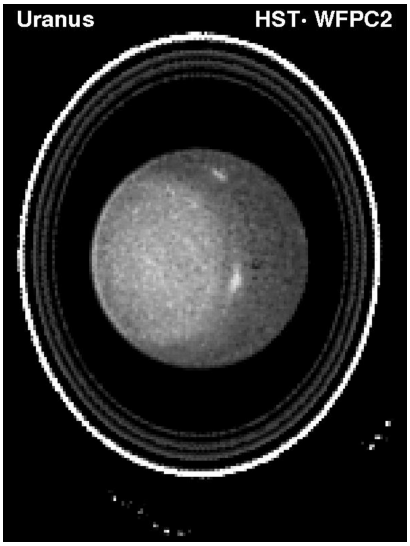

Figure 3.25. Uranus image taken by Hubble Space Telescope on August 14, 1994 (Image credit: NASA/JPL/STScI).

3.3.2 Aerocapture Feasibility Plot for Uranus

Figure 3.26 shows the required corridor width for Neptune aerocapture, and the number is used as a reference to identify the required corridor width for Uranus aerocapture. The red line denotes the guidance performance which is based on a Hybrid Predictor-corrector Aerocapture Scheme (HYPAS) guidance algorithm [85]. The margin above 3-σ between the red line and the orange region in Fig. 3.26 could be improved using an optimal guidance algorithm developed by Lu et al. [29].

Figures 3.27 and 3.28 are the aerocapture feasibility plots for Uranus aerocapture at β of 200 and 800 kg/m^2, summarizing the theoretical corridor width, peak g-load, peak heat rate, and total heat load. In Figure 3.27, contours of 0.75, 1.5 and 3 deg are shown for theoretical corridor width; 10, 20, 50, and 100 g for peak g-load; 1, 2, and 4 kW/cm^2 for peak heat rate; 250, 400, and 750 kJ/cm^2 for total heat load. For $\beta = 800$ kg/m^2 shown in Fig. 3.28, contours of the same value are shown except for total heat load which is shown for 300, 450, and 750 kJ/cm^2 (which is done for better illustration to avoid overlapping contours).

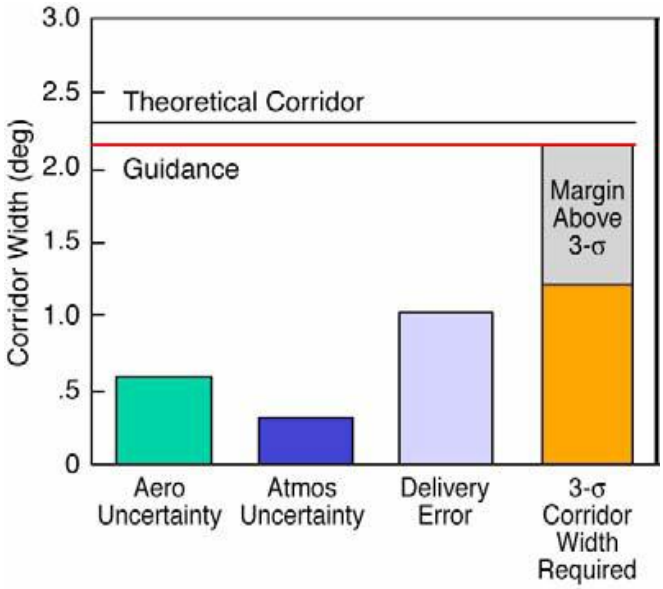

Figure 3.26. Required corridor width in the 2006 Neptune aerocapture study [10].

The primary constraint of using aerocapture at Uranus at relatively high arrival V_∞ (i.e., 20 km/s) is the total heat load. As a reference, Galileo entry probe had a total heat load of 200 kJ/cm^2 and a total of 50 % mass fraction is dedicated to the thermal protection system. Equivalently, using the rough relation as in Eq. (2.11), a total heat load of 300, 450, 750 kJ/cm^2 correspond to 61 %, 75 %, and 97 % TPS mass fraction, which is equivalent of 39 %, 25 %, and 3 % for useful payload. As 75 % mass fraction was used as a reference point for propulsive capture, a limit of 75 % can be used here and the region towards the right of the total heat load contour of 450 kJ/cm^2 would be infeasible. It is important to note that Eq. (2.11) is based on conventional rigid aeroshell and may not apply to a mid-L/D vehicle.

The peak heat rate shown is well within the heat rate limit of HEEET (8,000 W/cm^2). PICA may be sufficient for β of 200 kg/m^2, if the arrival V_∞ is below 18 km/s; and for β of 800 kg/m^2, if below 14 km/s. Assuming the required corridor width can be reduced to 0.75 deg, low-L/D vehicle (< 0.4) may be sufficient for aerocapture at Uranus. If using a vehicle with L/D of 0.4 and β of 200 kg/m^2 and arriving at V_∞ of 15 km/s, the corresponding theoretical corridor width is 1 deg, peak g-load

7.75 g, peak heat rate 961 W/cm^2, total heat load 205 kJ/cm^2 (i.e., 50 % TPS mass fraction). While using a vehicle with L/D of 0.4 and β of 800 kg/m^2 and arriving at V_∞ of 15 km/s, the corresponding theoretical corridor width is 0.88 deg, peak g-load 8.6 g, peak heat rate 1900 W/cm^2, total heat load 374 kJ/cm^2 (i.e., 68 % TPS mass fraction).

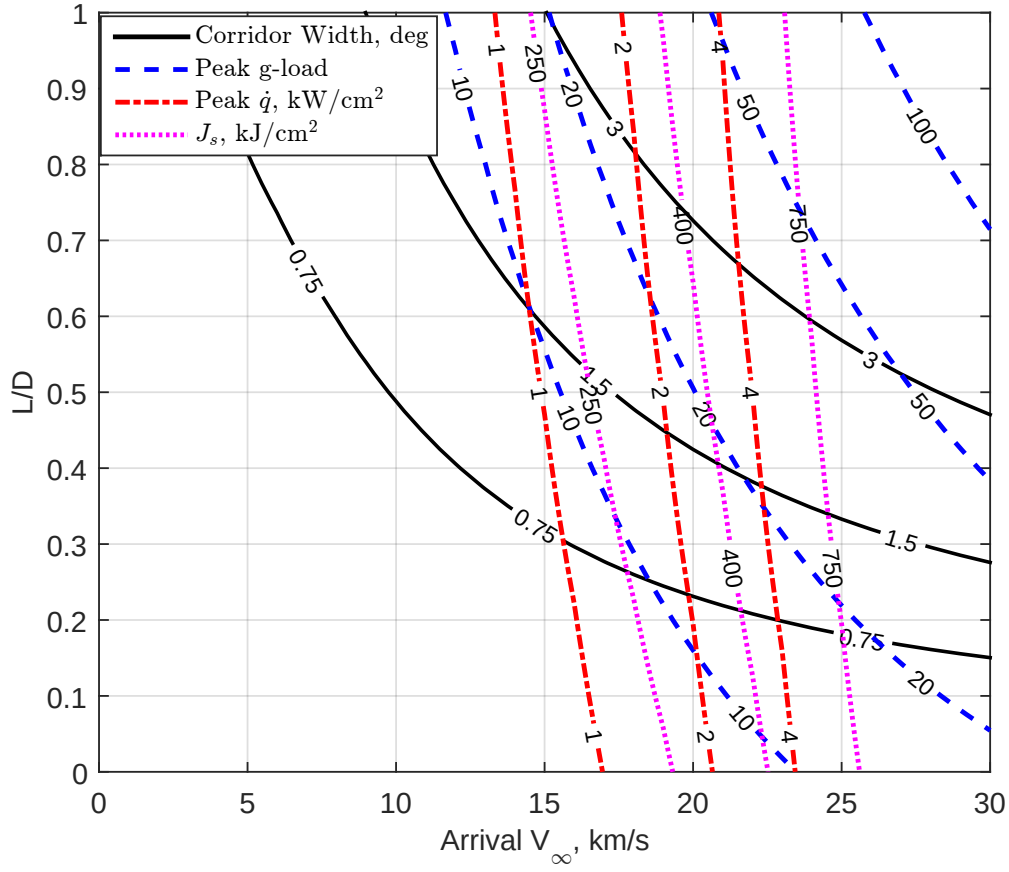

Figure 3.27. Aerocapture feasibility plot for Uranus with $\beta = 200$ kg/m^2.

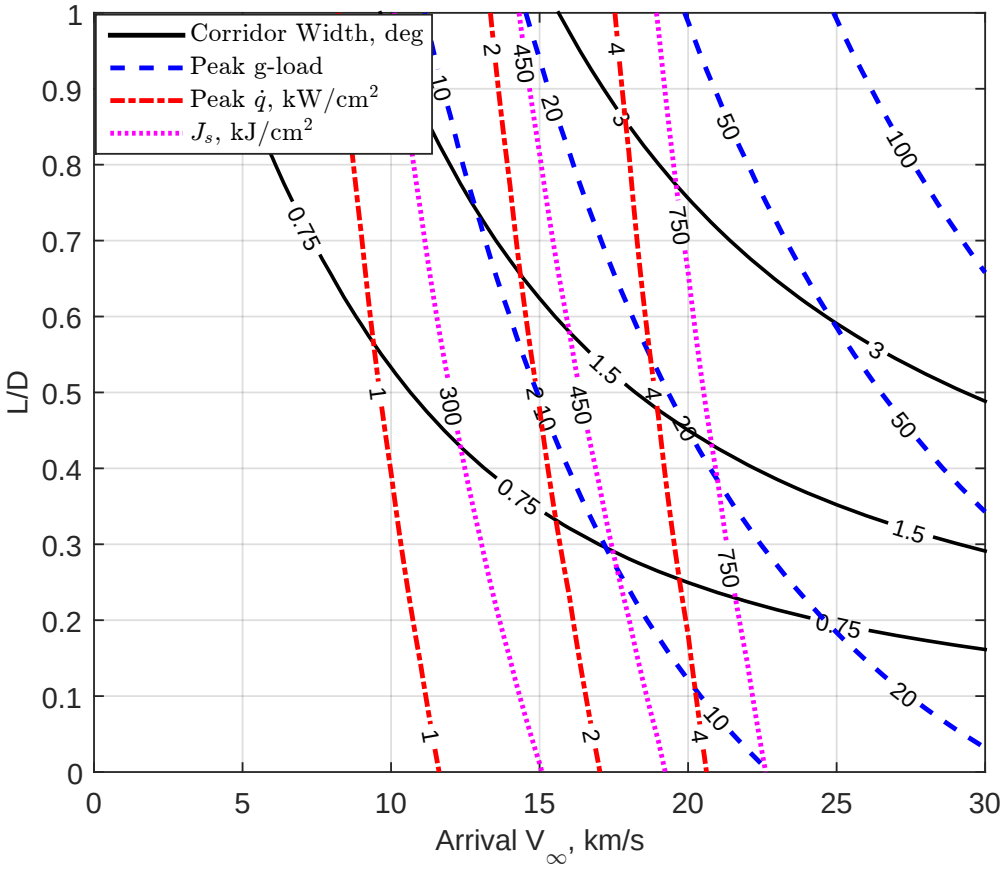

Figure 3.28. Aerocapture feasibility plot for Uranus with $\beta = 800$ kg/m^2.

3.3.3 Inclination Change

Inclination change can be achieved during Aerocapture using a lifting body by designed banking maneuver (pointing the lift vector away from the local vertical). A parametric analysis is conducted to investigate the possible inclination changes achievable during Aerocapture. Arrival V_∞, ballistic coefficient, and L/D are the three parameters of interests.

Figures 3.29(a) and 3.30(a) show that vehicle with higher L/D can achieve a higher inclination change and vehicles that arrive at a higher V_∞ can achieve a high inclination changes and the inclination changes vary proportionally as the arrival V_∞ increases. Note that the only difference between Figs. 3.29 and 3.30 are the entry conditions, i.e., the initial orbit inclination. The inclination changes, shown in Fig. 3.29 are the theoretical maximum inclination changes achievable (>25 deg) through an aerocapture maneuver. However, the entry condition is not realistic considering the risk of crossing the ring of Uranus upon arrival. Figure 3.30 assumes a more realistic arrival condition which entry Uranus atmosphere at a latitude of -74 deg with a heading of 270 deg (northward) and the corresponding max inclination change is less than 15 deg. As shown in Figs. 3.29(b) and 3.30(b), inclination changes vary only slightly at different values of ballistic coefficients, even from 50 to 800 kg/m^2.

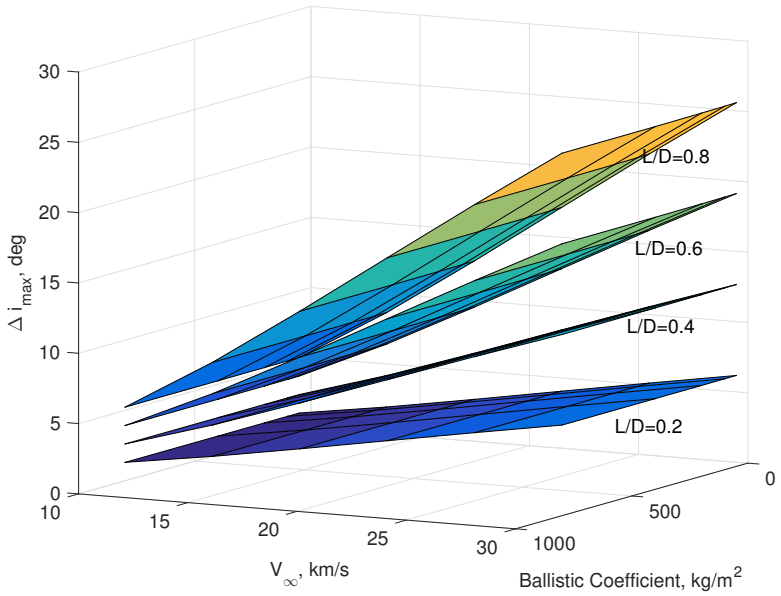

(a) 3D view

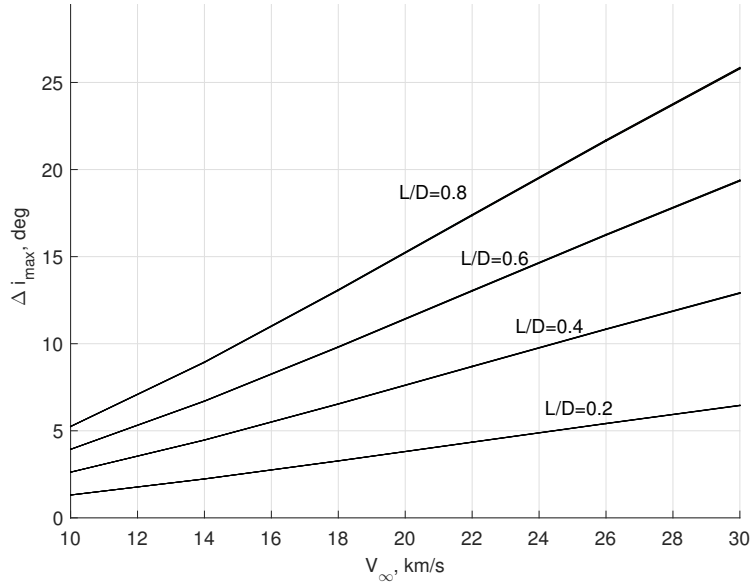

(b) 2D view

Figure 3.29. Inclination changes over arrival V_∞ from 10 to 30 km/s, ballistic coefficients from 50 to 800 kg/m^2. The initial entry latitude and entry heading are 0 and 0 deg respectively.

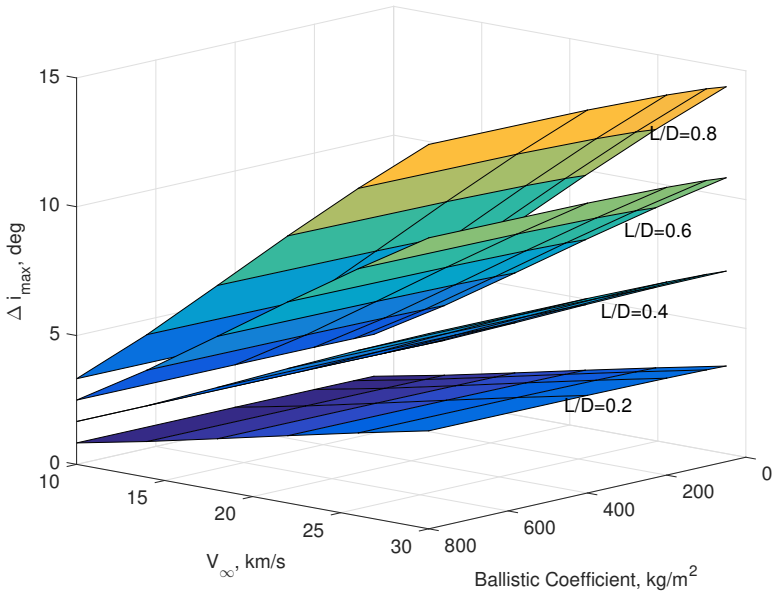

(a) 3D view

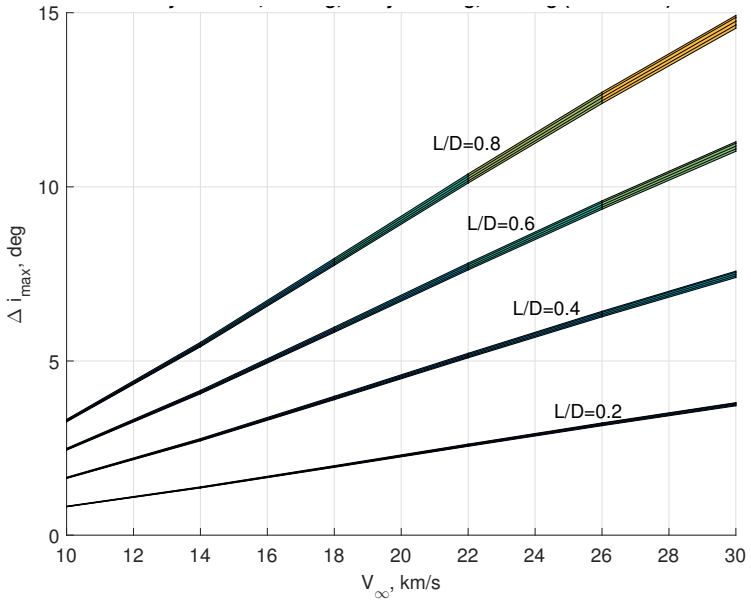

(b) 2D view

Figure 3.30. Inclination changes over arrival V_∞ from 10 to 30 km/s, ballistic coefficients from 50 to 800 kg/m^2. The initial entry latitude and entry heading are -74 deg and 270 deg respectively.

Figure 3.31 shows the maximum inclination changes at all possible entry latitude and entry headings. It may be desirable to avoid the combination of entry heading and entry latitude where the inclination changes are zero. The maximum inclination occurs at entry latitude of 0 deg and entry heading of 0 or 180 deg, the magnitude of the maximum inclination change is 15 deg. In Fig. 3.31, dark blue and bright yellow regions are where the highest maximum inclination changes occur. Note that the higher inclination changes occur near the equator. Thus to allow and ensure the most inclination changes, the vehicle needs to enter at a lower latitude. Figure 3.33 shows the inclination of final orbit at different entry conditions (i.e., latitude and heading) through an aerocapture maneuver by banking the vehicle to the left or right.

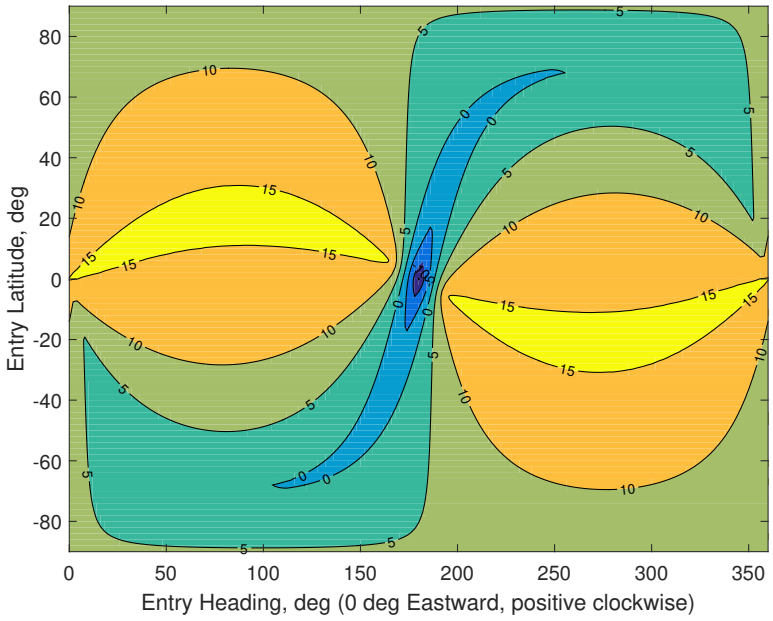

Figure 3.31. Maximum inclination increase at V_∞ = 20 km/s, β = 200 kg/m^2, and L/D=0.8 at all entry latitudes and entry headings.

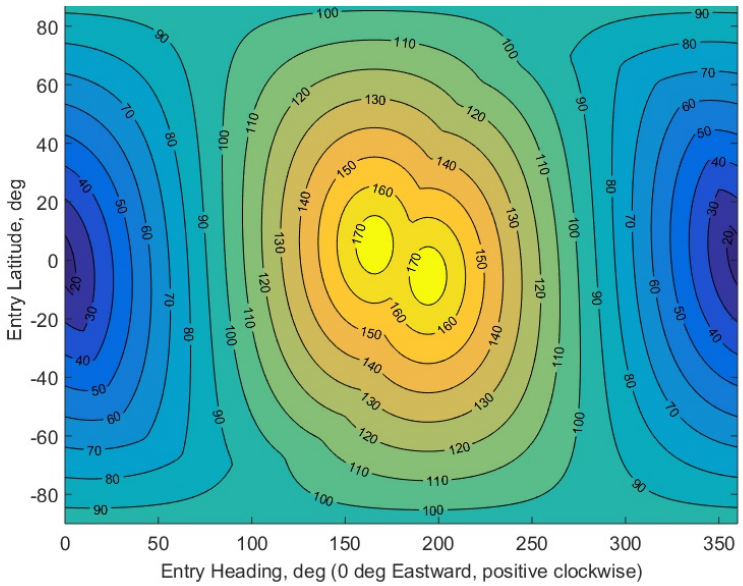

Figure 3.32. Maximum inclination achievable with $V_\infty = 20$ km/s, $\beta = 200$ kg/m^2, and L/D=0.8 at all entry latitudes and entry headings.

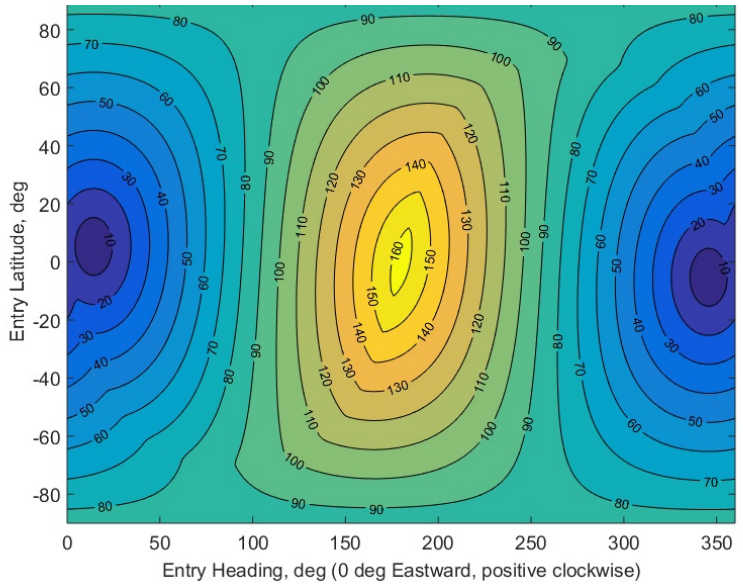

Figure 3.33. Minimum inclination achievable with $V_\infty = 20$ km/s, $\beta = 200$ kg/m^2, and L/D=0.8 at all entry latitudes and entry headings.

3.3.4 Shift in Line of Apsides

As illustrated in Fig. 3.34, lift-up and lift-down trajectories result in different angular distances traveled before exiting the atmosphere. The entry vehicle may change the line of apsides of the final orbit via an aerocapture maneuver. The line of apsides of the final orbit can be advanced or retreated by pointing the lift vector upward or downward. Figure 3.35 shows representative aerocapture trajectories at different values of L/D. For the purpose of presentation, a negative L/D denotes the case with lift vector pointing fully downward. For example, trajectories with L/D $= -0.8$ and L/D $= 0.8$ correspond to lift-down and lift-up cases respectively for a vehicle with L/D of 0.8). The nominal entry flight-path angles for different L/D are very close, and at the same entry velocity, the initial lines of apsides are roughly the same (within a range of 0.5 deg). The resultant true anomalies of the trajectories at the entry points are very close for different L/D configurations. In addition, the exit flight-path angles and velocities are also close for different L/D configurations, which means that the true anomalies at exit points are also very similar. Figure 3.35 has shown that with different L/D, the vehicle travels different angular distances in the atmosphere, resulting in the shift of the lines of apsides after the Aerocapture.

Figure 3.36 shows changes in line of apsides at different final orbit periods, and V_∞ from 10 to 30 km/s. As the final orbit period increases, the maximum $\Delta\omega$ achievable through an aerocapture maneuver does not change, whereas the higher the arrival V_∞, the more $\Delta\omega$ can be achieved. Note that lift-up and lift-down cases have opposing effects on $\Delta\omega$. Figure 3.37 shows the effect of ballistic coefficients and V_∞ on the changes in line of apsides. The capability of $\Delta\omega$ increases linearly with increasing V_∞ whereas $\Delta\omega$ is not affected by the ballistic coefficients. As shown for a ballistic case (i.e., L/D $= 0$), the changes in line of apsides are nearly zero for all values of ballistic coefficients and V_∞.

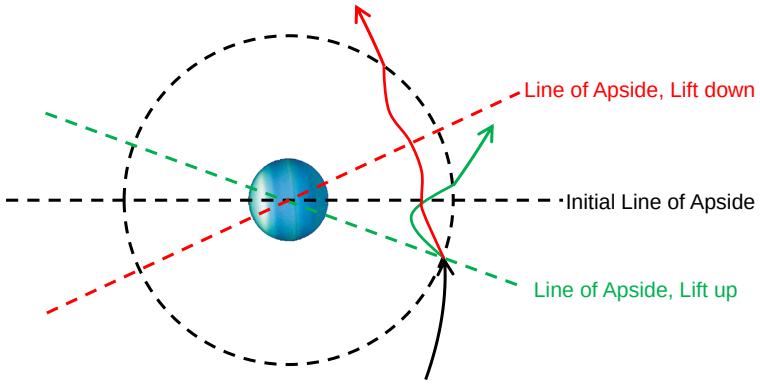

Figure 3.34. Illustration of shift of line of apsides for lift-up and lift-down cases.

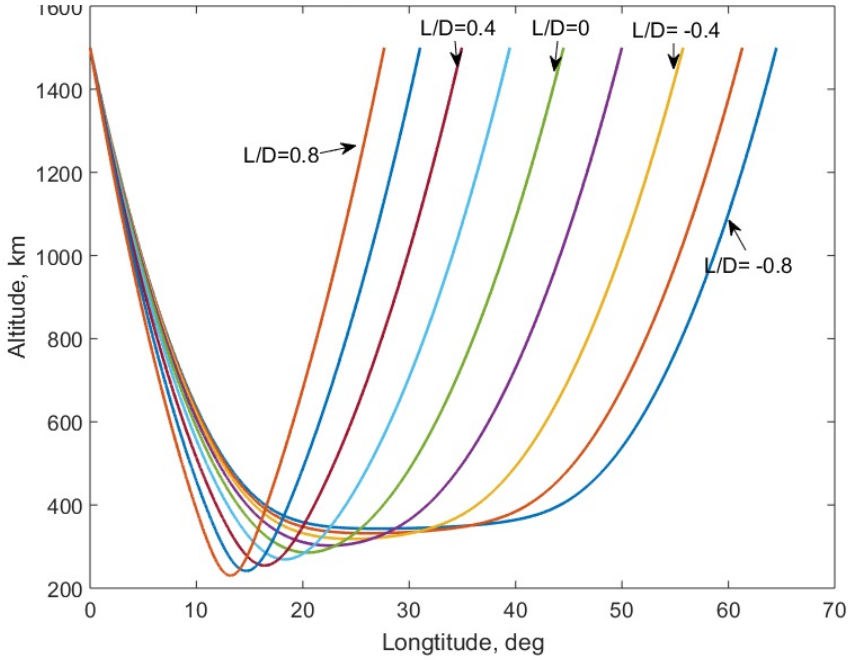

Figure 3.35. Aerocapture trajectory at different lift configurations. L/D = −0.8 represents the full lift-down case for L/D = 0.8.

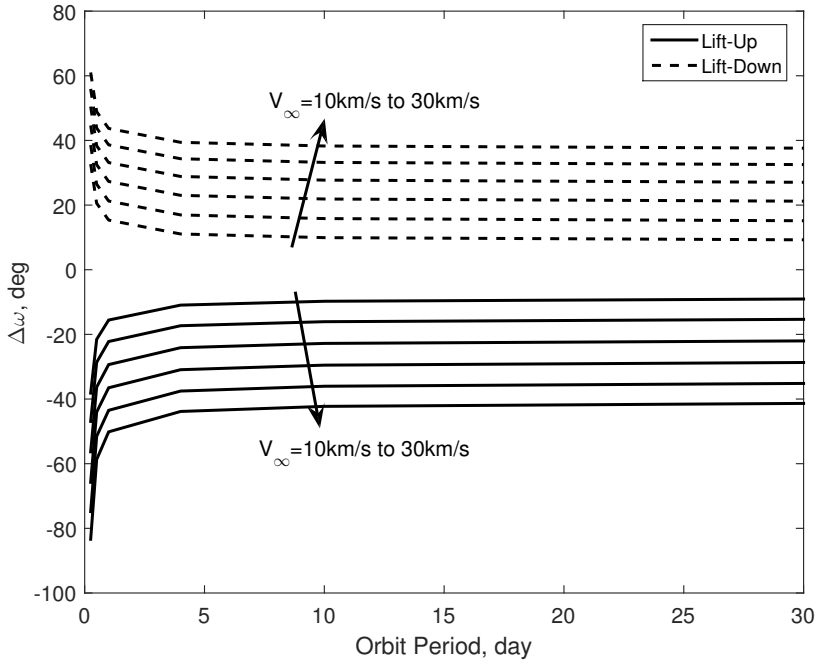

Figure 3.36. Shift of lines of apsides for both lift-up and lift-down configuration using a vehicle of L/D = 0.8 and $\beta = 200$ kg/m^2.

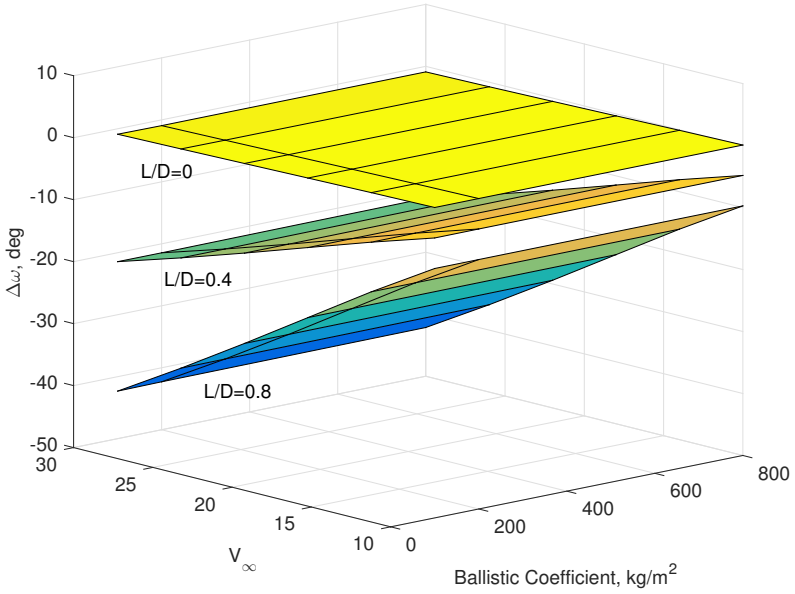

(a) 3D view

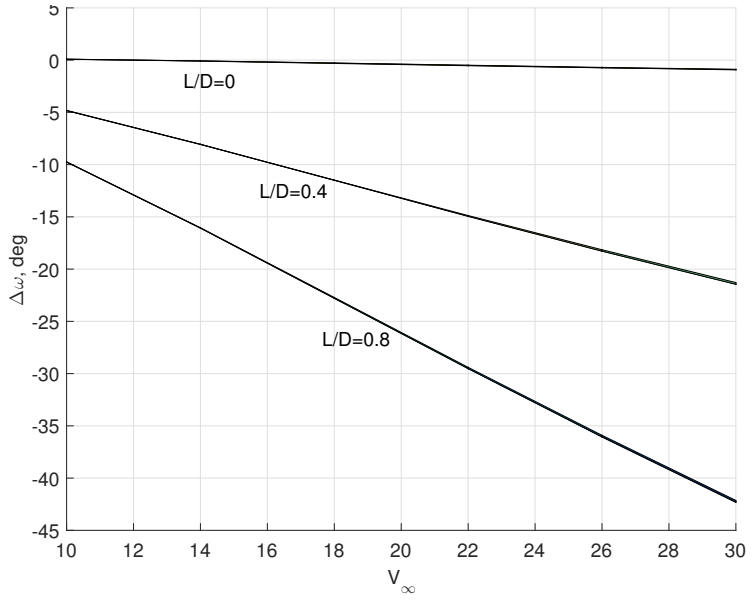

(b) 2D view

Figure 3.37. Effects of arrival V_∞, ballistic coefficients, and L/D on the changes in lines of apsides; assuming full lift up configuration.

4. DESIGN METHODOLOGY FOR SATURN SYSTEM MISSIONS USING AEROGRAVITY-ASSIST MANEUVERS

4.1 Background

The possibility of finding life on Ocean Worlds (i.e., Enceladus, Titan, and Europa) is of increasing interest to the science community, the public, and the politicians. Measurements from the Cassini mission have established the habitability of Enceladus oceans; a search-for-life mission is logically the next step, for example, an orbiter or a lander mission.

Previous Enceladus mission studies include Enceladus and Titan sample return mission concepts—Life Investigation For Enceladus (LIFE) [86] and Enceladus Life Signatures and Habitability (ELSAH); and Enceladus and Titan flyby mission concepts, Enceladus Life Finder (ELF) [87], Journey to Enceladus and Titan (JET) [88], and Explorer of Enceladus and Titan (E2T) [89]. It is worth noting that ELSAH is one of the missions selected for further study under NASA 2017 New Frontiers program to search for bio-signatures and assess Enceladus habitability.

Using Titan as an aerogravity-assist target for Saturn missions can be categorized as the endgame problem as appeared in the literature [90]. For interplanetary missions, the endgame problem deals with the final phase of the interplanetary trajectory which is entering in an orbit around the target body. The endgame problem for planetary moon orbiters has been challenging for the mission designers. Strange et al. [91] proposed graphical techniques for designing gravity-assist tours within a planet's system, followed by studies that focused on gravity-assist combined with V_∞ leveraging techniques for designing the endgame strategies [90, 92, 93].

4.1.1 Alternative Approaches

It is important to recognize the alternative methods for capturing at Saturn. Titan is an interesting target for performing gravity-assist in the Saturn system. The orbit can be reduced fairly quickly with several Titan flybys after the initial Saturn Orbit Insertion maneuver.

Direct Enceladus Insertion

Direct Enceladus insertion requires a very high ΔV. Even at the lowest possible Saturn arrival V_∞ of 0 km/s and lowest possible encounter velocity at Enceladus (i.e., the spacecraft approach velocity is along the direction of Enceladus orbit velocity), the ΔV for Enceladus Orbit Insertion (EOI) is 5.2 km/s, which is very high and requires a high mass fraction for the propulsion system, in particular the propellant mass.

Conventional Saturn Orbit Insertion

The traditional approach for a moon mission is to capture the spacecraft about the main body first then use a combination of trajectory correction maneuvers and then moon tours to pump down the orbit.

Cassini-Huygens mission can be used as a baseline for Saturn missions. Cassini's Saturn orbit insertion characteristics are as follows: the closest approach to Saturn is $r_p = 80{,}230$ km radius (19,980 km from cloud top); The main engine provided a total ΔV of 626 m/s for initial capture. The post SOI orbit had a velocity at periapsis, V_p of 30 km/s.

Moon Tours

A series of moon-tour maneuvers is implemented for Cassini to bring down its post-SOI orbit to the desired tour orbits. Campagnola and Russel investiaged the endgame problem using V_∞-leveraging technique [90] and multi-body technique [92]. To quickly quantify and analyze the cost and benefit of moon tours, Ref. [94] is used as a baseline to estimate the time and propellant requirement for reduced arrival

velocity at Enceladus—a total of 18 months with 1 year for the Rhea portion of the leveraging tour and 6 months for Dione portion.

4.1.2 Objectives

This chapter proposes a novel design methodology using Titan AGA maneuvers for a Saturn system mission, with a focus on Enceladus missions. The methodology is divided into three parts: (1) arrival at Saturn and Titan, which evaluates the arrival conditions at both Saturn and Titan; (2) atmospheric flight phase, which assess the performance of the vehicle in decelerating and changing orbits relative to Saturn; (3) post-AGA orbit, which characterizes the possible transfer orbit within the Saturn system for orbiter missions or direct Enceladus missions.

The rest of this chapter is structured as the following. Section 4.2 describes the methodology used for the analysis, including Saturn and Titan arrival, post-AGA transfer orbit, and vector diagram analysis. Section 4.2 also includes the equations of motion used for numerical simulation as well as relevant orbit equations. Section 4.3 discusses AGA turn angles with respect to outbound V_∞ and entry flight-path angle. Section 4.4 presents the AGA design space that combines the results obtained in Section 4.3 with details described in Section 4.2.

4.2 Methodology

4.2.1 Arriving at Saturn

While this chapter does not concern the search of interplanetary trajectories, this section discusses the possible arrival conditions at Saturn, for which a wide range of conditions is considered. Interplanetary trajectory design typically results in two parameters at target planet—arrival declination and arrival V_∞.

The graphical method as described in Ref. [40] is used to roughly estimate the arrival V_∞ at Saturn, without regard to the launch date and positions and alignments

of the planets. The results are also reproduced in Fig. 4.1. Assuming two metric tons payload mass, achievable launch characteristic energy (i.e., $C_3 = V_\infty^2$) are 140 km^2/s^2 for Space Launch System (Block I) and 80 km^2/s^2 for Delta-IV Heavy. Fig. 4.1 also notes a launch C_3 of 225 km^2/s^2, that is an equivalent V_∞ of 15 km/s. These launch C_3 values set limits on the arrival conditions that are useful to narrow down the possible arrival conditions for Titan encounter. For more detailed analysis of the possible gravity-assist paths to Saturn, Ref. [40] gives an example of Venus-Earth-Earth gravity-assist (VEEGA) sequence to Saturn.

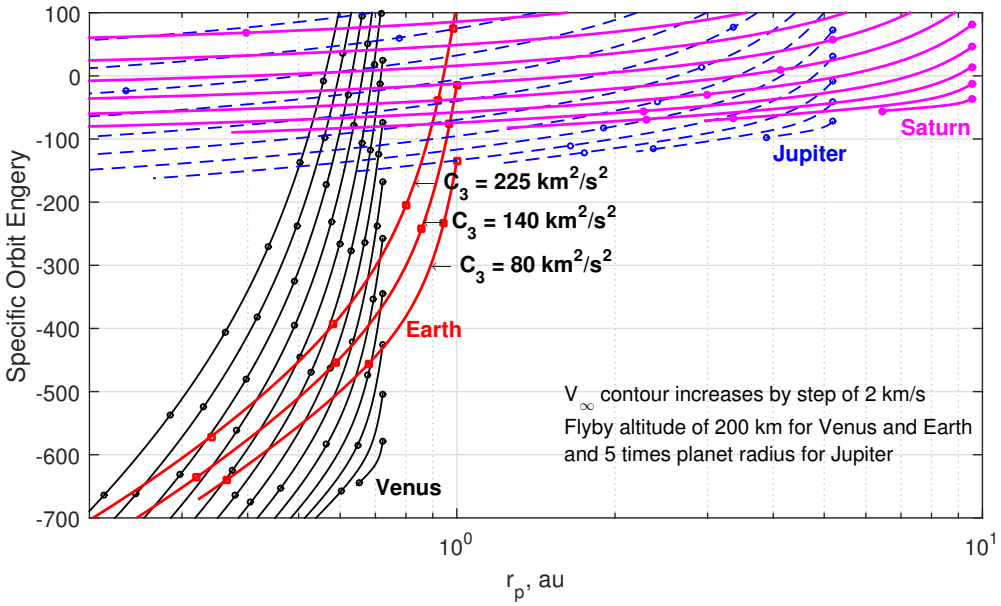

Figure 4.1. Tisserand graph for estimating arrival conditions at Saturn.

Note that in Fig. 4.1, V_∞ contours start at 1 km/s for each planet except Earth and are incremented by 2 km/s. The tick marks on the contour denote the limit on the flyby altitude, i.e., maximum GA turn angle achieved through a single pass at the lowest possible altitude (above the atmosphere or above the ring for Jupiter). Using VEEGA sequence and C_3 of 140 km^2/s^2, the range of arrival V_∞ at Saturn is roughly 7–15 km/s. If adding a Jupiter gravity-assist denoted as VEEJGA sequence, it is possible to achieve a wider range of arrival velocities of as low as 3 km/s and as

high as 19 km/s. However, given the planets alignment, Jupiter is not likely to be available for gravity-assist for Saturn missions in the next ten years.

4.2.2 Titan Encounter

Titan has a near-circular orbit about Saturn with a nearly zero inclination relative to Saturn's equatorial plane. Titan also has a zero deg axis tilt relative to Saturn's equatorial plane; however, Saturn has an axis tilt of 26.73 deg relative to the ecliptic plane. At different arrival declinations at Saturn, the spacecraft encounters Titan at different locations in its orbit. Ref. [91] proposed a graphical method for designing gravity-assist trajectories in which they use pump and crank angles to characterize the inbound and outbound orbit through a gravity-assist maneuver. Strange et al. combined a range of pump and crank angles and a constant V_∞ to form a sphere named V_∞ globe which is used for satellite tour design.

By properly selecting the B-plane target at Titan arrival, one can change both the velocity component in the ecliptic plane and velocity component normal to Saturn's equatorial plane. For a simplified analysis, the following chapter assumes a zero arrival declination at Titan.

When using Titan AGA, the phasing of Titan when the spacecraft arrives at Saturn must be considered as the phasing affects the arrival V_∞ at Titan. If the spacecraft encounters Titan while traveling in the same direction as Titan orbital velocity, the arrival V_∞ is lowest; while at the opposite direction, the arrival V_∞ is the highest.

Figure 4.2 shows the vector diagram for AGA maneuver. The arrival V_∞ at Saturn determines the magnitude of inbound velocity relative to Titan, V_{IN}, while the encounter of spacecraft with Titan in its orbit determines the inbound V_∞ at Titan, $V_{\infty,\mathrm{IN}}$.

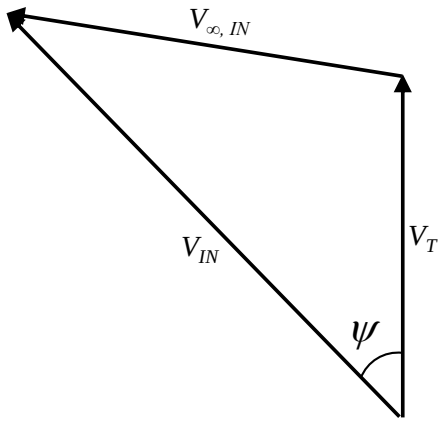

Figure 4.2. Vector diagram shows Titan's orbital velocity V_{T}, V_{IN}, $V_{\infty,\,\mathrm{IN}}$, and encounter angle, ψ.

In order to find the arrival V_∞ at Titan and Enceladus, the sphere-of-influence can be calculated for Titan and Enceladus respectively using the following [95, p.g. 416]:

$$r_{\mathrm{SOI}} = R\left(\frac{m_{\mathrm{moon}}}{m_{\mathrm{planet}}}\right)^{\frac{2}{5}} \tag{4.1}$$

where R denotes the mean distance from Saturn to the moons and m_{moon} and m_{planet} are the mass of the moons and planet respectively. The radius of sphere-of-influence for Titan and Enceladus are 4.33×10^4 km and 488 km. Since the radius of sphere-of-influence is very small compared to the orbit distance, zero-sphere-of-influence patched-conic approximation is assumed. Patched-conic assumption is common for low to medium fidelity trajectory search tools, such as STOUR [42].

Using the estimated Saturn arrival V_∞ from the last section, i.e., 7–15 km/s, a range of potential arrival V_∞ at Titan is marked in Fig. 4.3. The lowest possible arrival V_∞ at Titan is 5 km/s when the Saturn arrival V_∞ is 7 km/s and a zero Titan encounter angle; while the highest possible arrival V_∞ at Titan is 22.5 km/s, which corresponds to a Saturn arrival V_∞ of 15 km/s and a 180 deg encounter angle. While a lower Titan arrival V_∞ may be preferred to reduce the entry velocity (for AGA

maneuver), the discussion in Sec. 4.3 shows otherwise, that it is infeasible to achieve the lower Titan arrival V_∞ due to the limit on the AGA turn angle.

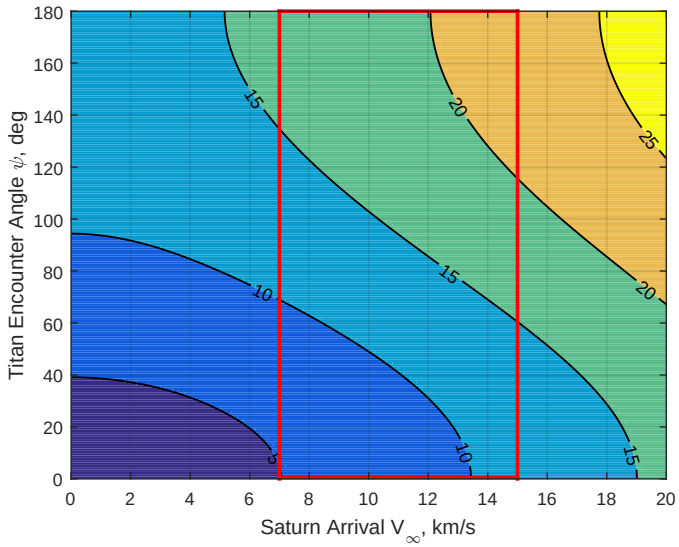

Figure 4.3. Contours of $V_{\infty,\,\mathrm{IN}}$ at Titan at different Saturn arrival V_∞ and Titan encounter angles.

4.2.3 Post-AGA Transfer Orbit

There are several mission scenarios to consider using Titan aerogravity-assist for capturing in the Saturn system. The mission can be a Saturn orbiter with multiple flybys of Enceladus and Titan, similar to the Cassini mission. The mission can also be an Enceladus orbiter or lander that uses Titan to decelerate and capture around Saturn and target Enceladus. Depending on the mission requirement, the spacecraft may target different transfer orbits following the Titan AGA maneuver. The subsequent sections consider two main scenarios: (1) direct missions to Enceladus; (2) Cassini-type Saturn missions.

For a Saturn mission, the spacecraft only has to deplete enough energy through AGA maneuver to get in a desired capture orbit around Saturn. However, for an Enceladus mission, the options for post-AGA orbits are more restrictive. The discus-

sion focuses on the case for an Enceladus mission and then extend to a more generic Saturn mission.

For a direct Enceladus mission, the Saturn-relative outbound orbit after Titan AGA should cross Enceladus orbit. As discussed for alternative approaches, moon tours for orbit pump down may be needed to further decrease the arrival velocity at Enceladus for either a lander or a sample return mission. The magnitude of ΔV_{E} required at Enceladus orbit insertion follows:

$$V_{\mathrm{E,\,IN}}^2 = V_{\mathrm{OUT}}^2 + \frac{2\mu_{\mathrm{S}}}{R_{\mathrm{E}}} - \frac{2\mu_{\mathrm{S}}}{R_{\mathrm{T}}} \tag{4.2a}$$

$$\gamma_{\mathrm{E,\,IN}} = \cos^{-1}\left(\frac{R_{\mathrm{T}} V_{\mathrm{OUT}} \cos\left(\gamma_{\mathrm{OUT}}\right)}{V_{\mathrm{E,\,IN}} R_{\mathrm{T}}}\right) \tag{4.2b}$$

$$\Delta V_{\mathrm{E}} = \sqrt{V_{\mathrm{E}}^2 + V_{\mathrm{E,\,IN}}^2 - 2V_{\mathrm{E}} V_{\mathrm{E,\,IN}} \cos(\gamma_{\mathrm{OUT}})} \tag{4.2c}$$

where V_{E} is the mean orbital velocity of Enceladus, V_{OUT} and γ_{OUT} are the Saturn-relative velocity and orbital flight-path angle of the Spacecraft outbound orbit at the mean radius of Titan orbit after AGA maneuver, and $V_{\mathrm{E,\,IN}}$ and $\gamma_{\mathrm{E,\,IN}}$ are the Saturn-relative velocity and orbital flight-path angle for Enceladus inbound orbit at the mean raidus of Enceladus orbit.

To achieve the minimum ΔV for Enceladus arrival, the transfer orbit should intercept Enceladus' orbit tangentially, meaning a zero orbital flight-path angle when the vehicle arrives at Enceladus. Such orbit also corresponds to the minimum energy orbit for Enceladus transfer and has the highest post-AGA velocity (i.e., V_{OUT}) at a certain orbital flight-path angle.

Direct Hohmann transfer from Titan to Enceladus is the minimal energy transfer for Enceladus arrival if no moon tours are used. However, the problem is, given the difference in their orbits, the ΔV for achieving Enceladus orbit is at least 3.7 km/s, which is considered very high for a practical mission. A main engine with an I_{sp} of 350s would require a propellant mass of more than 80% of the total mass. A velocity of 3.7 km/s, however, could be low enough for Enceladus sample collections [87].

Figure 4.4 shows the contours of Enceladus arrival V_∞ if the spacecraft uses a direct Enceladus transfer after Titan AGA. The contours show a maximum Enceladus arrival V_∞ of 4.5 km/s. The same trajectories can also be used for moon tours.

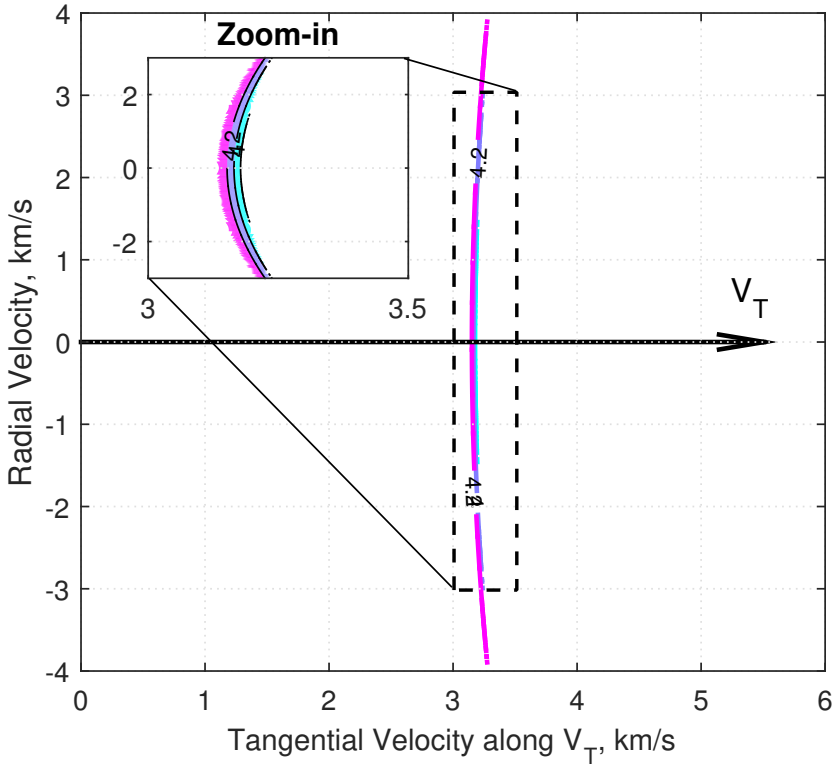

Figure 4.4. Post-AGA velocity characteristics for direct transfer to Enceladus.

4.2.4 Vector Diagram Analysis

Vector diagram is very useful in analyzing gravity-assist and is also a key element in the aerogravity-assist analysis because the velocities involved are relative to two central bodies.

Figure 4.5 shows a complete vector diagram using Titan aerogravity-assist, which is useful in describing the spacecraft velocities relative to Saturn and Titan. Velocity vectors represented are inbound and outbound hyperbolic excess velocities relative

to Titan, $V_{\infty,\,\mathrm{IN}}$ and $V_{\infty,\,\mathrm{OUT}}$ and inbound and outbound Saturn-relative velocities, V_{IN} and V_{OUT}. For a pure gravity-assist maneuver, $V_{\infty,\,\mathrm{IN}}$ and $V_{\infty,\,\mathrm{OUT}}$ have the same magnitude; however, for AGA maneuver the magnitude of $V_{\infty,\,\mathrm{OUT}}$ is smaller than that of $V_{\infty,\,\mathrm{IN}}$ due to the drag loss during atmospheric pass in Titan.

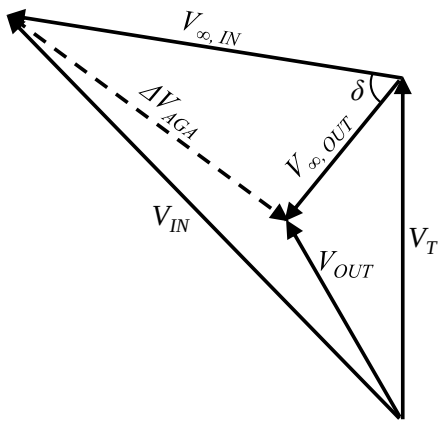

Figure 4.5. Illustrative vector diagram showing different velocities relative to Saturn and Titan before and after aerogravity-assist maneuver.

Vector diagram analysis follows a "backward-in-time" derivation, starting by choosing the post-AGA orbits with the desired spacecraft outbound velocity and orbital flight-path angles, then followed by the target outbound V_∞. For an Enceladus mission, the post-AGA orbit would cross the Enceladus' orbit which requires that the V_{OUT} has a magnitude smaller than Titan's orbital speed. The shaded area in Fig. 4.6 loosely resembles the shape of the colored contours in Fig. 4.4 and is used for illustration. A small trajectory correction maneuvers can be performed to adjust the post-AGA orbit to achieve the desired transfer orbits, therefore the shaded area can be slightly larger than the colored area in Fig. 4.4. Figure 4.6 shows the family of feasible V_{OUT} as solid arrows and the shaded area. The derived family of the target $V_{\infty,\,\mathrm{OUT}}$ which coincides with the shaded area. Any V_{OUT} vectors that end in the

shaded area are considered feasible trajectories that the spacecraft can use to transfer to Enceladus.

Another constraint not directly shown in the vector diagrams is that the post-AGA orbit should not coincide with the ring plane for safety concerns (i.e., the spacecraft must be in an orbit with r_p higher than the outer-most ring).

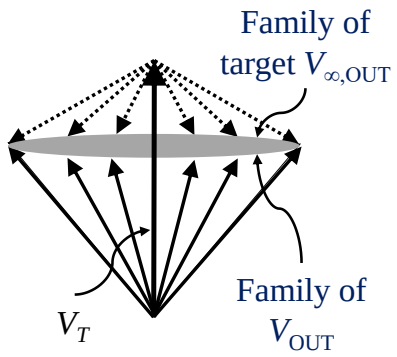

Figure 4.6. Representative V_{OUT} (solid arrows) and $V_{\infty,\,\mathrm{OUT}}$ (dash arrows) in Titan's orbital plane. Shaded region denotes families of both $V_{\infty,\,\mathrm{OUT}}$ and V_{OUT}.

As a result of ΔV due to atmospheric drag, the assumption of $V_{\infty,\,\mathrm{IN}} > V_{\infty,\,\mathrm{OUT}}$ is used to complete the vector diagram as in Fig. 4.5. Then the maximum aerodynamic turn angle would constraint the inbound $V_{\infty,\mathrm{IN}}$ space. The shaded area is an illustration and it is bounded only by the two solid lines which are constrained by the maximum AGA turn angle. There are no bounds for the shaded area in Fig. 4.7 on the left, right, and bottom, so feasible $V_{\infty,\,\mathrm{IN}}$ space extends further to the left, right, and bottom of the shaded area.

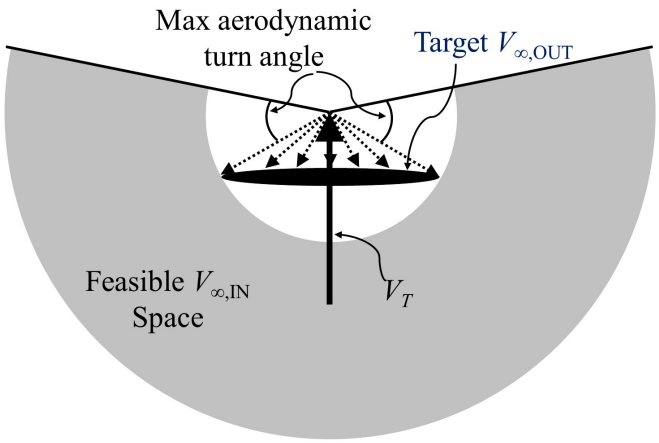

Figure 4.7. V_{OUT} (dash arrows) and $V_{\infty,\,\mathrm{OUT}}$ (shaded areas) in Titan's orbital plane.

As the spacecraft approaches Saturn at the lowest possible arrival velocity (i.e., Saturn $V_\infty = 0$ km/s), the inbound velocity at Titan V_{IN} is 7.9 km/s, meaning that the inbound velocity has to be higher than 7.9 km/s. Such limit adds a white circular area as shown in Fig. 4.8 which results in the feasible space of V_{IN} as the shaded area. V_{IN} originates from the tail of V_{T} and spans in the shaded regions and the red vector is shown in Fig. 4.8 as a sample V_{IN}. As mentioned for Fig. 4.7, similarly, the shaded area (i.e., feasible V_{IN} space) is only bounded on top and the area extends further to the left, right, and bottom.

The key result from the vector diagram analysis is that the shaded area in Fig. 4.8 informs that in order to use Titan as an aerogravity-assist target for Enceladus mission, the spacecraft must encounter Titan at a high orbital flight-path angle. The orbital flight-path angle (i.e., ψ in Fig. 4.8) is the angle between V_{IN} and V_{T}.

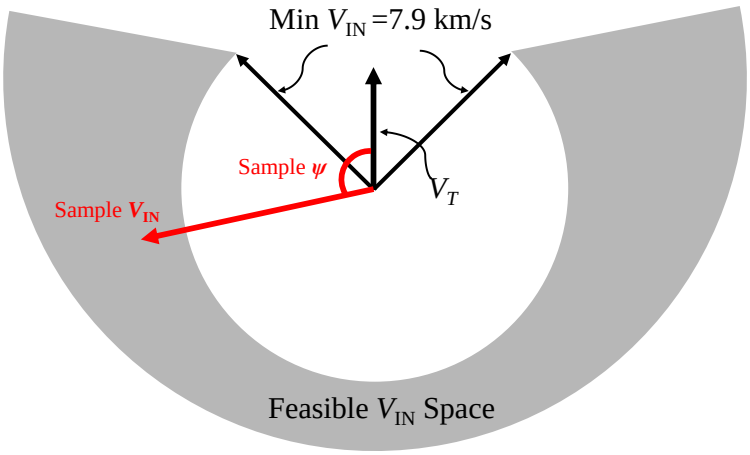

Figure 4.8. Feasible V_{IN} space derived from the constraints of Titan arrival conditions.

Gravity-assist maneuver allows both orbit pumping and cranking [91]. Pumping angle is equivalent to the turn angle defined in this section for a planar case, but cranking angle is the turn angle achieved in the out-of-plane component. Aerogravity-assist maneuver can also achieve both orbit pumping and cranking by properly choosing the B-plane target. Therefore, in Fig. 4.7, the lines constrained by the maximum AGA turn angle form a cone with its tip coinciding with the head of V_T.

It is worth noting that the vector diagram analysis in this section involves only the planar case where the spacecraft, Titan, and Enceladus all have coplanar orbits around Saturn. The analysis can be extended to include the out-of-plane components, but for the simplicity of illustrating the vector diagram analysis, only the planar case is shown. For 3D cases, the shaded elliptical region in Fig. 4.6 can be represented as an ellipsoid. Correspondingly, in Fig. 4.7 the white circular region would be a sphere, and in Fig. 4.8, the circular white area can be represented by another sphere.

Figure 4.9 is a variant plot of Fig. 4.3 and it shows the contours of potential arrival velocities relative to Titan orbital velocity V_T. The contours represent the head of the $V_{\infty,\,\mathrm{IN}}$. The grey area within the contours represents Saturn arrival V_∞ of less than 7 km/s, resulting from the estimates using the Tisserand graph. The white space outside of the contour represents Saturn arrival V_∞ of greater than 15 km/s. It is

important to note that all $V_{\infty,\,\mathrm{IN}}$ and $V_{\infty,\,\mathrm{OUT}}$ vectors originate from the head of V_{T}. A notional maximum AGA turn angle is used in Fig. 4.7 and there are similar regions that are inaccessible in Fig. 4.9 due to the turn angle constraints. Numerical analysis as described in the following sections is used to find such constraints.

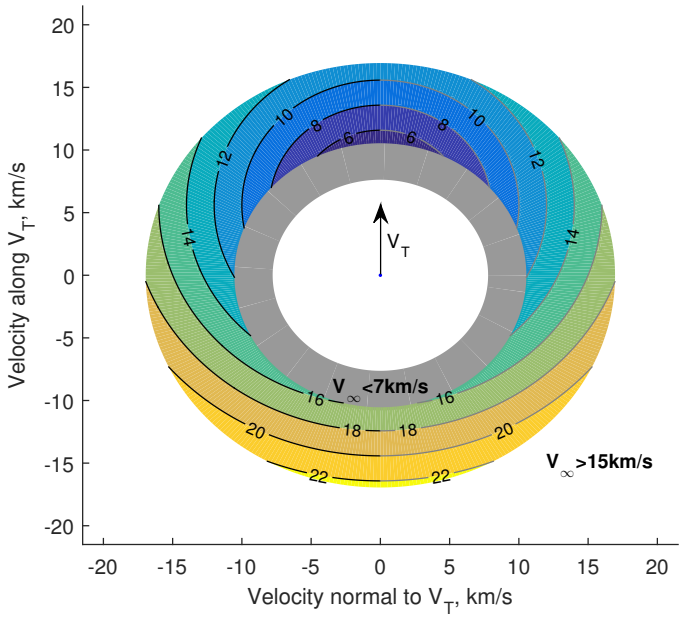

Figure 4.9. Contours of Titan inbound V_∞ (i.e., $V_{\infty,\,\mathrm{IN}}$) on Titan orbital plane and relative to Titan's orbital velocity. The gray area is for Saturn arrival V_∞ less than 7 km/s, the white space outside the colored region is for Saturn arrival V_∞ or more than 15 km/s

4.2.5 Equations of Motion

For numerical analysis of the aerogravity-assist trajectory, the vehicle uses dynamics models of atmosphere flight for the atmospheric phase of the trajectory (i.e., below the atmosphere interface altitude of 1000 km) and follows Keplerian orbit when outside of the atmosphere. The atmospheric portion of the flight assumes a non-rotating planet with non-rotating atmosphere same as Eqs. 2.1 and 2.2. Using planar equa-

tions of motion to simplify the analysis (i.e., aligning the coordinate system with the incoming trajectory thus ignoring the effect of latitude and heading), the simplified equations of motion is as follows:

$$\dot{\theta} = \frac{V \cos\gamma}{r} \tag{4.3a}$$

$$\dot{r} = V \sin\gamma \tag{4.3b}$$

$$\dot{V} = -\frac{q}{\beta} - g \sin\gamma \tag{4.3c}$$

$$\dot{\gamma} = -\frac{q(L/D)}{V\beta} \cos\sigma + \left(\frac{V}{r} - \frac{g}{V}\right) \cos\gamma \tag{4.3d}$$

To reduce the number of parameters and capture the fundamental characteristics of the entry vehicle, L/D and β are used similar for the aerocapture analysis in Chapter 4.2 and 3. Gravity acceleration follows the simplified model as $g = \mu/r^2$. In Eq. (4.3), θ does not appear in the other three equations, thus is an independent variable but it is required to calculate the turn angles of the inbound and outbound trajectory, therefore is retained in the equation of motion.

The non-atmospheric portion of the trajectory is solved using the analytical relations of conic sections for Keplerian orbits. Depending on the reference frame, the orbits can be either elliptic or hyperbolic. For example, the arrival trajectory at Saturn and at Titan would both be hyperbolic for interplanetary missions. The outbound orbit after the atmospheric phase is hyperbolic relative to Titan but elliptic relative to Saturn.

4.2.6 Aerothermodynamic Heating

For all atmospheric passes, heating is an important constraint to consider. While some atmospheric maneuvers (i.e., aerobraking) do not result in significant heat; for aerogravity-assist, the hypersonic speed at low altitude requires the consideration of

heating during the design process. The equations for evaluating heating environment are described in Section 2.3.2.

4.3 AGA Turn Angle Analysis

The turn angle achieved through a pure gravity-assist is a function of the closest approach distance from Titan. The vector diagram shown in Fig. 4.5 also includes ΔV_{AGA}, which is the equivalent ΔV resulting from the atmospheric pass. ΔV_{AGA} is the resultant of ΔV from both the gravity turn and aerodynamic deceleration. However, it is more convenient to describe the maneuver using ΔV_{AGA} and AGA turn angle, δ_{AGA}. It is worth noting that the two quantities—AGA turn angle and aerodynamic deceleration—are interdependent of each other. Aerodynamic deceleration depends heavily on the characteristics of the trajectory during the atmospheric pass, which varies with atmospheric entry conditions, vehicle aerodynamic properties, and atmospheric conditions. While for gravity-assist, there exists algebraic equations relating the inbound and outbound trajectory based on the B-plane targeting; no such equation exists for AGA maneuvers. As such, the trajectory may be very sensitive to the entry flight-path angle and vehicle lift profiles, the vehicle requires guidance and control to properly guide the vehicle to a desired state. Gravity-assist, on the other hand, is a more passive maneuver where no additional control is needed while performing flyby of a body (Note there may exist exception such as powered gravity-assist).

The turn angle from pure gravity-assist is:

$$\delta_{\text{ga}} = 2\sin^{-1}\left[1/\left(1 + r_p V_\infty^2/\mu\right)\right] \tag{4.4}$$

The turn angle achievable via a pure gravity-assist is shown in Fig. 4.10. A higher turn angle (i.e., effective ΔV) can be achieved by targeting a lower apoapsis altitude. However, the following results will show the turn angle from a AGA maneuver can be as much as 30 deg for V_∞ of more than 10 km/s, therefore, the slightly higher

turn angle at a lower altitude from gravity-assist is insignificant as compared to AGA maneuver.

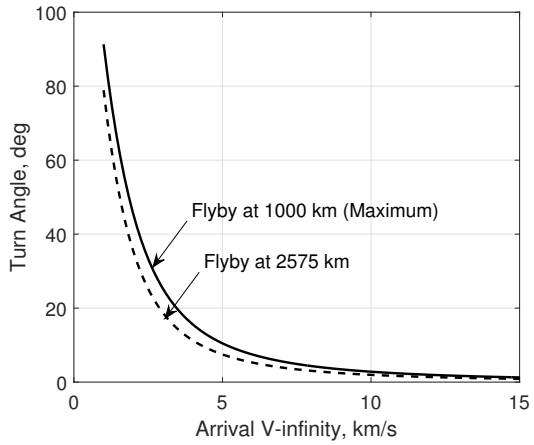

Figure 4.10. Turn angle from a pure gravity-assist at Titan.

The conversion between V_∞ at Saturn and spacecraft velocities at Titan V_{IN} is straightforward. The relevant orbit equations used to convert orbit parameters are listed as follows:

$$V_{\text{IN}} = \sqrt{V_{\infty,\text{S}}^2 + 2\mu_\text{S}/R_\text{T}} \tag{4.5}$$

Specific angular momentum, h, and velocity at apoapsis and periapsis points, specific orbit energy, ϵ, eccentricity, e, semi-latus rectum, p, radius at periapsis, r_p, and apoapsis, r_a, are as follows:

$$h = rV\cos\gamma = r_a V_a = r_p V_p \tag{4.6a}$$

$$\epsilon = V^2/2 - \mu/r \tag{4.6b}$$

$$e = \sqrt{1 + 2\epsilon h^2/\mu^2} \tag{4.6c}$$

$$p = h^2/\mu \tag{4.6d}$$

$$r_a = p/\left(1-e\right) \tag{4.6e}$$

$$r_p = p/\left(1+e\right) \tag{4.6f}$$

Other useful equations are:

$$h = R_E V_E \cos\gamma_E = R_T V_T \cos\gamma_T \tag{4.7a}$$

$$\epsilon = V_E^2/2 - \mu_{\text{Saturn}}/R_E = V_T^2/2 - \mu_{\text{Saturn}}/R_T \tag{4.7b}$$

The relations of turn angles from entry and exit conditions are especially important. The inbound and outbound trajectories of an AGA maneuver are both hyperbolic orbits about Titan. The following relations are derived based on hyperbolic orbits. The characteristic of the post-AGA orbit can be described by the outbound V_∞ and AGA turn angle.

The turn angle achieved from an AGA maneuver for a planar case is found using

$$\delta_{\text{aga}} = |\theta_{\infty,\text{in}} - \theta_{\text{in}}| + |\theta_{\infty,\text{out}} - \theta_{\text{out}}| + \theta_{\text{aga}} \tag{4.8}$$

where $\theta_{\infty,\text{in}}$ and $\theta_{\infty,\text{out}}$ are the true anomalies of the inbound and outbound V_∞ velocity vectors respectively, θ_{in} and θ_{out} are the true anomalies at atmospheric entry and exit points respectively, and θ_{aga} is the angular distance traveled through an AGA maneuver. The true anomalies are found as the follows:

$$\theta_{\infty,\text{in}} = -\cos^{-1}\left(-1/e_{\text{in}}\right) \tag{4.9a}$$

$$\theta_{\infty,\text{out}} = \cos^{-1}\left(-1/e_{\text{out}}\right) \tag{4.9b}$$

$$\theta_{\text{in}} = -\cos^{-1}\left(p_{\text{in}}/\left(\mu_{\text{p}} e_{\text{in}}\right) - 1/e_{\text{in}}\right) \tag{4.9c}$$

$$\theta_{\text{out}} = \cos^{-1}\left(p_{\text{out}}/\left(\mu_{\text{p}} e_{\text{out}}\right) - 1/e_{\text{out}}\right) \tag{4.9d}$$

Figure 4.11 shows AGA turn angles with two vehicle L/D configurations (i.e., full lift-up and full lift-down) at different entry flight-path angles. With the full lift-down case, one can achieve a turn angle of more than 100 deg; however, the entry flight-path angle corresponding to such turn angle is almost the same as turn angle of 40 deg. Given the uncertainties in entry flight-path angle, vehicle aerodynamic properties, and atmospheric density; achieving a turn angle of 100 deg is simply implausible. With a higher arrival V_∞ the lift-down curve in Fig. 4.11 would shift slightly towards

the left, meaning a steeper entry flight-path angle. The following section shows that the higher turn angle is achieved with a longer atmospheric pass, thus more drag loss.

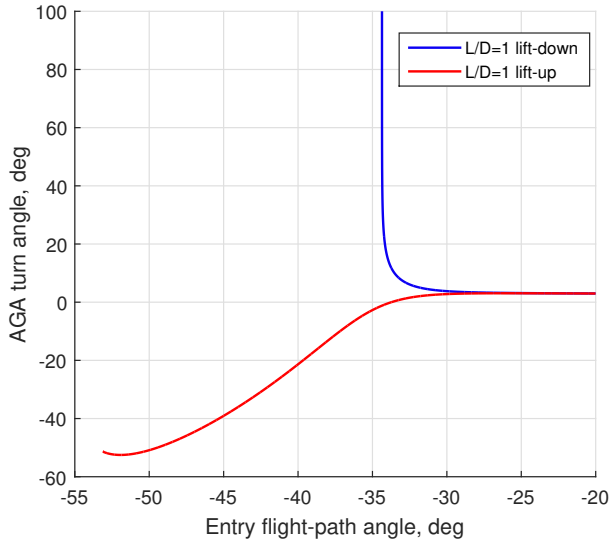

Figure 4.11. AGA turn angles for different entry flight-path angle conditions with full lift-up and lift-down configuration for L/D = 1, $\beta = 200$ kg/m^2, and $V_{\infty,\,\mathrm{IN}}$ of 10 km/s.

It is important to note that the two configurations considered—full lift-up and full lift-down—represent the limit of AGA maneuvers, which means, under the same arrival condition with the same type of vehicle (i.e., β of 200 kg/m^2 and L/D of 1.0), the spacecraft cannot achieve higher turn angles than the two curves in Fig. 4.11.

4.3.1 Turn Angle and Outbound V_∞

Obtaining the turn angle from AGA maneuver is not trivial and the values depend heavily on the trajectory during the atmospheric pass, as observed from Fig. 4.11. A ballistic entry trajectory may seem to be a good option as it requires no vehicle control. However, any slight variation in entry flight-path angle or aerodynamic properties would cause the vehicle to deviate from its planned path. In addition,

a ballistic trajectory can only reduce the magnitude of the V_∞ vector and cannot achieve any useful turn angle.

Figure 4.12 shows the space for outbound V_∞ in relation to the $V_{\infty,\,\mathrm{IN}}$. The solid lines show the possible heads for the outbound V_∞ for different vehicle L/D configurations with the tail originating from (0, 0). The top line represents L/D = 1 with full lift-down configuration while the bottom line L/D = 1 with full lift-up configuration. Each line is spaced by L/D difference of 0.2. The combination of the top and bottom most lines limits the $V_{\infty,\,\mathrm{OUT}}$ space. As shown and labeled in Fig. 4.12, outbound V_∞ have two components, one along the direction of $V_{\infty,\,\mathrm{IN}}$ and another normal to $V_{\infty,\,\mathrm{IN}}$. The dashed contours in Fig. 4.12 are the corresponding entry flight-path angles. As the shapes of the entry flight-path angle contours show, lift-up and lift-down would require targeting at very different entry flight-path angles.

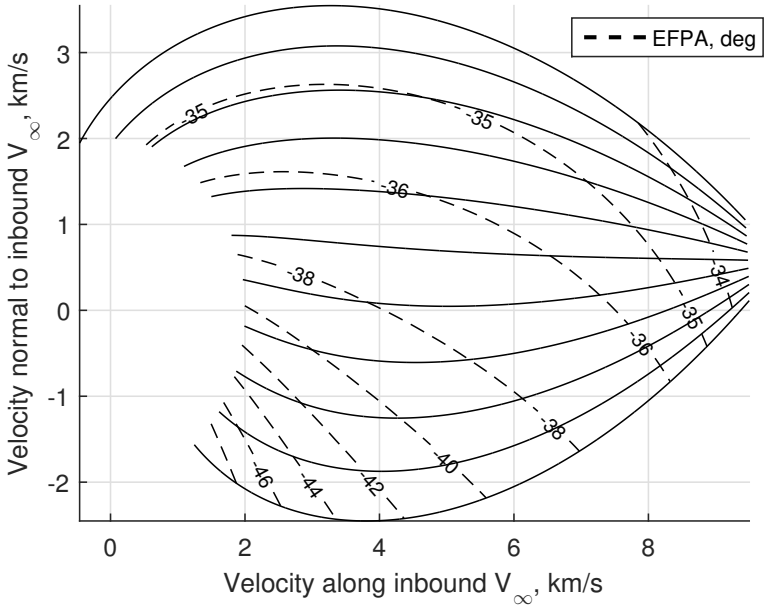

Figure 4.12. $V_{\infty,\,\mathrm{OUT}}$ space for $V_{\infty,\,\mathrm{IN}}$ of 10 km/s, with different vehicle L/D configurations.

It is worth noting that for the purpose of Titan AGA, the analysis eliminated the cases where $V_{\infty,\,\mathrm{OUT}}$ is lower than 2 km/s since for V_∞ of less than 2 km/s, the

trajectories do not encounter any moons within Titan's orbit. One could use another Titan flyby to perform an additional gravity-assist to reduce the orbit; however, such cases are similar to a generic Saturn mission.

On top of Fig. 4.12, peak g-load, peak heat rate, and total heat load are added to obtain Fig. 4.13. Peak g-load contours and peak heat rate contours follow similar patterns as the entry flight-path angle contours, which means that targeting a higher entry flight-path angle would result in a higher peak g-load and peak heat rate. Peak g-load varies from as low as 1 g from the left of the plot to up to 20 g approaching the lift-up trajectory at high entry flight-path angles; peak heat rate varies from as low as 75 W/cm^2 from the left of the plot to up to 315 W/cm^2 approaching the area for lift-up trajectory at very high entry flight-path angles.

Total heat load follows a different pattern as peak g-load and peak heat rate. Total heat load is maximum at 37 kJ/cm^2 when entering at shallow flight-path angle with fully lift-down configuration at L/D = 1 (top most solid line), and at the same time reaching the highest turn angle (i.e., noted by coordinate (0, 2) in Fig. 4.13). The main reason is that the vehicle flies in the atmosphere for a longer period at a similar heat rate condition, thus resulting in a higher total heat load. On the other hand, total heat load is about 15 kJ/cm^2 when flying at a full lift-up trajectory with L/D = 1 (bottom-most solid line), and at the steepest entry flight-path angle.

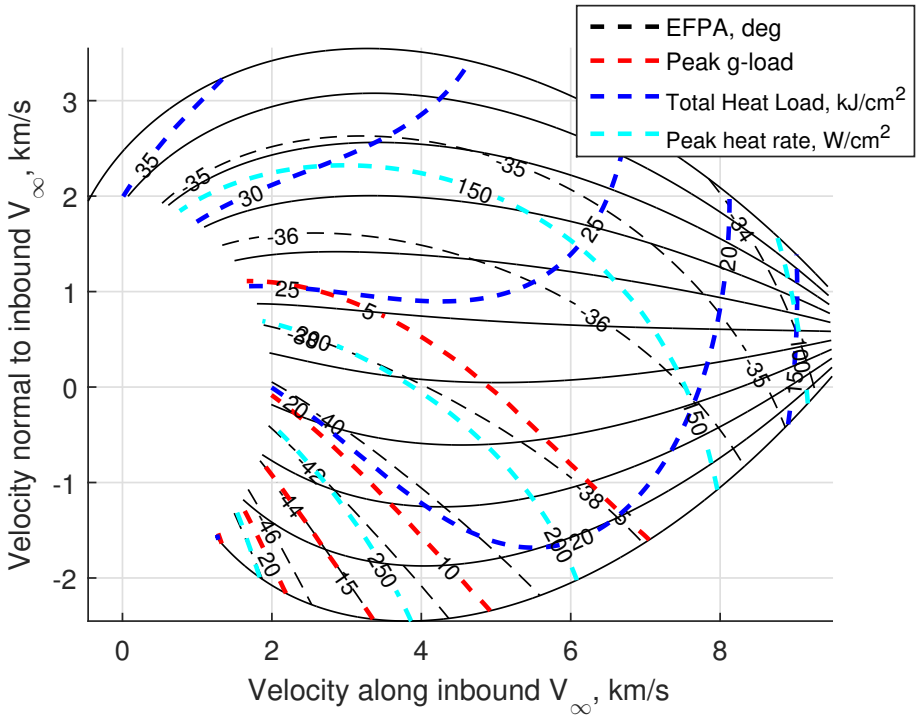

Figure 4.13. Outbound V_∞ space for $V_{\infty,in}$ of 10 km/s, with different vehicle L/D orientations, with design parameter included.

4.3.2 Turn Angle and Entry Flight-Path Angle

Figure 4.14 shows the contours of vehicle L/D configuration and $V_{\infty,\,\mathrm{OUT}}$ magnitude corresponding to different entry flight-path angle and AGA turn angles. Note that for L/D configurations, positive numbers represent the full lift-up case with the particular L/D value whereas negative numbers represent full lift-down cases. In addition, L/D actually denotes $(\mathrm{L/D})_{\max}$, not the commanded L/D.

Figure 4.14 essentially shows all possible target entry flight-path angle ranges and AGA turn angles for different vehicle configurations. For example, if choosing maximum vehicle L/D to be 0.2, the possible combination of entry flight-path angle and AGA turn angles are effectively constrained by the two contours labeled 0.2 and -0.2. Similarly, if choosing a vehicle with a designed L/D of 0.4, all possible combinations of entry flight-path angle and AGA turn angles are bounded by 0.4

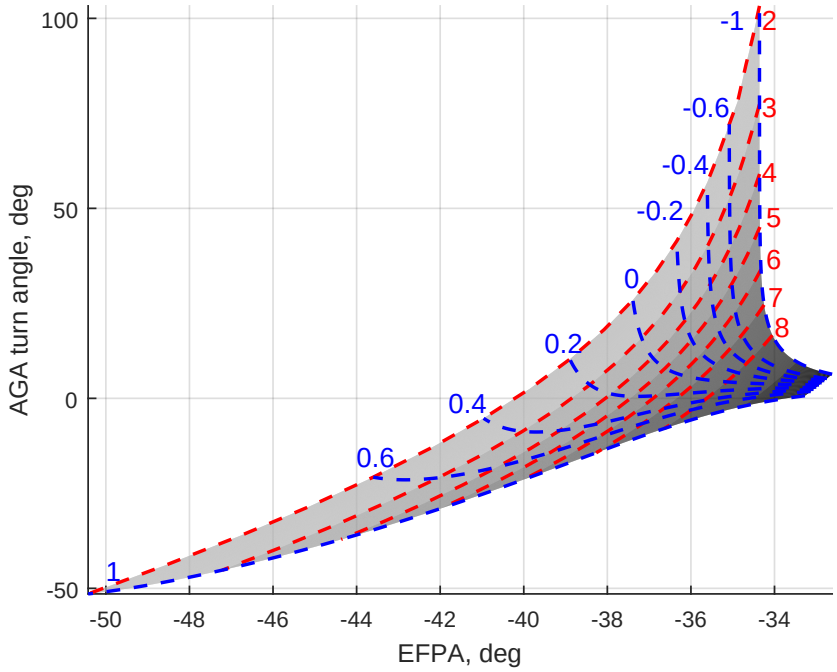

Figure 4.14. Vehicle L/D contours (blue) and $V_{\infty,\,\mathrm{OUT}}$ contours (red) at different entry flight-path angle and AGA turn angle at $V_{\infty,\,\mathrm{IN}} = 10$ km/s. Contour of L/D = 0 denotes the ballistic case.

and −0.4 contours. Note that from Fig. 4.4, the targeted $V_{\infty,\,\mathrm{OUT}}$ magnitude ranges from 2.4 km/s (with V_{OUT} along the direction of V_{T}) and up to 5 km/s (i.e., V_{OUT} is 45 deg relative to V_{T}). At a shallow entry flight-path angle, the vehicle won't have enough deceleration to meet the $V_{\infty,\,\mathrm{OUT}}$ target. If a vehicle with L/D of 0.2 enters the atmosphere with flight-path angle steeper than −42 deg, the vehicle would not leave Titan with enough V_∞ or would enter the atmosphere completely.

It is important to note that positive and negative turn angles are equivalent. Proper B-plane point can be selected to target the preferred turn angle. Upon closer examination of Fig. 4.14, a targeted entry flight-path angle of steeper than −41 deg would require that the vehicle has L/D more than 0.4. Similarly, any targeted entry flight-path angle shallower than −35.5 deg would also require that the vehicle has L/D of more than 0.4. The L/D value of 0.4 is from the configuration of the state-of-the-art entry vehicles that are in the low-L/D domain (e.g., Apollo command module of L/D $>$ 0.3 as in Table 2.2); whereas using vehicles with L/D of more than 0.4 would require significant investments in technology.

Consider the region enclosed by the contours of L/D of 0.4 and L/D of −0.4 as shown in Fig. 4.15, using lift-down configuration (i.e., the contour of 0.4), the vehicle can only achieve up to 10 deg turn angle which is not a large turn angle. However, the lift-down configurations result into a small range of entry flight-path angles at high turn angles. In order to accommodate uncertainties from different sources, it is not preferred to select a trajectory on the boundary of these contours. For a vehicle with L/D of 0.4, selecting the design point bounded by the lines of L/D of 0.2 and −0.2 would offer the maximum robustness for guidance and control to accommodate the uncertainties. Also, the designed turn angle should be achievable at a range of entry flight-path angles; for example, if a 30-deg turn angle is selected, the required entry flight-path angle range is from −35.5 to −37 deg. Depending on the navigation error, the 1.5-deg range of entry flight-path angle may or may not be enough. However, if 40 deg turn angle is selected, the corresponding range of entry flight-path angle is more restrictive (−35.6 to −36.5 deg).

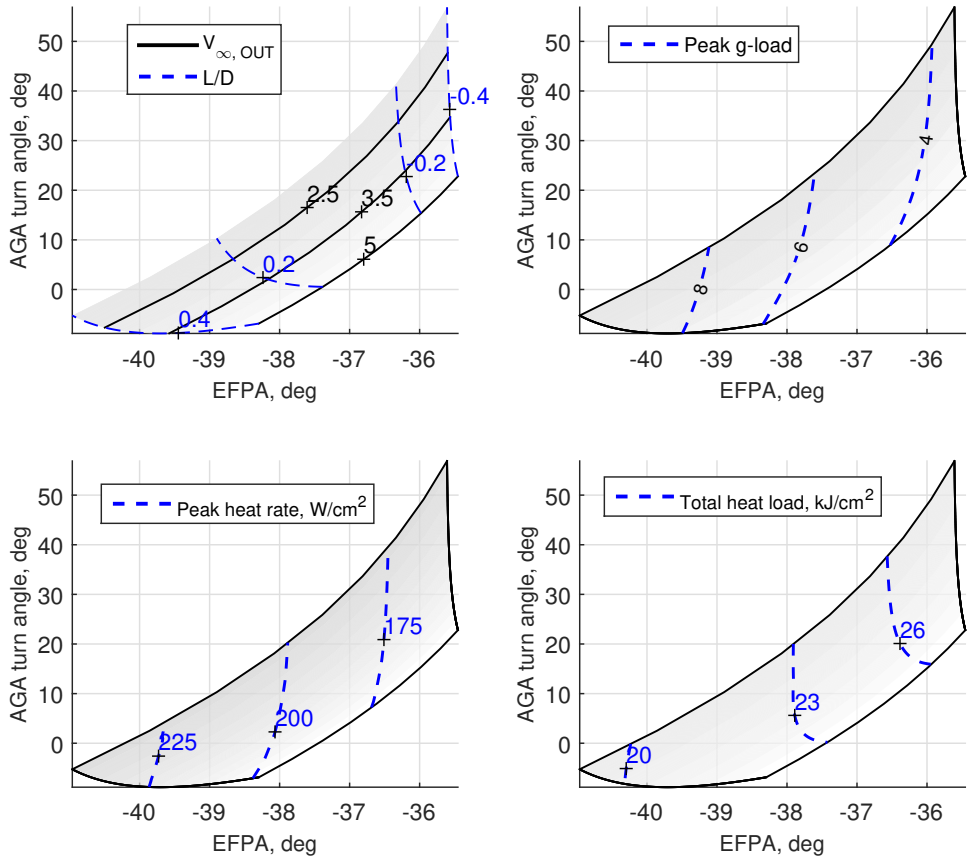

Figure 4.15. Contours of peak g-load, peak heat rate, and total heat load at $V_{\infty,\,\mathrm{IN}} =$ 10 km/s for maximum L/D of 0.4 and $V_{\infty,\,\mathrm{OUT}}$ of 2–5 km/s.

If the target entry flight-path angle is shallower than the smallest entry flight-path angle in Fig. 4.15, the outbound trajectory would not have the desired properties for an Enceladus-bound mission. Assuming an error from approach navigation in the initial entry flight-path angle is ±1 deg, the selected turn angle must be achievable with a 2-deg range in entry flight-path angles. In Fig. 4.15, −35.5 to −37.5 entry flight-path angle range results in approximately 25 deg turn angle.

4.4 Titan AGA Design Space

4.4.1 Enceladus Mission

Depending on the arrival geometry (as shown in Fig. 4.9), different Titan encounter angles result in different $V_{\infty,\,\mathrm{IN}}$ magnitude. As Fig. 4.15 shows the results for $V_{\infty,\,\mathrm{IN}}$ of 10 km/s, this section extends the results for $V_{\infty,\,\mathrm{IN}}$ from 12 to 20 km/s with an interval of 4 km/s.

Figures 4.16, 4.17, and 4.18 show the corresponding design plots for $V_{\infty,\,\mathrm{IN}}$ of 12 km/s, 16 km/s, and 20 km/s respectively. The general trends for peak g-load, peak heat rate, and total heat load for all $V_{\infty,\,\mathrm{IN}}$ magnitudes remain the same as $V_{\infty,\,\mathrm{IN}} = 10$ km/s. Increasing $V_{\infty,\,\mathrm{IN}}$ magnitude results in a higher peak g-load, higher peak heat rate, and higher total heat load. Conventionally, when designing an entry vehicle, the goal is to minimize the design parameters such as, peak g-load, peak heat rate, and total heat load, in order to reduce the structural requirement and increase the payload mass fraction, which is beneficial to either deliver more payload mass or use a smaller launch vehicle to save on launch cost. Thus, the smallest possible $V_{\infty,\,\mathrm{IN}}$ should be used during the design process.

By comparing the top left figures in Figs. 4.16, 4.17, and 4.18, the differences in the positive AGA turn angles are very small, and there is only a slight increase in the negative range from −10 to −20 deg. Since −20 deg is still a smaller angle than the positive turn angles, the difference between −10 and −20 is not important.

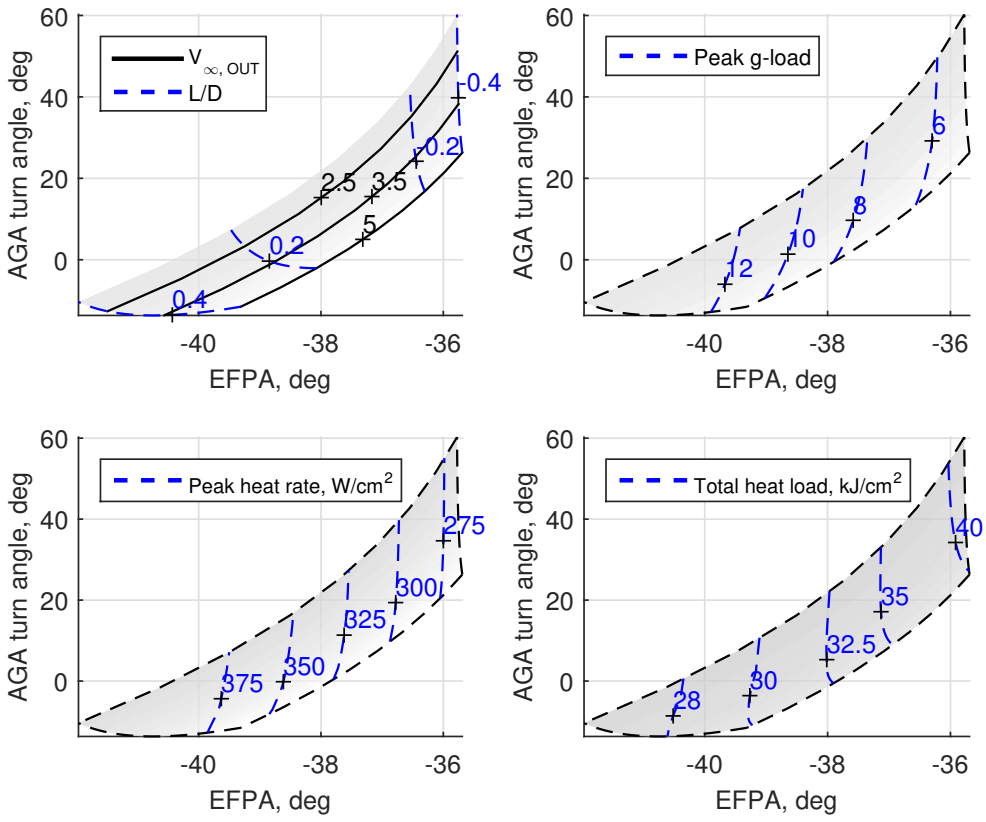

Figure 4.16. Contours of peak g-load, peak heat rate and total heat load at $V_{\infty,\,\mathrm{IN}} = 12$ km/s for maximum L/D of 0.4 and $V_{\infty,\,\mathrm{OUT}}$ of 2–5 km/s.

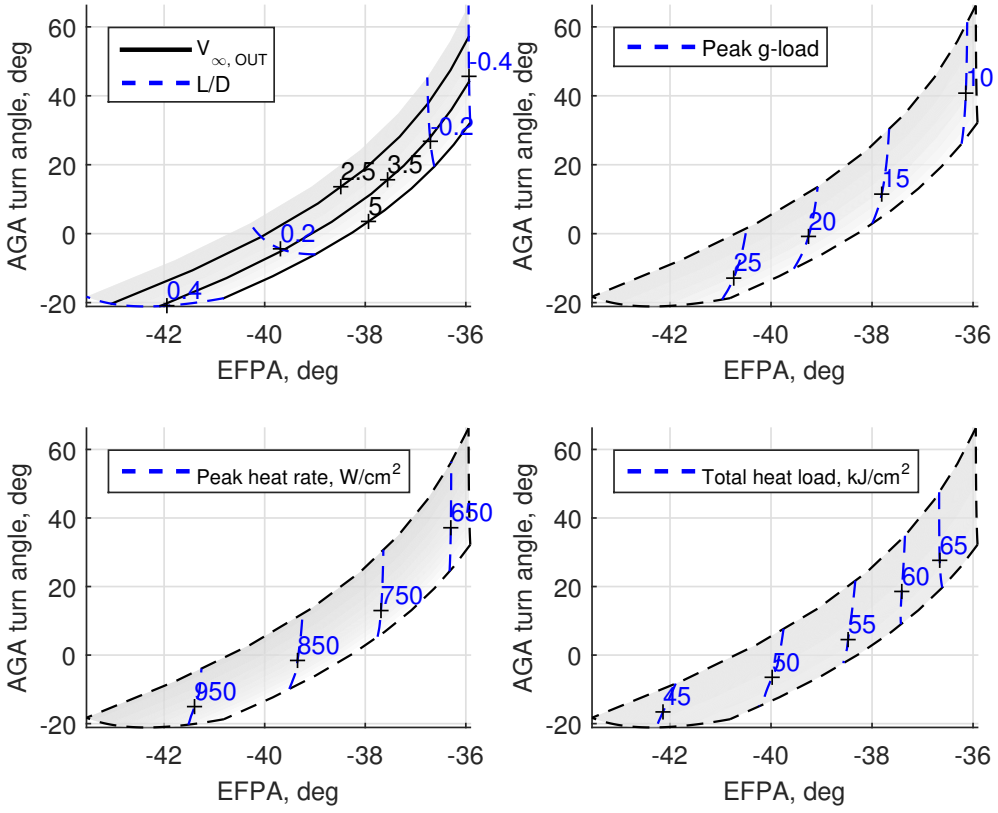

Figure 4.17. Contours of peak g-load, peak heat rate and total heat load at $V_{\infty,\,\mathrm{IN}} = 16$ km/s for maximum L/D of 0.4 and $V_{\infty,\,\mathrm{OUT}}$ of 2–5 km/s.

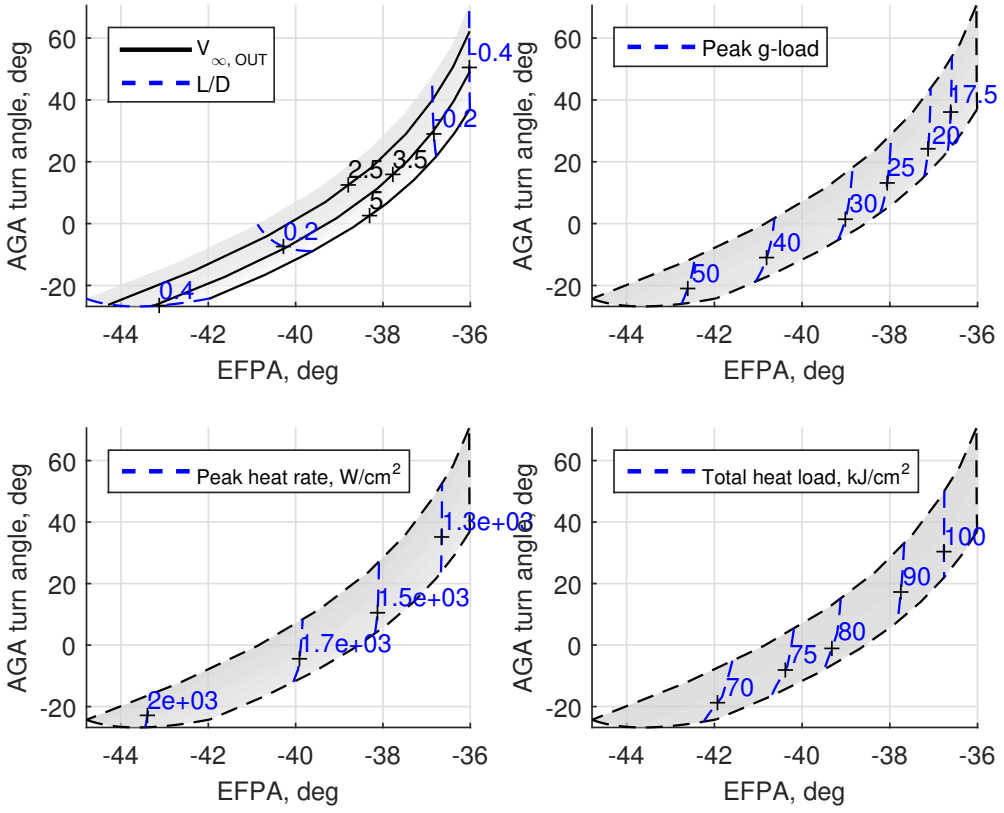

Figure 4.18. Contours of peak g-load, peak heat rate and total heat load at $V_{\infty,\,\mathrm{IN}} = 20$ km/s for maximum L/D of 0.4 and $V_{\infty,\,\mathrm{OUT}}$ of 2–5 km/s.

Assuming a 2-deg required range for entry flight-path angle, the potential AGA turn angles are roughly 25 deg for $V_{\infty,\,\mathrm{IN}}$ of 12, 16, and 20 km/s. Using the 25-deg turn angle as a baseline design parameter, the value for the maximum aerodynamic turn angle is substituted in Fig. 4.7 in the vector diagram analysis and also related to Fig. 4.9.

Figure 4.19 shows the case with $V_{\infty,\,\mathrm{IN}}$ of 10 km/s where the turn angle of 25 deg is barely enough to result in an $V_{\infty,\,\mathrm{OUT}}$ in the targeted range (black-shaded ellipse). As a reference, the maximum angle between V_{T} and $V_{\infty,\,\mathrm{IN}}$ = 10 km/s 101.5 deg; for V_{T} and $V_{\infty,\,\mathrm{IN}}$ = 12km/s, 118.5 deg;for V_{T} and $V_{\infty,\,\mathrm{IN}}$ = 12 km/s, 137.8 deg. As the contour approaches 16 km/s, the maximum angle between V_{T} and $V_{\infty,\,\mathrm{IN}}$ = 16 km/s approaches 180 deg, which means that a turn angle of 0 would be sufficient to perform the AGA maneuver. With the targeted lowest $V_{\infty,\,\mathrm{IN}}$ found in Fig. 4.19, the Titan encounter angle can be derived, which is ± 70 deg; and the corresponding Saturn arrival V_{∞} is 7 km/s.

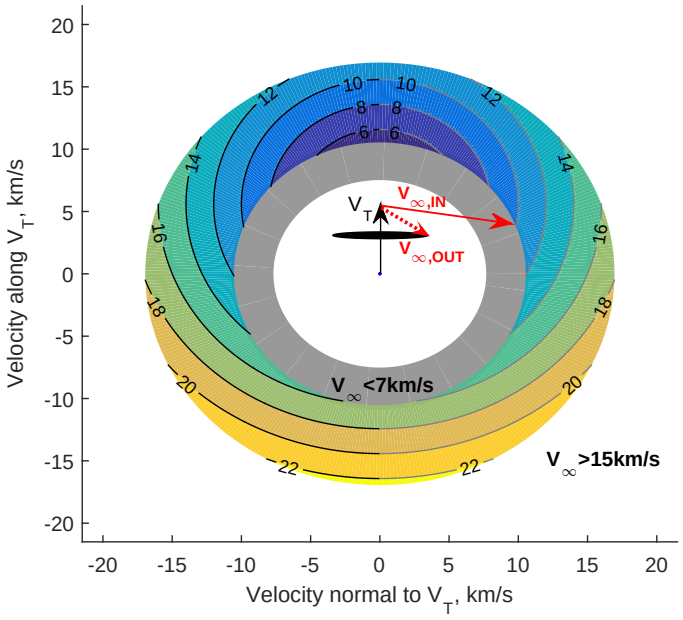

Figure 4.19. Representative limit of $V_{\infty,\,\mathrm{OUT}}$ (red dotted arrow) and $V_{\infty,\,\mathrm{IN}}$ (red solid arrow) of 10 km/s.

When considering $V_{\infty,\,\mathrm{IN}}$ of 10 km/s, the corresponding peak g-load is less than 6 g, peak heat rate less than 200 W/cm^2, and total heat load of around 25 kJ/cm^2. As a reference, Huygens probe entry on Titan resulted in a total heat load of 40 kJ/cm^2 with a peak heat rate of 50 W/cm^2. Such entry environments are somewhat comparable to the condition enabled by Adaptive Deployable Entry and Placement Technology (ADEPT) [63], which is designed for use on small satellites and could sustain a heat rate of up to 200 W/cm^2 [96]. However, ADEPT is built with layers of TPS materials and each layer can take a heat load of 2 kJ/cm^2 [97]; while options for 4, 8, and 12 layers of TPS materials for ADEPT have been investigated [98], the question remains that whether ADEPT could handle a total heat load of 25 kJ/cm^2.

4.4.2 Cassini-type Saturn System Mission

Extending the result to a conventional Saturn orbiter mission, one could use Titan AGA to get captured around Saturn which can help reduce propellant requirements from a propulsive capture. Figure 4.20 shows the $V_{\infty,\,\mathrm{OUT}}$ space where any of the points on this plot would result in a post-AGA trajectory in a closed Saturn orbit. Similar to the case for Enceladus mission, to minimize the design parameters, such as peak g-load, peak heat rate, and total heat load, the smallest $V_{\infty,\,\mathrm{IN}}$ possible is preferred. The $V_{\infty,\,\mathrm{IN}}$ as low as 5 km/s can be selected, i.e., the spacecraft encounters Titan at 0 deg, traveling in the same direction as Titan in orbit.

To illustrate the resultant peak g-load, peak heat rate, and total heat load for a Saturn mission, $V_{\infty,\,\mathrm{IN}}$ of 6 km/s is used. The blue dash circle in Fig. 4.20 represents the potential $V_{\infty,\,\mathrm{OUT}} = 6$ km/s with no drag loss. However, with AGA maneuver, the $V_{\infty,\,\mathrm{OUT}}$ should be inside the blue dash circle. Therefore, for $V_{\infty,\,\mathrm{IN}} = 6$ km/s, the potential $V_{\infty,\,\mathrm{OUT}}$ is the area overlaid by the black circle and the blue dash circle in Fig. 4.20.

At $V_{\infty,\,\mathrm{IN}}$ of 6 km/s, Fig. 4.21 shows the ranges for the three design parameters and the turn angle is limited between 10 deg and 40 deg. Given the low Titan arrival

velocity (i.e., low entry velocity), the peak g-load, peak heat rate, and total heat load are all very benign. As Fig. 4.21 shows, the peak g-load is only about 1.5, peak heat rate is topped at approximately 30 W/cm^2 and total heat load no more than 8 kJ/cm^2.

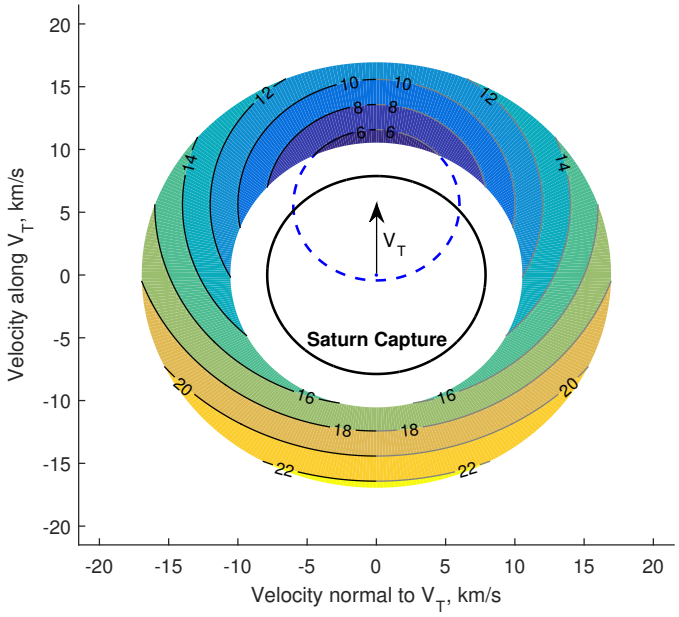

Figure 4.20. Vector diagram for Cassini-type Saturn mission; black circle encloses the possible $V_{\infty,\,\mathrm{OUT}}$ space for Saturn capture orbit; blue dash circle denotes the limit of $V_{\infty,\,\mathrm{OUT}}$=6 km/s.

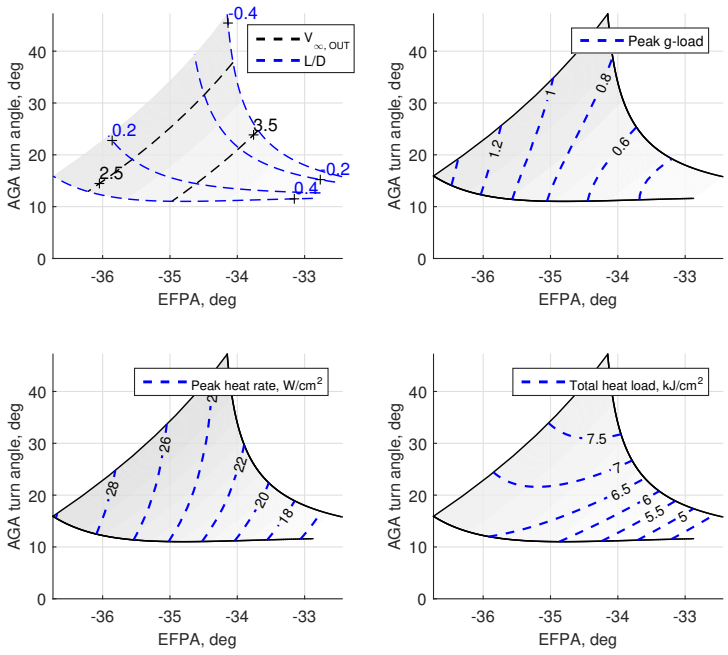

Figure 4.21. Contours of peak g-load, peak heat rate and total heat load at $V_{\infty,\,\mathrm{IN}} = 6$ km/s for maximum L/D of 0.4 and $V_{\infty,\,\mathrm{OUT}}$ of 2–5 km/s.

5. IMPROVED CONTROL OF AEROASSIST VEHICLE USING COMBINED LIFT AND DRAG MODULATION

5.1 Introduction

The challenge of outer planet exploration is the long flight times to arrive the target body. Reducing the time of flight requires the spacecraft to travel at higher speeds, which translate to a higher arrival velocity. Chemical propulsion has been the go-to approach for orbit insertion maneuvers. At high arrival velocity, the ΔV required for chemical orbit insertion may exceed the throughput of an engine. Previous studies have shown aerocapture enables a higher arrival velocity at ice giants (i.e., Uranus and Neptune) and requires a mid-L/D (0.6–0.8) vehicle [20]. However, the heritage entry vehicles have only flown at low-L/D range (0-0.4), and mid-L/D vehicles require further development [18]. There is a need for innovative approaches of aerocapture so that the missions can leverage the current state-of-the-art entry technology for aerocapture missions.

5.1.1 Control of Aeroassist Vehicles

Throughout an aerocapture maneuver, the spacecraft needs to compensate for the uncertainties, such as approach navigation, atmosphere modeling, and uncertainties in vehicle aerodynamic properties. The spacecraft must have some level of control authority to compensate for those uncertainties. There are three types of methods to provide control authority: lifting modulation (i.e., bank angle modulation or angle of attack modulation), drag modulation, and direct force control. Aerocapture using lifting vehicles has been studied extensively, and Ref. [10, 16, 17] provided a reference point-design for the aerocapture system to Neptune, Titan, and Venus. Putnam et

al. [30] studied drag modulation for aerocapture and showed the potential for missions to Venus and Mars. Saikia et al. [99] analyzed and compared the performance of ADEPT for landing at Mars and Venus using bank modulation, drag modulation, and angle-of-attack modulation. For aerocapture, previous studies have not considered the benefit of the combined lift and drag modulation.

The traditional entry vehicles either use ballistic entry or lifting entry. For example, lifting vehicles are used for Mars entry, descent, and landing to accommodate for very thin atmosphere and avoid the risk of crash landing [100]. Due to current advances (i.e., computational fluid dynamics analysis and ballistic range tests [101]) in drag-modulated systems for aeroassist maneuvers and entry and precision landing, there exists potential of combining both lift modulation and drag modulation to achieve a higher control authority. For consistency, lift and drag force (or deceleration) are defined as the force (or acceleration) components normal and parallel to the velocity vector, respectively.

Lift modulation (via bank angle control) has been the exclusive control method implemented in flight for human space flight and planetary missions. Lifting vehicles create aerodynamic lift by offsetting the vehicle's center of mass. The control of vehicle's trajectory is achieved through changing the orientation of the vehicle (i.e., the direction of the lift vector).

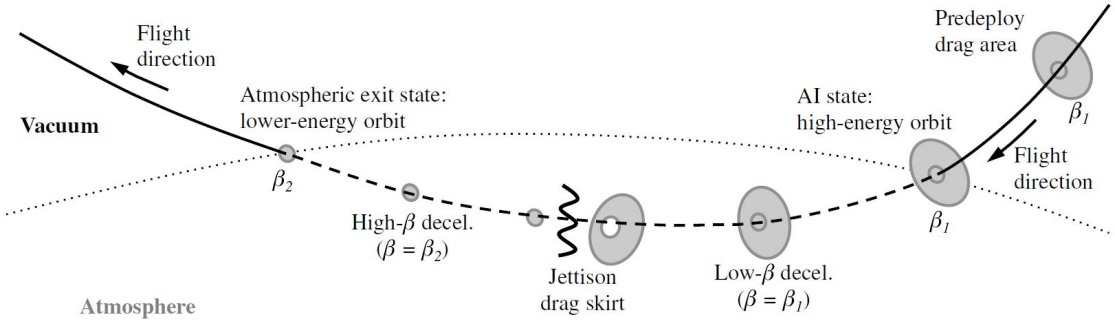

Figure 5.1. Illustration of single event drag-modulation aerocapture system, taken from Ref. [30].

Drag modulation uses essentially a ballistic vehicle (i.e., L/D of 0) which has the capability of changing the ballistic coefficient through deploying a drag skirt. Figure 5.1 shows an illustration of single-event drag modulation aerocapture system. The vehicle enters the atmosphere with a small initial ballistic coefficient β_1 and can increase its ballistic coefficient to as high as β_2. The control authority of a drag-modulated system depends on both the small β_1 and large β_2. A different way to characterize the control authority is small β_1 and the β-ratio as β_1/β_2 [30]. However, the following analysis assumes no particular control mode and the results are valid for both single-event drag control and continuous drag control.

5.1.2 Required Corridor Width

An estimate of the required corridor width is presented here, which is based on the Neptune aerocapture study [10]. There are mainly three errors from the required corridor width—approach navigation, atmospheric uncertainty, and uncertainties in aerodynamic properties.

Error in approach navigation requires a different assessment, some numbers from previous studies will be used. However, note that navigation error depends on the arrival velocity. In general, the higher the velocity, the higher the error.

5.1.3 Theoretical Corridor Width

Theoretical Corridor Width (TCW) is a measure of the control authority on a vehicle; while the required corridor width measures the amount of uncertainties. Both corridor widths use the unit of degree. Theoretical Corridor Width is the range between the allowable steepest and shallowest entry flight-path angles (EFPA) (γ_{max} and γ_{min} in Fig. 1.1), at which the spacecraft can successfully enter the orbit and achieve the target apoapsis altitude.

A vehicle with a theoretical corridor width of 2 deg, for example, can successfully compensate for a required corridor width of 2 deg; whereas a theoretical corridor width

of 1 deg is not sufficient for a required corridor width of 2 deg. The consequences of not having enough control authority (i.e., theoretical corridor width) is that the vehicle cannot guarantee the successful capture of the vehicle, which may result in entering the atmosphere entirely or escaping upon exiting the atmosphere.

Two definitions for corridor width may be used in this context: (1) The overshoot and undershoot boundaries corresponding to maximum and minimum flight-path angles that captures the vehicle to the desired apoapsis radius; (2) The overshoot boundary defines the shallowest flight-path angle that captures the vehicle around the celestial body, i.e., specific energy barely less than 0. The undershoot boundary defines the steepest flight-path angle at which the vehicle enters the orbit. The former will be used in the simulation results.

The definition of entry corridor width also depends on the altitude where the entry flight-path angle is defined. Orbit mechanics show that for the same trajectory, higher altitude corresponds to a larger corridor width. To be consistent with previous work, entry flight-path angle is defined at the altitude of sensible atmosphere.

It is important to note that although the term drag modulation and bank modulation may refer to particular vehicle control methods, however, this analysis in this chapter is also valid for lift modulations, which would change both vehicle L/D and ballistic coefficient are modulated at the same time; for example, through angle-of-attack modulation [102].

5.1.4 Objective

This chapter offers a novel control approach for aeroassist vehicles and the the results can help the mission design community to quickly assess the vehicle requirements for aeroassisted missions and provide guidance for future technology investments. The analysis evaluates the control methods of aeroassist vehicles which is applicable to aerocapture, aerogravity-assist, and entry. The control authorities for lift modulation, drag modulation, and combined lift and drag modulations are quantified by

evaluating the theoretical corridor width for a wide range of vehicle configurations (i.e., different L/D and ballistic coefficients). Improvements in the control authorities of the combined lift modulation and drag modulation is shown, compared with the control authorities of lift-modulation only vehicles.

5.2 Methodology: TCW Assessment

This section presents the example test cases for Uranus aerocapture, assuming arrival V_∞ of 20 km/s and a post-capture apoapsis radius of an elliptical orbit of 5 days. The altitude of the entry interface is 1500 km. For a single value of L/D and upper and lower values of ballistic coefficients, there are a total of six configurations. Table 1 lists all six configurations along with the corresponding nominal entry flight-path angles. Observing that the nominal entry flight-path angles are different for each case. Then combining different cases results in a total of five scenarios as shown in Table 5.2. Cases 2 and 4 correspond to the shallowest and steepest entry flight-path angles respectively for drag modulation with $\beta_1 = 100$ kg/m^2 and $\beta_2 = 500$ kg/m^2; cases 1 and 5 correspond to bank angle modulation for vehicle with $\beta = 100$ kg/m^2 and L/D = 0.3; cases 3 and 6 correspond to bank angle modulation for vehicle with $\beta = 500$ kg/m^2 and L/D = 0.3; and cases 1 and 6 correspond to bank angle modulation for vehicle with $\beta = 500$ kg/m^2 and L/D = 0.3.

Table 5.1. Nominal entry flight-path angle for Uranus aerocapture at V_∞ of 20 km/s.

Case	Description	Entry flight-Path angle, deg
1	$\beta = 100$, L/D = 0.3 (lift-down)	-14.28
2	$\beta = 100$, L/D = 0	-14.60
3	$\beta = 500$, L/D = 0.3 (lift-down)	-14.77
4	$\beta = 500$, L/D = 0	-15.13
5	$\beta = 100$, L/D = 0.3 (lift-up)	-15.21
6	$\beta = 500$, L/D = 0.3 (lift-up)	-15.75

Table 5.2. Theoretical corridor width for different scenarios; V_∞ of 20 km/s

Scenario	Cases	β	L/D	TCW, deg
1. Drag modulation	2 & 4	100 & 500	0	0.54
2. Bank modulation	1 & 5	100	0.3	0.93
3. Bank modulation	3 & 6	500	0.3	0.98
4. Bank & drag modulation	1 & 6	100 & 500	0.3	1.47
5. Bank or drag modulation	2 & 6	100 & 500	0 & 0.3	1.15

It is obvious that scenario 4 with combined bank and drag modulation offers the highest TCW at 1.47 deg as compared with drag modulation (two β of 100 and 500 kg/m^2) at 0.54 deg, bank modulation with β = 100 kg/m^2 and L/D=0.3 at 0.93 deg, and bank modulation with β = 100 kg/m^2 and L/D=0.3 at 0.98 deg. Results in Chapter 3 showed that the theoretical corridor width varies only slightly with ballistic coefficients, which is also confirmed with 0.93 and 0.98 deg for two configurations of bank modulation. The largest theoretical corridor width corresponds to two configurations—one is the small ballistic coefficient at lift-down configuration and another the larger ballistic coefficient at lift-up configuration.

Scenario 5 has the second largest theoretical corridor width—the shallow side is ballistic entry with $\beta = 100$ kg/m^2 and steep side is for $\beta = 500$ kg/m^2 and L/D=0.3. Scenario 5 may be of particular interest, since it can be difficult for a vehicle to achieve L/D = 0.3 while having a large drag area. If the vehicle can only increase ballistic coefficient (i.e., jettison drag skirt), control of the vehicle would follow two stages—first is drag modulation by skirt jettison and second is bank modulation only after the skirt deployment. However, if the vehicle has an initial configuration of $\beta = 100$ kg/m^2 and is able to deploy and jettison a drag skirt, the system may be more robust given one additional event for drag modulation. However, the latter can be technically challenging to implement. Regardless, the theoretical corridor width

results shown in later sections do not assume a specific control mode; and the same applies to all other scenarios.

To illustrate the difference in the trajectories, Figures 5.2 and 5.3 show the profiles of aerocapture trajectories for cases 1, 3, 5, and 6. Results in the following sections compare the theoretical corridor width from scenario 4 and 5 with scenario 2 or 3 (as in Table 5.2).

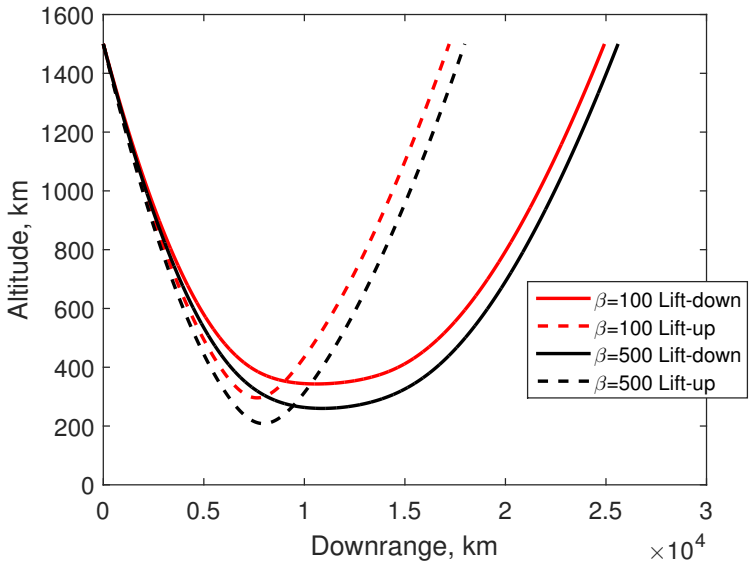

Figure 5.2. Aerocapture trajectory profiles (altitude vs. downrange) using L/D of 0.3 and V_∞ of 20 km/s.

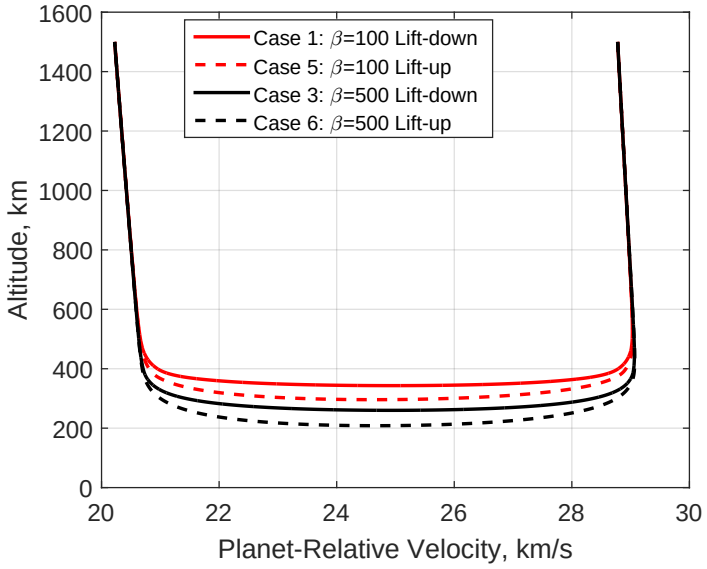

Figure 5.3. Aerocapture trajectory profiles (altitude vs. velocity) for L/D of 0.3 and V_∞ of 20 km/s.

5.3 Results and Discussion: Uranus Aerocapture

5.3.1 Scenario 4 at V_∞ of 20, 15, and 10 km/s

Figure 5.4 shows the nominal entry flight-path angles with different vehicle configurations, that is β values of 50, 200, 1000 kg/m^2 and L/D from 0 to 1.0. In Fig. 5.4, L/D=0 refers to the ballistic cases and note that the curves of the same color intercept at L/D=0, which means a zero deg theoretical corridor width for drag modulation with the two corresponding β values. Also note at L/D=0, the difference between two intercept points is the theoretical corridor width. When L/D increases, the control authority from L/D is more dominant and the contribution from the ballistic coefficients becomes smaller.

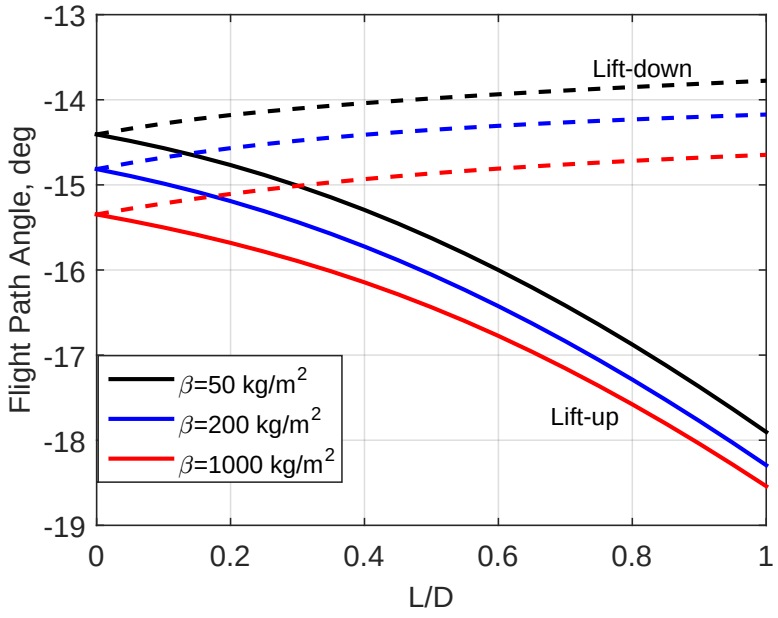

Figure 5.4. Nominal entry flight-path angles for L/D from 0–1 and three values of ballistic coefficients; Uranus arrival V_∞ of 20 km/s.

Considering a range of L/D from 0–1 and a range of β-ratios from 1–20, Fig. 5.5 shows the contours of theoretical corridor widths. Note that for vehicle L/D=0 and β-ratio of 1, the theoretical corridor width is 0 deg. As L/D increases and β-ratio

increases, the theoretical corridor width gets larger. The black solid contours, black dash contours, and red dash-dot contours almost overlap, meaning that the theoretical corridor width varies only slightly when β_1 changes from 25 to 50 kg/m^2 and to 150 kg/m^2.

As an example, assuming a required corridor width of 1.5 deg, β_1 of 50 kg/m^2, and L/D of 0.3, β-ratio of 3.5 is needed to achieve the required corridor; that is equivalent of using a drag skirt with twice the radius as the primary aeroshell. However, if increasing the value of β_1 to 150 kg/m^2, and assuming a required corridor width of 1.5 deg, a vehicle with L/D of 0.4 and β-ratio of 6 is sufficient.

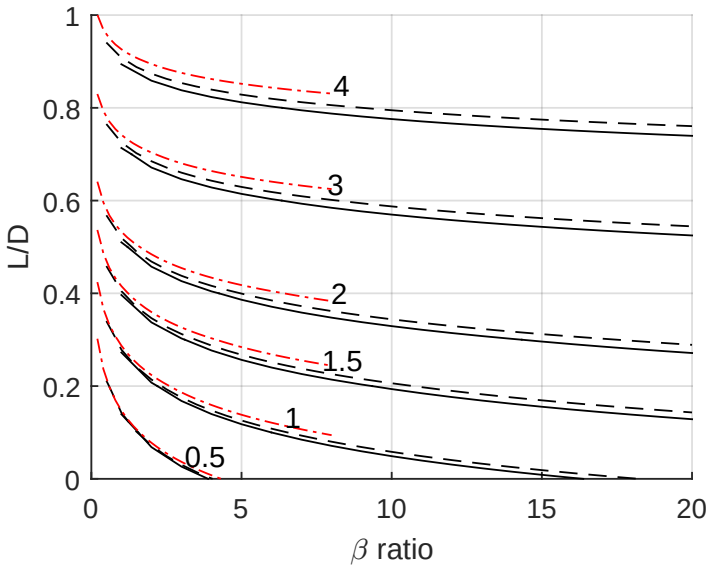

Figure 5.5. Contours of theoretical corridor width at V_∞ of 20 km/s for $\beta_1 = 25$ kg/m^2 (solid), $\beta_1 = 50$ kg/m^2 (dash), and $\beta_1 = 150$ kg/m^2 (red dash-dot).

Figure 5.6 shows the differences between theoretical corridor width for the combined approach and that of bank modulation only with $\beta = 25$ kg/m^2. At small β-ratio, the increase in TCW is almost constant across the entire range of L/D. However, when β-ratio is larger than 5, the increase in TCW is more significant as a result of increasing β-ratio. The same result was inferred from Fig. 5.4. Considering

a vehicle with low-L/D (0–0.4), L/D=0.2, for example, adding vehicle control using a β-ratio of 4 increases the corridor width by 0.5 deg.

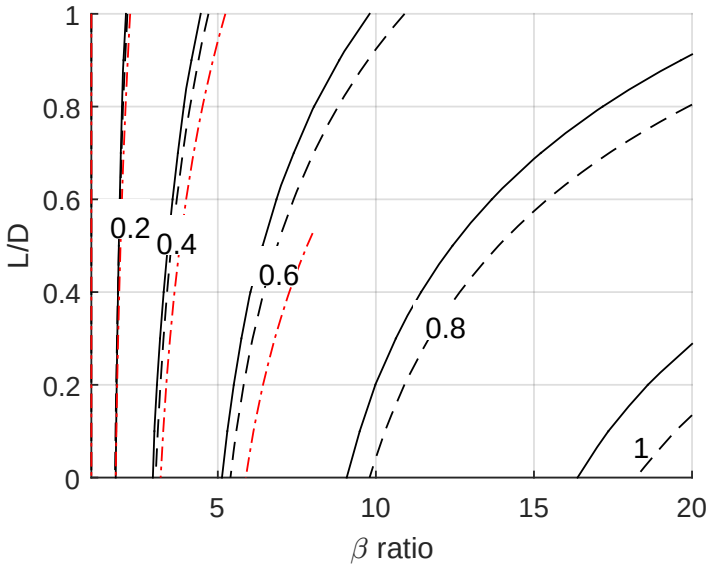

Figure 5.6. Increase in theoretical corridor width for V_∞=20 km/s as compared to β-ratio of 1 and β_1 of 25 kg/m^2 (solid), 50 kg/m^2 (dash), and 125 kg/m^2 (red dash-dot).

Figure 5.7 and 5.8 show the contours of theoretical corridor widths for Uranus aerocapture at V_∞ of 15 km/s and 10 km/s respectively. As compared with the theoretical corridor width for V_∞ of 20 km/s (as shown in Fig. 5.5), the corridor width for lower V_∞ is smaller than that for higher V_∞. The three contours of the same level in both Figs. 5.7 and 5.8 are relatively close. Thus, increasing β_1 from 25 to 50, then to 125 kg/m^2 only result in a small increase in the theoretical corridor width, which is similar to the result for V_∞ of 20 km/s.

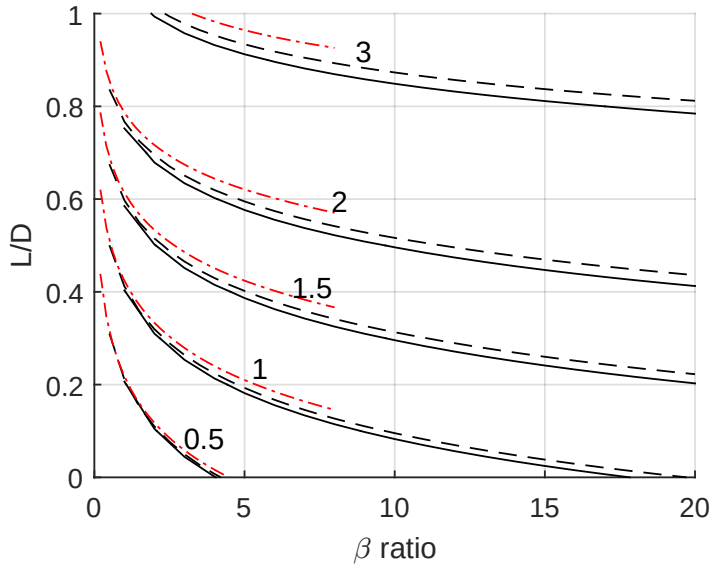

Figure 5.7. Contours of theoretical corridor width for $\beta_1 = 25$ kg/m^2 (solid) and $\beta_1 = 50$ kg/m^2 (dash), and 125 kg/m^2 (red dash-dot); $V_\infty = 15$ km/s.

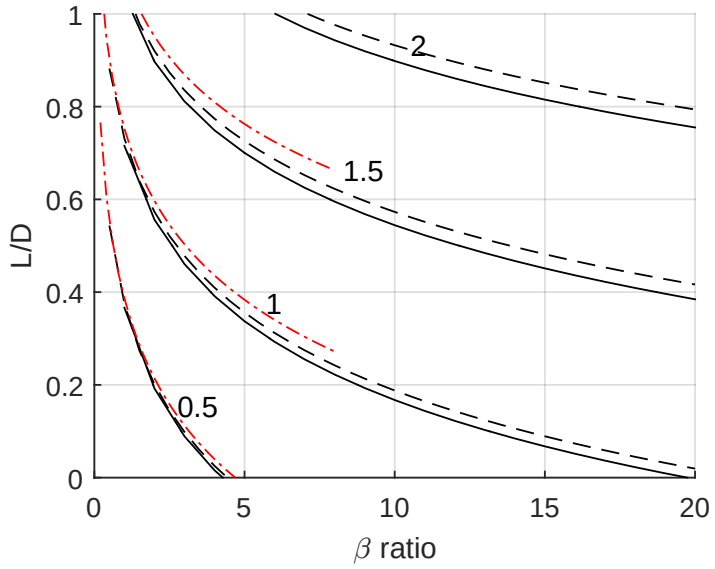

Figure 5.8. Contours of theoretical corridor width for $\beta_1 = 25$ kg/m^2 (solid) and $\beta_1 = 50$ kg/m^2 (dash), and 125 kg/m^2 (red dash-dot); $V_\infty = 10$ km/s.

5.3.2 Scenario 5 at V_∞ of 20, 15, and 10 km/s

Figures 5.9, 5.10, and 5.11 show the contours of theoretical corridor widths for aerocapture at Uranus at 20, 15, and 10 km/s respectively. Results are shown for β_1 of 25, 50, and 125 kg/m^2. For all three figures, the three contours of the same level in Fig. 5.7 are relatively close to each other, showing that the differences in theoretical corridor width are small for different values of β_1. However, comparing the results for different V_∞, the theoretical corridor width get smaller as V_∞ decreases. The same results was also observed in Chapter 3 for Uranus aerocapture.

Assuming a required corridor width of 1.5 deg and a low-L/D vehicle, for arrival V_∞ of 20 and 15 km/s, there exist some combinations of L/D and β-ratio that would offer 1.5 deg in theoretical corridor width. For V_∞ of 20 km/s, a vehicle with L/D of 0.4, β_1 of 50 kg/m^2, and β-ratio of 5 would result in sufficient corridor width of 1.5 deg. For V_∞ of 20 km/s, a vehicle with L/D of 0.4, β_1 of 50 kg/m^2, and β-ratio of 5 would offer sufficient control. However for V_∞ of 10 km/s, there is no combination of L/D and β ratio that would produce enough control authority. It is important to note the assumption that β-ratio is capped at 20. A large enough β-ratio would have the required control authority, which however, would be very difficult to achieve.

If assuming a required corridor with of 1 deg and a low-L/D vehicle and also using β_1 of 50 kg/m^2, there are combinations of L/D and β-ratio for all three V_∞ considered—for V_∞ of 20 km/s, L/D of 0.3 and β-ratio of 2.5; for V_∞ of 15 km/s, L/D of 0.3 and β-ratio of 6; for V_∞ of 10 km/s, L/D of 0.4 and β_1 of 8.5. Note that the combination chosen is one of the many available.

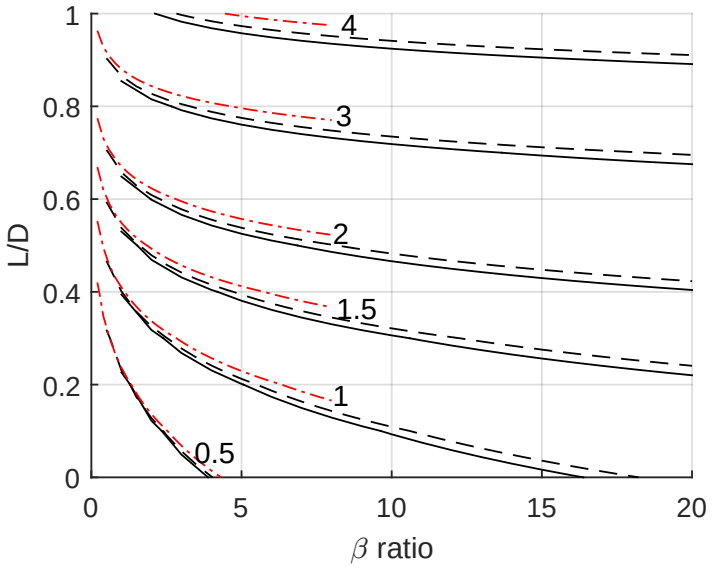

Figure 5.9. Contours of theoretical corridor width for $\beta_1 = 25$ kg/m^2 (solid), $\beta_1 = 50$ kg/m^2 (dash), $\beta_1 = 150$ kg/m^2 (red dash-dot); V_∞ of 20 km/s.

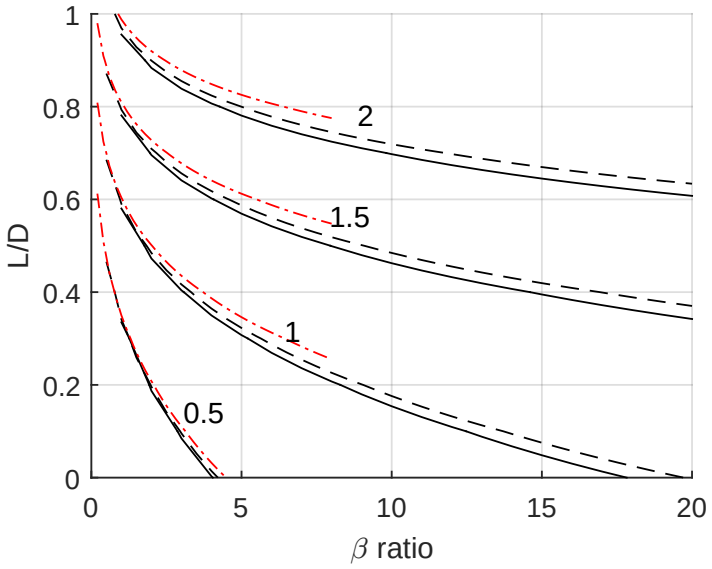

Figure 5.10. Contours of theoretical corridor width for $\beta_1 = 25$ kg/m^2 (solid), $\beta_1 = 50$ kg/m^2 (dash), $\beta_1 = 150$ kg/m^2 (red dash-dot); V_∞ of 15 km/s.

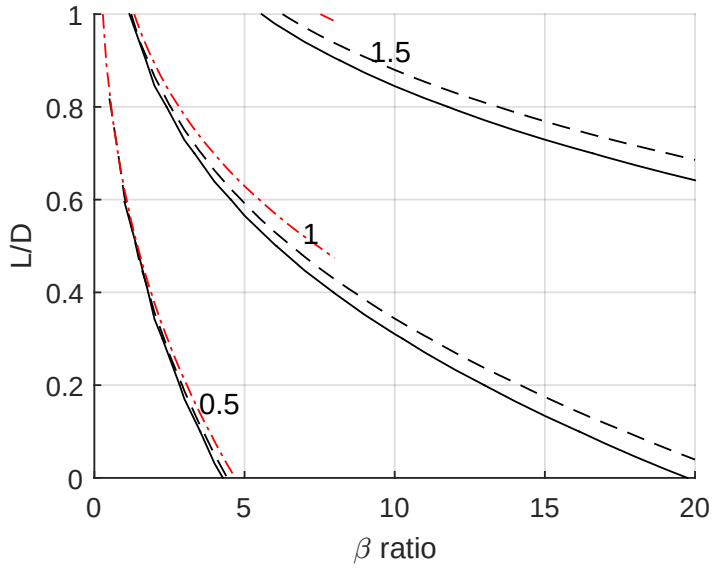

Figure 5.11. Contours of theoretical corridor width for $\beta_1 = 25$ kg/m^2 (solid), $\beta_1 = 50$ kg/m^2 (dash), $\beta_1 = 150$ kg/m^2 (red dash-dot); V_∞ of 10 km/s.

Figure 5.12 shows the increase in theoretical corridor width as compared with the case of bank modulation only (i.e., β-ratio of 1). The results are shown for β_1 of 50 kg/m^2 and three arrival V_∞—10, 15, and 20 km/s. An interesting observation that at around L/D of 0.38, three contours roughly overlap each, meaning that the same β-ratio on a vehicle with L/D of 0.38 results in the same increase in theoretical corridor width at all arrival V_∞. For L/D lower than 0.38, adding β-ratio would result in a larger increase in theoretical corridor width at higher V_∞; whereas for L/D higher than 0.38, adding β-ratio would result in a smaller increase in theoretical corridor width at higher V_∞.

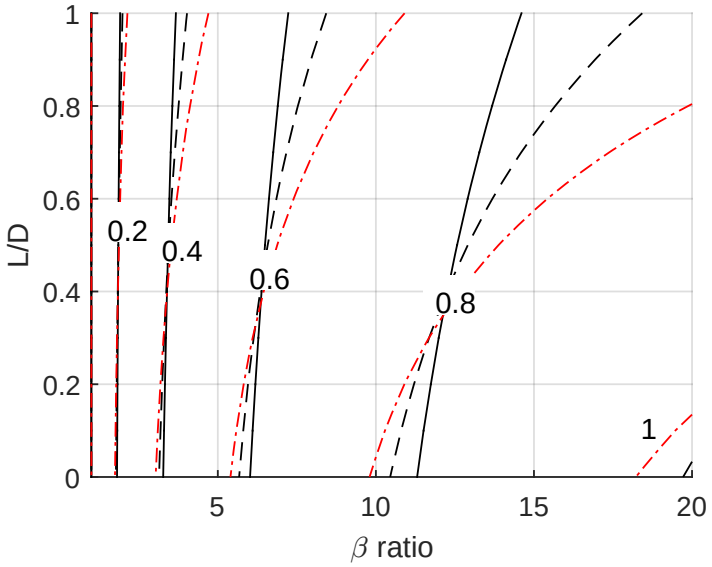

Figure 5.12. Increase in theoretical corridor width as compared to β-ratio of 1 and β_1 of 50 kg/m^2 at V_∞ of 10 km/s (solid), 15 km/s (dash), and 20 km/s (dash-dot).

6. CONCLUDING REMARKS

6.1 Conclusion

6.1.1 Aerocapture Design Methodology and Performance Analysis

Results in Chapter 3 have shown the various design rules and relations for mission designs using aerocapture. As aerocapture is a feasible and promising option for orbit insertion at Titan, Venus, and Uranus, it is important that different interplanetary arrival trajectories must be used when comparing aerocapture with propulsive capture. For example for Titan, propulsive options for orbit insertion can be applied to an arrival V_∞ of 4.5 km/s, whereas aerocapture requires an arrival V_∞ of at least 5 km/s when using a vehicle with L/D = 0.2.

Increasing the vehicle L/D lowers the limit on V_∞, however, achieving a high L/D with traditional entry vehicle designs may be extremely challenging. The lower limit on vehicle L/D is driven by the required corridor width. To ensure the performance of aerocapture, reducing required corridor width would increase aerocapture robustness. Different values of peak g-load were identified on the plots; and the results showed that peak g-load is not the limiting factor for aerocapture at Titan. On the contrary, aerothermodynamics heating is the primary driving factor for aerocapture vehicle design. Of the two heating parameters, peak heat rate is well within the limit of current TPS technology. Total heat load is a more important design parameter, especially when the vehicle has a large ballistic coefficient. Vehicle ballistic coefficient affects heating significantly. On the contrary, ballistic coefficient has a minimal effect on peak g-load. As shown, post-aerocapture TCM requires a ΔV of at least 140 m/s. As this study only evaluated convective heating using empirical relation, further computation or experimental analysis is necessary to estimate radiative heating.

As uncertainties in interplanetary guidance and navigation and atmosphere model improve to reduce the required corridor width, one could consider using a conventional low-L/D rigid blunt body entry vehicle design for aerocapture in the future. Aerocapture enables a higher arrival V_∞ as opposed to propulsive orbit insertions, which could result in achieving a reduction in flight times, or an increase in the delivered payload mass fraction, or both.

6.1.2 Design Methodology using Titan Aerogravity-Assist for Saturn System Missions

A novel design methodology is presented and it combines a graphical method using vector diagrams and physical constraints. Saturn mission concepts using aerogravity-assist maneuver at Titan is investigated, with emphasis on Enceladus missions. The results have shown the potential of using Titan to perform aerogravity-assist maneuver for both a Saturn system mission and an Enceladus mission. The ranges of values for key design parameters—peak g-load, peak heat rate, and total heat load—show that it may be possible to use the next-generation deployable entry system (i.e., ADEPT) to perform Titan aerogravity-assist. A peak heat rate of less than 30 W/cm^2 for a Saturn mission is very benign and there could be potential for dual-use heatshields that would merit a sample return mission.

6.1.3 Improved Control Authority for Aeroassist Vehicles

This investigation presented the improvement in control authority by leveraging both drag and bank modulation and the results showed the benefit of achieving a higher control authority on aerocapture vehicle. Using a combination of bank modulation and drag modulation, improvement in vehicle control authority can be made for aerocapture at Uranus. The analysis and results can also be applied to active force control or lift modulation where angle of attack can be changed. Combining the lifting capability with drag modulated vehicle increases the system complexity and

perceived risk, and technology development is needed before such an approach can be implemented. Nevertheless, the results showed promising increase of control authority when combining bank modulation and drag modulation, even for scenario 5, where the control authority is reduced from the full combined bank and drag modulation.

6.2 Recommendations and Future Works

Following the investigations presented in this dissertation, there are many possibilities for future works. The design methodologies open up many mission concept options using aerocapture. For example, multiple-use heatshields can be considered for more complicated mission scenarios that use more than one aeroassist maneuvers. Also, the design methodology can be extended to include more detailed analysis, e.g., TPS mass analysis for more accurate mass estimates. As the aerocapture design methodologies can be wrapped into a design tool, it can also include other capabilities such as guidance and control performance analysis, that would help quantify the required corridor width for all conditions. In addition, improvements in the simulations can be made by including high-fidelity models for gravity and atmosphere; wind effects, although minor, can also be included in the analysis.

As the previous studies have used the inaccurate assumptions for interplanetary trajectory, the cost and benefit for aerocapture missions compared with missions using chemical propulsion can be reassessed and quantified for all bodies considering different interplanetary transfer options.

Specific for aerogravity-assist, given detailed mission scenarios, the analysis can be extended to quantify the performance for arrival at non-zero declination and include the effect of crank angle changes through the maneuver. The analysis in this dissertation did not include wind effect for the trajectory during atmospheric pass, in the future, the wind effect will be included that helps identify the preferred orbit for entry (i.e., prograde or retrograde). In addition, third body perturbation will be analyzed to increase the fidelity of the analysis for the post-AGA orbit.

The vector diagram analysis described can be extended to cases with transfer within the Solar System, such as a sample return mission from the outer planets while using Mars or Venus for orbit transit. The methodology can be used to perform mission design and trade analysis beyond traditional methods such as gravity-assist or moon tours. Multiple-use heatshields can also be considered using aerogravity-assist maneuver in combination with the aerocapture maneuver.

REFERENCES

[1] Jon A Sims, James M Longuski, and Moonish R Patel. Aerogravity-assist trajectories to the outer planets. *Acta Astronautica*, 35:297–306, 1995.

[2] Donald R Merritt. Venus Express: Aerobraking and Post-Aerobraking Science Operations. In *AIAA SPACE 2015 Conference and Exposition*, Pasadena, CA, 2015. American Institute of Aeronautics and Astronautics.

[3] Daniel T Lyons, R.Stephen Saunders, and Douglas G Griffith. The Magellan Venus mapping mission: aerobraking operations. *Acta Astronautica*, 35(9-11):669–676, 1995.

[4] Daniel T Lyons, Joseph G Beerer, Pasquale Esposito, M Daniel Johnston, and William H Willcockson. Mars Global Surveyor: Aerobraking Mission Overview. *Journal of Spacecraft and Rockets*, 36(3):307–313, 1999.

[5] John C Smith and Julia L Bell. 2001 Mars Odyssey Aerobraking. *Journal of Spacecraft and Rockets*, 42(3):406–415, 2005.

[6] Daniel Lyons. Mars Reconnaissance Orbiter: Aerobraking Reference Trajectory. In *AIAA/AAS Astrodynamics Specialist Conference and Exhibit*, Monterey, CA, 2002. American Institute of Aeronautics and Astronautics.

[7] Marta R.R. de Oliveira, Paulo J.S. Gil, and Richard Ghail. A novel orbiter mission concept for venus with the EnVision proposal. *Acta Astronautica*, 148:260–267, 2018.

[8] Gerald D. Walberg. A Survey of Aeroassisted Orbit Transfer. *Journal of Spacecraft and Rockets*, 22(1):3–18, 1985.

[9] Surjit Varma and Krishna Dev Kumar. Multiple Satellite Formation Flying Using Differential Aerodynamic Drag. *Journal of Spacecraft and Rockets*, 49(2):325–336, 2012.

[10] Mary Kae Lockwood, Karl T. Edquist, Brett R. Starr, Brian R. Hollis, Glenn A. Hrinda, Robert W. Bailey, Jeffery L. Hall, Thomas R. Spilker, Muriel A. Noca, N. O'Kongo, Robert J. Haw, Carl G. Justus, Aleta L. Duvall, Vernon W. Keller, James P. Masciarelli, David A. Hoffman, Jeremy R. Rea, Carlos H. Westhelle, Claude A. Graves, Naruhisa Takashima, Kenneth Sutton, Josephe Olejniczak, Y. K. Chen, Michael J. Wright, Bernard Laub, Dinesh Prabhu, R. Eric Dyke, and Ramadas K. Prabhu. Aerocapture Systems Analysis for a Neptune Mission. Technical report, NASA/TM-2006-214300, 2006.

[11] Howard S London. Change of Satellite Orbit Plane by Aerodynamic Maneuvering. *Journal of the Aerospace Sciences*, 29(3):323–332, 1962.

[12] Jim J. Jones. The Rationale for an Aeroassist Flight Experiment. In *22nd Thermophysics Conference*, Honolulu, HI, 1987. AIAA-87-1508.

[13] A Miele, T Wang, W.Y. Lee, and Z.G. Zhao. Optimal trajectories for the aeroassisted flight experiment. *Acta Astronautica*, 21(11-12):735–747, 1990.

[14] A Miele, Z G Zhao, and W Y Lee. Optimal Trajectories for the Aeroassisted Flight Experiment. Part 1: Equations of Motion in an Earth-fixed System. Technical report, Rice University, 1989.

[15] A Miele, Z. G. Zhao, and W. Y. Lee. Optimal Trajectories For the Aeroassisted Flight Experiment, Part 2, Equations of Motion In an Intertial System. Technical report, Rice University, 1989.

[16] Mary Kae Lockwood, Brett R. Starr, John W. Paulson, Dean A. Kontinos, Y. K. Chen, Bernard Laub, Joseph Olejniczak, Michael J. Wright, Naruhisa Takashima, Carl G. Justus, Aleta L. Duval, Jeffery L. Hall, Robert W. Bailey, Robert J. Haw, Muriel A. Noca, Thomas R. Spilker, Claude A. Graves, Christopher J. Cerimele, Carlos H. Westhelle, Vernon W. Keller, and Kenneth Sutton. Systems Analysis for a Venus Aerocapture Mission. Technical report, NASA/TM-2006-214291, 2006.

[17] Mary K. Lockwood, Eric M. Queen, David W. Way, Richard W. Powell, Karl Edquist, Brett W. Starr, Brian R. Hollis, E. Vincent Zoby, Glenn A. Hrinda, Robert W. Bailey, Jeffery L. Hall, Thomas R. Spilker, Muriel Noca, Robert Haw, Carl G. Justus, Aleta Duvall, Dale L. Johnson, James Masciarelli, Naruhisa Takashima, Kenneth Sutton, Joe Olejniczak, Bernard Laub, Michael J. Wright, Dinesh Prabhu, and R. Eric Dyke. Aerocapture Systems Analysis for a Titan Mission. Technical report, NASA/TM-2006-214273, 2006.

[18] Thomas R Spilker, Mark Adler, Nitin Arora, Patricia M Beauchamp, James A Cutts, Michelle M Munk, Richard W Powell, Robert D Braun, and Paul F Wercinski. Qualitative Assessment of Aerocapture and Applications to Future Missions. *Journal of Spacecraft and Rockets*, 56(2):536–545, 2019.

[19] Thomas R. Spilker, Chester S. Borden, Mark Adler, Michelle M Munk, Richard W. Powell, Robert D. Braun, Patricia M. Beauchamp, James A. Cutts, Paul F. Wercinski, and JPL A-Team. An Assessment of Aerocapture and Applications to Future Missions. Technical report, JPL D-97058, 2016.

[20] Mark D Hofstadter, Amy Simon, and Kim Reh. Ice Giants Pre-Decadal Study Final Report. Technical report, NASA, 2017.

[21] Sarag Saikia, Jay Millane, Alec Mudek, Archit Arora, Paul Witsberger, Eiji Shibata, Luis Podesta, Ye Lu, Peter Edelman, James Longuski, and Kyle Hughes. Aerocapture Assessment at Uranus and Neptune for NASA's Ice Giant Studies. Technical report, PU-AAC-2016-MC-0002, West Lafayette, IN, 2016.

[22] J. E. Lyne, A. Anagnost, and M. E. Tauber. Parametric study of manned aerocapture. II - Mars entry. *Journal of Spacecraft and Rockets*, 29(6):814–819, 1992.

[23] J. E. Lyne, M. E. Tauber, and Robert D. Braun. Parametric study of manned aerocapture. I - Earth return from Mars. *Journal of Spacecraft and Rockets*, 29(6):808–813, 1992.

[24] Scott Craig and James E. Lyne. Parametric Study of Aerocapture for Missions to Venus. *Journal of Spacecraft and Rockets*, 42(6):1035–1038, 2005.

[25] Ye Lu and Sarag J Saikia. Feasibility Assessment of Aerocapture for Future Titan Orbiter Missions. *Journal of Spacecraft and Rockets*, 55(5):1125–1135, 2018.

[26] Jeffery L Hall, Muriel A Noca, and Robert W Bailey. Cost-Benefit Analysis of the Aerocapture Mission Set. *Journal of Spacecraft and Rockets*, 42(2):309–320, 2005.

[27] Parul Agrawal, Gary A. Allen, Evgeniy B. Sklyanskiy, Helen H. Hwang, Loc C. Huynh, Kathy McGuire, Mark S. Marley, Joseph A. Garcia, Jose F. Aliaga, and Robert W. Moses. Atmospheric Entry Studies for Uranus. In *2014 IEEE Aerospace Conference*, pages 1–19. IEEE, 2014.

[28] A. Miele. Recent Advances in the Optimization and Guidance of Aeroassisted Orbital Transfers. *Acta Astronautica*, 38(10):747–768, 1996.

[29] Ping Lu, Christopher J. Cerimele, Michael A. Tigges, and Daniel A. Matz. Optimal Aerocapture Guidance. *Journal of Guidance, Control, and Dynamics*, 38(4):553–565, 2015.

[30] Zachary R Putnam and Robert D Braun. Drag-Modulation Flight-Control System Options for Planetary Aerocapture. *Journal of Spacecraft and Rockets*, 51(1):139–150, 2014.

[31] Jordi Puig-Suari, James M. Logunski, and Steven G Tragesser. Aerocapture with a Flexible Tether. *Journal of Guidance, Control, and Dynamics*, 18(6):1305–1312, 1995.

[32] Steven G Tragesser and James M Longuski. Analysis and Design of Aerocapture Tether with Accounting for Stochastic Errors. *Journal of Spacecraft and Rockets*, 35(5):683–689, 9 1998.

[33] Paul Williams, Sherrin Yeo, and Chris Blanksby. Heating and Modeling Effects in Tethered Aerocapture Missions. *Journal of Guidance, Control, and Dynamics*, 26(4):643–654, 2003.

[34] Daniel Lyons and Wyatt Johnson. Ballute Aerocapture Trajectories at Titan. In *AIAA/AAS Astrodynamics Specialist Conference*, pages 1–13, Big Sky, Montana, 2003. AIAA.

[35] Daniel Lyons and Wyatt Johnson. Ballute Aerocapture Trajectories at Neptune. In *AIAA Atmospheric Flight Mechanics Conference and Exhibit*, Providence, Rhode Island, 2004. AIAA.

[36] Wyatt Johnson and Dan Lyons. Titan Ballute Aerocapture Using a Perturbed TitanGRAM Model. In *AIAA Atmospheric Flight Mechanics Conference and Exhibit*, number August, Providence, Rhode Island, 2004. AIAA.

[37] Kevin L Miller, Doug Gulick, Jake Lewist, Bill Trochman, Jim Stein, Daniel T Lyons, and Richard G Wilmoth. Trailing Ballute Aerocapture: Concept and Feasibility Assessment. In *AIAA Joint Propulsion Conference and Exhibit*, Huntsville, AL, 2003. AIAA, AIAA 2003-4655.

[38] Kristin L Gates Medlock, Mohammad a Ayoubi, James M Longuski, West Lafayette, Daniel T Lyons, Doctoral Candidate, and Senior Engineer. Analytic Solutions for Aerocapture, Descent, and Landing Trajectories for Dual-Use Ballute Systems. In *AIAA/AAS Astrodynamics Specialist Conference and Exhibit*, pages 1–, Keystone, CO, 2006.

[39] Reuben R Rohrschneider and Robert D Braun. Survey of Ballute Technology for Aerocapture. *Journal of Spacecraft and Rockets*, 44(1):10–23, 2007.

[40] Nathan J Strange and James M Longuski. Graphical Method for Gravity-Assist Trajectory Design. *Journal of Spacecraft and Rockets*, 39(1):9–16, 2002.

[41] Jon A Sims, James M Longuski, and Moonish R Patel. Aerogravity-Assist Trajectories to the Outer Planets and the Effect of Drag. *Journal of Spacecraft and Rockets*, 37(1):49–55, 2000.

[42] Gregory A. Henning, Peter J. Edelman, and James M. Longuski. Design and Optimization of Interplanetary Aerogravity-Assist Tours. *Journal of Spacecraft and Rockets*, 51(6):1849–1856, 2014.

[43] Eugene P. Bonfiglio, James M. Longuski, and Nguyen X. Vinh. Automated Design of Aerogravity-Assist Trajectories. *Journal of Spacecraft and Rockets*, 37(6):768–775, 2000.

[44] Steven Walker, Jeffrey Sherk, Dale Shell, Ronald Schena, John Bergmann, and Jonathan Gladbach. The DARPA/AF Falcon Program: The Hypersonic Technology Vehicle #2 (HTV-2) Flight Demonstration Phase. In *15th AIAA International Space Planes and Hypersonic Systems and Technologies Conference*, Dayton, OH, 2008. AIAA.

[45] Mark J. Lewis and Angus D. McRonald. Design of hypersonic waveriders for aeroassisted interplanetary trajectories. *Journal of Spacecraft and Rockets*, 29(5):653–660, 1992.

[46] Philip Ramsey and James E. Lyne. Investigation of Titan Aerogravity Assist for Capture into Orbit About Saturn. *Journal of Spacecraft and Rockets*, 43(1):231–233, 2006.

[47] Philip Ramsey and James E. Lyne. Enceladus Mission Architecture Using Titan Aerogravity Assist for Orbital Capture About Saturn. *Journal of Spacecraft and Rockets*, 45(3):635–638, 2008.

[48] Damon Landau, Try Lam, and Nathan Strange. Broad search and optimization of solar electric propulsion trajectories to Uranus and Neptune. *Advances in the Astronautical Sciences*, 135(3):2093–2112, 2009.

[49] Jon Sims, Paul Finlayson, Edward Rinderle, Matthew Vavrina, and Theresa Kowalkowski. Implementation of a Low-Thrust Trajectory Optimization Algorithm for Preliminary Design. In *AIAA/AAS Astrodynamics Specialist Conference and Exhibit*, Keystone, CO, 2006. AIAA.

[50] Jacob A Englander and Bruce A Conway. Automated Solution of the Low-Thrust Interplanetary Trajectory Problem. *Journal of Guidance, Control, and Dynamics*, 40(1):15–27, 2017.

[51] M. R. Zwack, P. D. Dees, H. D. Thomas, T. P. Polsgrove, and J. B. Holt. Program to Optimize Simulated Trajectories II (POST2) Surrogate Models for Mars Ascent Vehicle (MAV) Performance Assessment. Technical report, NASA, Huntsville, Alabama, 2017.

[52] Alireza Mazaheri, Peter A Gnoffo, Christopher O. Johnston, and Bil Kleb. LAURAN Users Manual: 5.5-65135. Technical report, NASA, Hampton, VA, 2013.

[53] Nguyen X. Vinh, Adolf Busemann, and Robert D. Culp. *Hypersonic and Planetary Entry Flight Mechanics*. The University of Michigan Press, 1980.

[54] Luciano Iess, Nicole J Rappaport, Robert A Jacobson, Paolo Racioppa, David J Stevenson, Paolo Tortora, John W Armstrong, and Sami W Asmar. Gravity field, shape, and moment of inertia of Titan. Technical Report 5971, 2010.

[55] Ravit Helled, Eli Galanti, and Yohai Kaspi. Saturns fast spin determined from its gravitational field and oblateness. *Nature*, 520(7546):202–204, 2015.

[56] Ravit Helled, John D. Anderson, Morris Podolak, and Gerald Schubert. Interior Models of Uranus and Neptune. *The Astrophysical Journal*, 726(1):15, 2011.

[57] E Lellouch and D. M Hunten. The Lellouch-Hunten Models for Titan's Atmosphere. In *Huygens: Science, Payload and Mission, Proceedings of an ESA conference*. 1997-ESA-SP1177, 1997.

[58] R. V. Yelle, D. F. Strobel, E Lellouch, and D Gautier. Engineering Models for Titan's Atmosphere. *European Space Agency, Special Publication*, pages 243–256, 1997.

[59] J. H. Waite, J. Bell, R. Lorenz, R. Achterberg, and F. M. Flasar. A Model of Variability in Titan's Atmospheric Structure. *Planetary and Space Science*, 86:45–56, 2013.

[60] A. J. Kliore, G. M. Keating, and V. I. Moroz. Venus international reference atmosphere (1985). *Planetary and Space Science*, 40(4):573, 1992.

[61] G F Lindal, J R Lyons, D N Sweetnam, V R Eshleman, D P Hinson, and G L Tyler. The atmosphere of Uranus: Results of radio occultation measurements with Voyager 2. *Journal of Geophysical Research*, 92(A13):14987–15001, 1987.

[62] Stephen Hughes, F. Cheatwood, Robert Dillman, Anthony Calomino, Henry Wright, Joseph DelCorso, and Anthony Calomino. Hypersonic Inflatable Aerodynamic Decelerator (HIAD)Technology Development Overview. In *21st AIAA Aerodynamic Decelerator Systems Technology Conference and Seminar*, Dublin, Ireland, 2011. AIAA.

[63] Ethiraj Venkatapathy, James Arnold, Ian Fernandez, Kenneth R. Hamm, David Kinney, Bernard Laub, Alberto Makino, Mary Kathleen McGuire, Keith Peterson, Dinesh Prabhu, Daniel Empey, Ian Dupzyk, Loc Huynh, Prabhat Hajela, Peter Gage, Austin Howard, and Dana Andrews. Adaptive Deployable Entry and Placement Technology (ADEPT): A Feasibility Study for Human Missions to Mars. In *21st AIAA Aerodynamic Decelerator Systems Technology Conference and Seminar*, Dublin, Ireland, 2011. AIAA.

[64] Jeremy M Knittel and Mark J Lewis. Concurrent Aerocapture with Orbital Plane Change Using Starbody Waveriders. *The Journal of the Astronautical Sciences*, 61(4):319–340, 2014.

[65] K. Sutton and R. A. Graves. A General Stagnation-Point Convective-Heating Equation for Arbitrary Gas Mixtures. Technical report, Washington, DC, 1971.

[66] L. Caillault, L. Walpot, T. E. Magin, A. Bourdon, and C. O. Laux. Radiative heating predictions for Huygens entry. *Journal of Geophysical Research*, 111(E9):E09S90, 2006.

[67] Jamshid A Samareh. A Multidisciplinary Tool for Systems Analysis of Planetary Entry, Descent, and Landing (SAPE). Technical report, NASA, 2009.

[68] William A. Page and Henry T. Woodward. Radiative and convective heating during Venus entry. *AIAA Journal*, 10(10):1379–1381, 1972.

[69] Andrew P Ingersoll and Thomas R Spilker. A Neptune Orbiter with Probes Mission with Aerocapture Orbit Insertion. In *NASA Space Science Vision Missions*, chapter 3, pages 81–114. 2008.

[70] Elizabeth Kolawa, Tibor Balint, Gaj Birur, Gary Bolotin, Eric Brandon, Linda Del Castillo, Henry Garrett, Jeffery Hall, Michael Johnson, Jack Jones, Insoo Jun, Ram Manvi, Mohammad Mojarradi, Alina Mossessian, Jagdish Patel, Michael Pauken, Craig Peterson, Rao Surampudi, Harald Schone, Jay Whitacre, Insoo Jun, Ed Martinez, Raj Venkapath, Bernard Laud, and Phil Neudeck. Extreme Environments Technologies for Future Space Science Missions. Technical report, NASA, 2007.

[71] Don Ellerby, Peter Gage, Cole Kazemba, Milad Mahzari, Owen Nishioka, Keith Peterson, Mairead Stackpoole, Ethiraj Venkatapathy, Zion Young, Carl Poteet, Scott Splinter, Mike Fowler, and Charles Kellermann. Heatshield for Extreme Entry Environment Technology (HEEET) Development Status. In *13th International Planetary Probe Workshop*, Laurel, MD, 2016.

[72] Karl T. Edquist, Artem A. Dyakonov, Michael J. Wright, and Chun Y. Tang. Aerothermodynamic Design of the Mars Science Laboratory Heatshield. In *41st AIAA Thermophysics Conference*, San Antonio, TX, 2007. AIAA 2009-4075.

[73] Nathan Strange, Thomas Spilker, Damon Landau, Try Lam, Daniel Lyons, and Jose Guzman. Mission design for the Titan Saturn system mission concept. In *AAS/AIAA Astrodynamics Conference*, Pittsburgh, PA,, 2009. AAS 09-356.

[74] James C Leary, Robert D Strain, Ralph D Lorenz, and Hunter J Waite. Titan Explorer Flagship Mission Study. Technical report, The Johns Hopkins University Applied Physics Laboratory, 2008.

[75] M.K. Bird, R. Dutta-Roy, M. Heyl, M. Allison, S.W. Asmar, W.M. Folkner, R.A. Preston, D.H. Atkinson, P. Edenhofer, D. Plettemeier, R. Wohlmuth, L. Iess, and G.L. Tyler. The Huygens Doppler Wind Experiment: Titan Winds Derived from Probe Radio Frequency Measurements. *Space Science Reviews*, 104(1-4):613–640, 2002.

[76] National Research Council. *Vision and Voyages for Planetary Science Decadal Survey 2013-2022*. The National Academies Press, Washington, DC, 2013.

[77] J. H. Waite and Curt Niebur. Mission Concept Study Planetary Science Decadal Survey JPL Team X Titan Lake Probe Study. Technical Report April, 2010.

[78] Ellen Stofan, R Lorenz, J. Lunine, E. B. Bierhaus, B. Clark, P. R. Mahaffy, and M. Ravine. TiME - The Titan Mare Explorer. In *2013 IEEE Aerospace Conference*, pages 1–10. IEEE, 2013.

[79] Kim Reh, Christian Erd, Dennis Matson, Athena Coustenis, Jonathan Lunine, and Jean-Pierre Lebreton. Titan Saturn System Mission A Joint Endeavour by ESA and NASA. Technical report, JPL, 2009.

[80] Joseph Olejniczak, Dinesh Prabhu, Michael Wright, Naru Takashima, Brian Hollis, Kenneth Sutton, and E. Zoby. An Analysis of the Radiative Heating Environment for Aerocapture at Titan. In *39th AIAA/ASME/SAE/ASEE Joint Propulsion Conference and Exhibit, Joint Propulsion Conferences*, number July, 2003.

[81] Natasha Bosanac, Jerrold E Marsden, Ashley Moore, and Stefano Campagnola. Titan Trajectory Design Using Invariant Manifolds and Resonant Gravity Assists. In *AAS/AIAA Space Flight Mechanics Meeting*, San Diego, CA, 2010.

[82] Robert Grimm, James Cutts, Martha Gilmore, Robert Herrick, Gary Hunter, Izenberg. Noam, Kandis Lea Jessup, and Robert Lillis. Venus Bridge: A Smallsat Program Through the Mid-2020s. In *12th Low-Cost Planetary Mission Conference*, 2017.

[83] Kyle M Hughes. *Gravity-Assist Trajectories to Venus, Mars, and The Ice Giants: Mission Design with Human and Robotic Applications*. PhD thesis, Purdue University, 2016.

[84] J. Mansell, N. Kolencherry, K. Hughes, A. Arora, H.S. Chye, K. Coleman, J. Elliott, S. Fulton, N. Hobar, B. Libben, Y. Lu, J. Millane, A. Mudek, L. Podesta, J. Pouplin, E. Shibata, G. Smith, B. Tackett, T. Ukai, P. Witsberger, and S. Saikia. Oceanus: A multi-spacecraft flagship mission concept to explore Saturn and Uranus. *Advances in Space Research*, 59(9):2407–2433, 2017.

[85] James Masciarelli, Carlos Westhelle, and Claude Graves. Aerocapture Guidance Performance for the Neptune Orbiter. In *AIAA Atmospheric Flight Mechanics Conference and Exhibit*, Providence, Rhode Island, 2004. AIAA.

[86] Peter Tsou, Donald E Brownlee, Christopher P. McKay, Ariel D Anbar, Hajime Yano, Kathrin Altwegg, Luther W Beegle, Richard Dissly, Nathan J Strange, and Isik Kanik. LIFE: Life Investigation For Enceladus A Sample Return Mission Concept in Search for Evidence of Life. *Astrobiology*, 12(8):730–742, 2012.

[87] Kim Reh, Linda Spilker, Jonathan I. Lunine, J. Hunter Waite, Morgan L. Cable, Frank Postberg, and Karla Clark. Enceladus Life Finder: The search for life in a habitable Moon. *IEEE Aerospace Conference Proceedings*, pages 1–8, 2016.

[88] C Sotin, K Altwegg, R H Brown, K Hand, J I Lunine, J Soderblom, J Spencer, and P Tortora. JET: JOURNEY TO ENCELADUS AND TITAN. In *42nd Lunar and Planetary Science Conference*, 2011.

[89] Giuseppe Mitri, Frank Postberg, Jason M. Soderblom, Peter Wurz, Paolo Tortora, Bernd Abel, Jason W. Barnes, Marco Berga, Nathalie Carrasco, Athena Coustenis, Jean Pierre Paul de Vera, Andrea D'Ottavio, Francesca Ferri, Alexander G. Hayes, Paul O. Hayne, Jon K. Hillier, Sascha Kempf, Jean-Pierre Lebreton, Ralph D. Lorenz, Andrea Martelli, Roberto Orosei, Anastassios E. Petropoulos, Kim Reh, Juergen Schmidt, Christophe Sotin, Ralf Srama, Gabriel Tobie, Audrey Vorburger, Vronique Vuitton, Andre Wong, and Marco Zannoni. Explorer of Enceladus and Titan (E2T): Investigating ocean worlds' evolution and habitability in the solar system. *Planetary and Space Science*, 155:73–90, 2018.

[90] Stefano Campagnola and Ryan P Russell. Endgame Problem Part 1: V-Infinity-Leveraging Technique and the Leveraging Graph. *Journal of Guidance, Control, and Dynamics*, 33(2):463–475, 2010.

[91] Nathan Strange, Ryan Russell, and Brent Bungton. Mapping the V-infinity Globe. *Advances in the Astronautical Sciences*, 129:423446, 2007.

[92] Stefano Campagnola and Ryan P Russell. Endgame Problem Part 2: Multibody Technique and the Tisserand-Poincare Graph. *Journal of Guidance, Control, and Dynamics*, 33(2):476–486, 2010.

[93] Ryan C Woolley and Daniel J Scheeres. Applications of V-Infinity Leveraging Maneuvers to Endgame Strategies for Planetary Moon Orbiters. *Journal of Guidance, Control, and Dynamics*, 34(5):1298–1310, 2011.

[94] Mark Adler, Robert C. Moeller, Chester S. Borden, William D. Smythe, Robert F. Shotwell, Bjorn F. Cole, Thomas R. Spilker, Nathan J. Strange, Anastassios E. Petropoulos, Debarati Chattopadhyay, Joan Ervin, Elizabeth Deems, Peter Tsou, and John Spencer. Rapid Mission Architecture trade study of Enceladus mission concepts. In *2011 Aerospace Conference*, pages 1–13. IEEE, 2011.

[95] Howard D. Curtis. *Orbital Mechanics for Engineering Students*. Butterworth-Heinemann, 3rd editio edition, 2014.

[96] Alan M. Cassell, Chad A. Brivkalns, Jeff V. Bowles, Joseph A. Garcia, David J. Kinney, Paul F. Wercinski, Alicia D. Cianciolo, and Tara T. Polsgrove. Human Mars mission design study utilizing the adaptive deployable entry and placement technology. *IEEE Aerospace Conference Proceedings*, pages 1–16, 2017.

[97] James O. Arnold, Keith H. Peterson, Bryan C. Yount, Nigel Schneider, and Jose Chavez-Garcia. Thermal and Structural Performance of Woven Carbon Cloth For Adaptive Deployable Entry and Placement Technology. In *AIAA Aerodynamic Decelerator Systems (ADS) Conference*, Daytona Beach, FL, 2013. AIAA.

[98] James O. Arnold, Bernard Laub, Yih-Kang Chen, Dinesh K. Prabhu, M. E. Bittner, and Ethiraj Venkatapathy. Arcjet Testing of Woven Carbon Cloth for Use on Adaptive Deployable Entry Placement Technology. In *IEEE Aerospace Conference*, Big Sky, MT, 2013.

[99] Sarag J Saikia, Harish Saranathan, James Longuski, and Michael J Grant. Trajectory Optimization Analysis of Rigid Deployable Aerodynamic Decelerator. In *AIAA/AAS Astrodynamics Specialist Conference*, San Diego, CA, 2014. AIAA.

[100] Robert D Braun and Robert M Manning. Mars Exploration Entry, Descent, and Landing Challenges. *Journal of Spacecraft and Rockets*, 44(2):310–323, 2007.

[101] Alex Austin, Adam Nelessen, Bill Strauss, Joshua Ravich, Mark Jesick, Ethiraj Venkatapathy, Robin Beck, Paul Wercinski, Michael Aftosmis, Michael Wilder, Gary Allen, Robert Braun, Michael Werner, and Evan Roelke. SmallSat Aerocapture to Enable a New Paradigm of Planetary Missions. In *2019 IEEE Aerospace Conference*, pages 1–20. IEEE, 2019.

[102] Eric M. Queen. Angle-of-Attack-Modulated Terminal Point Control for Neptune Aerocapture. In *14 AAS/AIAA Space Flight Mechanics Conference*, Maui, Hi, 2004. AAS 04-129.

VITA

Ye Lu earned his Bachelor of Science with a double major in Aerospace Engineering and Mathematics from Worcester Polytechnic Institute (WPI) in 2013, where he graduated with highest distinction. He then earned Master of Science in Aerospace Engineering from WPI in 2015. During his study in WPI, he worked under Prof. Nikolaos Gatsonis and Prof. Michael Demetriou in Dynamic and Controls. In the Fall of 2015, Ye began is Ph.D. graduate studies in Astrodynamics and Space Applications at Purdue University under the guidance of Dr. Sarag J. Saikia and Prof. James M. Longuski. During his Ph.D. study, Ye worked as an instructor for the Department of Mathematics from 2015–2016 and taught Calculus. Then starting the summer of 2016 and til the summer of 2018, Ye was a Graduate Assistant in the College of Engineering, where he planned and organized the Summer Undergraduate Research Fellowship (SURF) program. In addition to his research on spacecraft and mission design using aeroassist maneuvers, his research interests also include design of small satellites for low-cost planetary missions and technology demonstrations. After graduation, he will join the Aerospace Program as Assistant Professor (Tenure-Track) at the Kent State University in Kent, OH.